2005

A study of ion acceleration, asymmetric optical pumping and low frequency waves in two expanding helicon plasmas

Xuan Sun
West Virginia University

Recommended Citation

Sun, Xuan, "A study of ion acceleration, asymmetric optical pumping and low frequency waves in two expanding helicon plasmas" (2005). *Graduate Theses, Dissertations, and Problem Reports*. 2334.
https://researchrepository.wvu.edu/etd/2334

A Study of Ion Acceleration, Asymmetric Optical Pumping and Low Frequency Waves in Two Expanding Helicon Plasmas

Xuan Sun

Dissertation Submitted to the College of Arts and Sciences
at West Virginia University
in partial fulfillment of the requirements
for the degree of

Doctor of Philosophy
in
Plasma Physics

Earl Scime, PhD., Committee Chair
Mark Koepke, PhD.
Manfred Boehm, PhD.
Gurudas Ganguli, PhD.
Charter Stinespring, PhD.

Department of Physics
Morgantown, West Virginia
2005

Keywords: Helicon plasma, Ion speed, Double layer, Asymmetric, Drift Alfvén wave

Abstract

A Study of Ion Acceleration, Asymmetric Optical Pumping and Low Frequency Waves in Two Expanding Helicon Plasmas

Xuan Sun

This work concerns measurements of parallel ion flow, optical pumping, and low frequency waves in expanding plasmas generated by two different helicon plasma sources. The measurements confirm numerical predictions of the formation of a current-free double layer in a region of diverging magnetic field. With laser-induced fluorescence (LIF), the double layer structure in both helicon plasma sources was investigated through measurements of the bulk parallel ion flow speed. Both double layers have a total potential drop of $3\text{-}4kT_e$ and length scales smaller than ion-neutral mean-free-path. A stronger double layer, with a potential drop of $\sim 6kT_e$, was created in a uniform magnetic field region with a plasma limiting aperture plate. During the investigations of ion acceleration in expanding plasmas, a new phenomenon, asymmetrical optical pumping (AOP) due to the acceleration of ions in magnetic field gradient, was observed. The signature of AOP is a difference in the LIF emission amplitude from a pair of Zeeman-split ion states. A model that reproduces the dependence of the AOP on magnetic-field and ion-velocity gradients is described. With magnetic fluctuation probes, low frequency, transverse, electromagnetic waves were also identified in the expanding helicon plasma. The wave is localized to the vicinity of the maximum plasma density gradient and appears only at low neutral pressure. Based on the scaling of the wave frequency and amplitude with magnetic field strength, the wave was identified as the resistive drift Alfvén wave.

Acknowledgements

First, I would like to thank my advisor, Professor Earl Scime. It has been a great pleasure to work with him. I have been deeply impressed not only by his intelligence, insight, and energy, but also the way in which he has mentored me. I have come to learn that an advisor can also be a friend, a friend that you can count on and believe in. I want to thank Dr. John Kline for his help in my first year working in lab. He set for me an example of how to be an excellent graduate student. I thank Professor Robert Boivin for his many internal reports, they were very helpful in my research. Thanks also go to Dr. Costel Biloiu for helpful discussions as well as many scientific and technical interactions. I extend thanks to my colleagues: Bob Spangler, Amy Keesee, Robert Hardin, and Chris Compton for all their assistance and support. I thank the technical staff: Doug Mathess, Carl Weber, and Tom Milan for the construction of probes and other experimental apparatus. And I also want to thank Professor Mark Koepke, Professor Manfred Boehm, Dr. Guru Ganguli, and Professor Charter Stinespring for serving on my committee.

Part of my research was completed at Princeton Plasma Physics Laboratory (PPPL) in the collaboration with Professor Samuel Cohen. I want to thank him for his guidance and our enlightening conversations. His influence on my growth as a scientist has been significant. I would also like to thank Bruce Berlinger for the excellent technical support while I was at PPPL.

I am greatly indebted to my parents for all the things they have done for me. Being on the opposite side of the Earth these years, I have missed them very much. Last, but certainly not least, I am grateful to my wife Ming Luo, who encourages and supports me constantly. Her suggestions for me both in science and life are always wise.

Table of contents:

Chapter 1: Introduction

The principle results of this dissertation concern experimental investigations of ion flow speeds, low frequency electromagnetic waves, and laser pumping of optical transitions in expanding helicon plasmas in a magnetic field gradient. For adiabatically steady flow, the speed of a neutral fluid or gas in a nozzle (see Fig.1-1a) cannot achieve supersonic speeds without the use of a *de Laval* nozzle (Fig.1-1b) [1]. The same conclusion is usually applied to plasmas, which are usually treated as quasi-neutral fluids. Using the one-dimensional continuity and momentum conversation equations, flow speed can be expressed as a function of plasma expansion:

$$\frac{dM}{dz} = \frac{M}{M^2 - 1}\frac{1}{A}\frac{dA}{dz}, \tag{1.1}$$

where M is the plasma flow speed normalized to the sound speed and A is the cross sectional area of the plasma. In these experiments, the plasmas expand from source at high magnetic field strength to an expansion chamber at lower magnetic field strength. Thus, the plasmas evolve from a small cross sectional area to a larger area, i.e. $dA/dz > 0$. Assuming the plasma outflow speed in the source is initially subsonic, i.e. $M < 1$, Eq. (1.1) predicts plasma deceleration during the expansion – in contradiction to most experimental observations in expanding plasmas. Moreover, there is a singularity at $M = 1$ if plasma accelerates from subsonic speeds. To remove the singularity, *Manheimer* and *Fernsler* [2] included the effects of collisionality (ionization processes were also incorporated into their collisionality term). Eq. (1.1) becomes:

$$\frac{dM}{dz} = \frac{M\, {}^{dA}\!/_{Adz} - M^2\, {}^{\nu_i}\!/_{C_s}}{M^2 - 1} \tag{1.2}$$

where ν is the ionization rate. However, the question of an accelerating mechanism remains. Eq. (1.2) implies that collisions act as an accelerating force until $M = 1$ and then switch to decelerating force for $M > 1$. Perhaps the most significant omission in the derivation of Eq. (1.2) is the effect of ambipolar and other quasi-static electric fields. As will be shown in this work, such electric fields play a critical role in accelerating ions during plasma expansion.

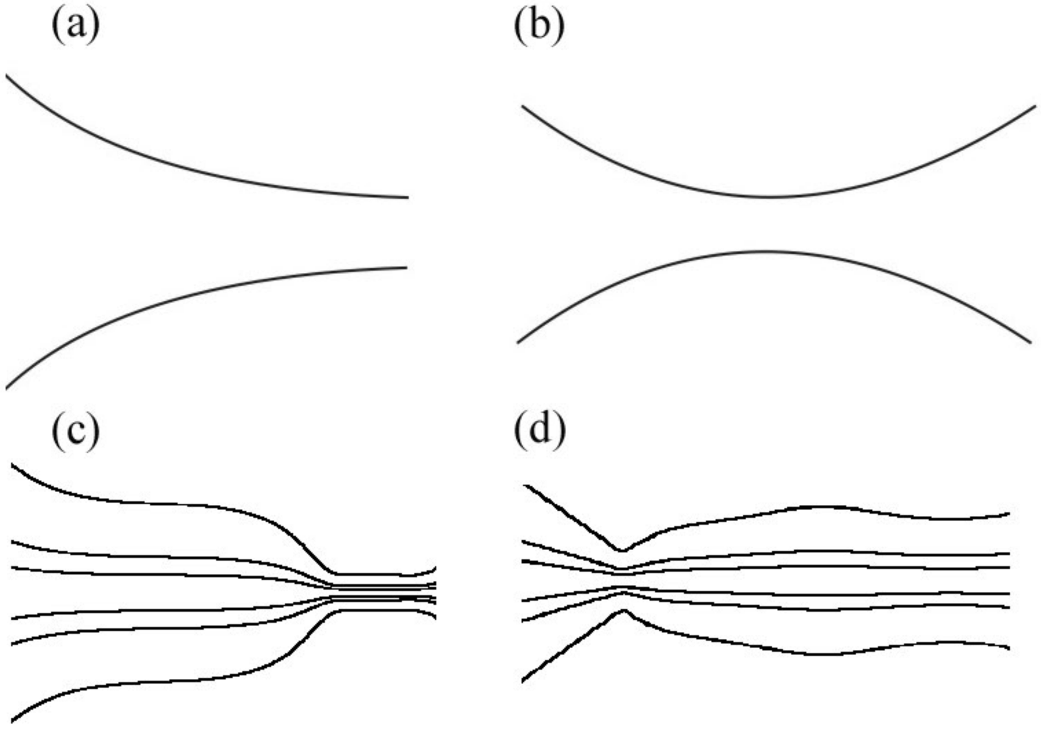

Figure. 1-1. Schematic diagrams of (a) mechanical nozzle with a monotonically decreasing cross sectional area, (b) A classic *de Laval* nozzle. (c) HELIX-LEIA magnetic field geometry. (d) MNX magnetic field geometry.

The experiments for this work were conducted in two different helicon plasma sources: the HELIX-LEIA (Hot hELIcon eXperiment – Large Experimental on Instabilities and Anisotropies) system at West Virginia University (WVU) and MNX (the Magnetic Nozzle eXperiment) at Princeton Plasma Physics Laboratory (PPPL). The magnetic geometries of both experiments are shown in Fig. 1-1c and 1-1d, respectively.

The HELIX-LEIA magnetic field geometry is fundamentally similar to the free expansion schematic shown in Fig 1-1a. Using laser induced fluorescence (LIF) to measure the ion velocity distribution function (IVDF), supersonic ion outflow speeds of Mach number ~2.2 were observed in the HELIX-LEIA system. At low neutral pressures, when the ion-neutral collision length was comparable to the scale length of magnetic field gradient, a localized electric field developed at the end of the helicon source. The localized electric field had the characteristics of an electric double layer (DL). In MNX, with a magnetic field geometry similar geometry that shown in Fig. 1-1b, magnetic mirror acceleration of ions, i.e., the magnetic nozzle effect, was not observed at low mirror ratio (the ion flow speed actually increased with decreasing mirror ratio). As in the HELIX-LEIA experiments, in MNX the DL developed in the magnetic field gradient region. An introduction to double layers and the HELIX-LEIA facility is given in the latter part of Chapter 1 of this dissertation. The diagnostics used to make the measurements are described in Chapter 2. Experimental results in HELIX are shown in Chapter 3 and the experimental results in MNX, along with an introduction to the MNX facility, are presented in Chapter 4.

Chapter 5 describes a new phenomenon discovered during the MNX experiments. When performing LIF measurements of the IVDF parallel to the magnetic field, the LIF emission amplitude from two Zeeman split transitions was found to differ significantly. Unpolarized, laser light injected parallel to the magnetic field should equally pump both the $\sigma+$ and $\sigma-$ transitions and because of equal state populations the LIF emission should be strictly symmetric. However, in the presence of a double layer and a magnetic field gradient the LIF emission was found to differ by as much as a factor of three. A theoretical model that accurately predicts the dependence of the asymmetry on nozzle magnetic field strength and ion collisionality was constructed and is also discussed in Chapter 5. The key physics is that when the ions accelerate along a magnetic field gradient, the effective interaction time with the laser is different for $\sigma-$ and $\sigma+$ transitions, i.e., asymmetric optical pumping. This same effect could be responsible for the asymmetric Stokes V profiles observed in solar spectroscopic measurements.

Finally, in Chapter 6 the characteristics of a set of low frequency electromagnetic waves observed in the HELIX-LEIA system at low neutral pressures are described. The scaling of the wave frequency and amplitude with magnetic field strength are shown to be consistent with the excitation of resistive drift Alfvén waves.

1.1 Review of Double Layers

Because double layers play a key role in many of the phenomena reported in this dissertation, it is worthwhile to begin with a review the basic characteristics of double layers. In its simplest form, a double layer consists of two spatially separated charge layers, one positive and one negative. In other words, the DL is a freestanding sheath and can appear anywhere in a plasma. The physical location of DL distinguishes it from the conventional sheath, which appears at the surface of an object inserted into plasma or at plasma boundary [3]. In laboratory plasmas, a DL's thickness can vary from several to thousands of Debye lengths. However, that a DL's thickness must be smaller than the ion mean-free path is commonly stated in the literature [4]. Since freely expanding electrons can create an ambipolar electric field that accelerates out of the source at the sound speed, a potential drop larger than kT_e/e is another often cited requirement for a plasma structure to be identified as a double layer. Strong DLs can have potential drops many times the electron temperature, e.g., many hundreds of, if not thousands, times the electron thermal energy [5,6,7,8]. However, a potential drop with less than kT_e is possible for types of DLs, e.g. the slow ion acoustic type double layer [9]. A typical DL potential structure with its associated charged particle populations is shown in Fig. 1-2. To maintain a double layer, at least three of the four particle populations, i.e. free and trapped ions and electrons, must be present [4]. It is also possible that a DL not consist of a single monotonically decreasing potential structure. A DL may contain potential dips on either side of DL or include a series of smaller DL-like structures.

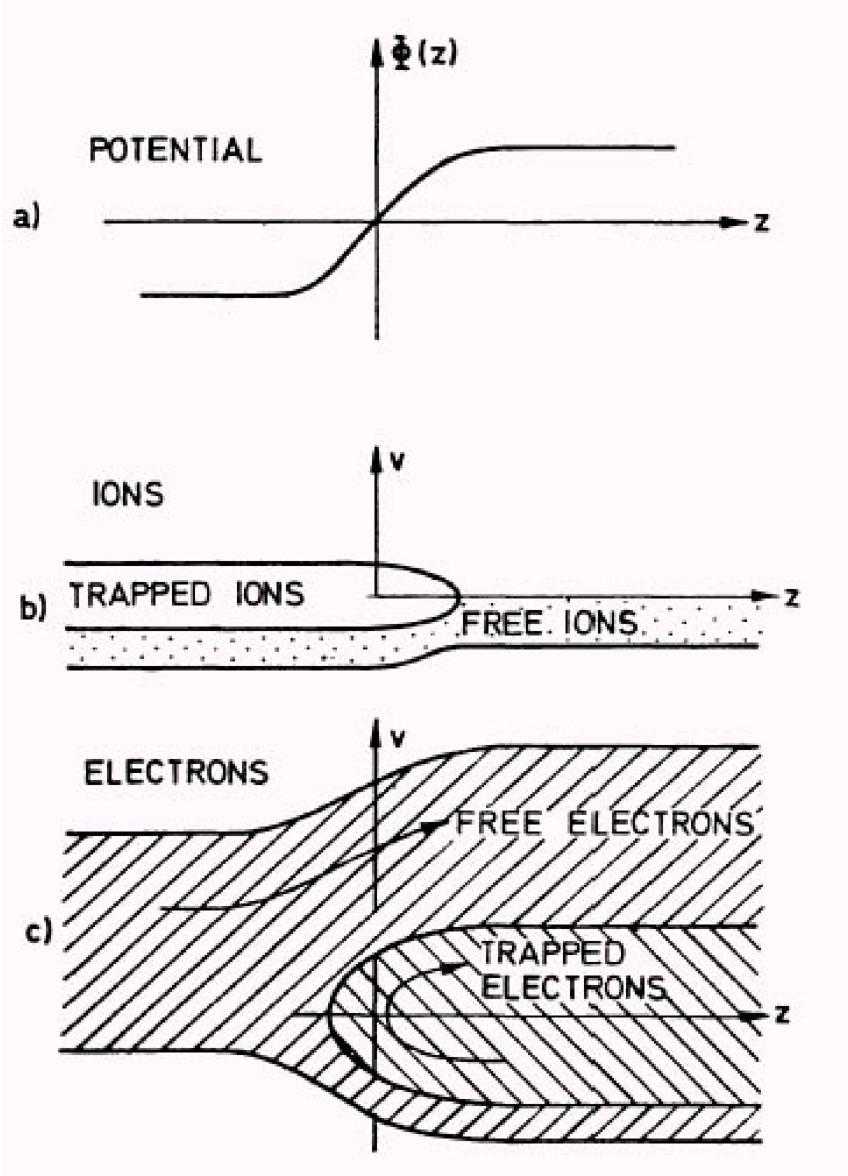

Figure 1-2. (1) Potential structure of plasma potential distribution. (b) Phase space for trapped and free ions. (3) Phase space for trapped and free electrons. From Ref. [4].

Experimental studies of sheathes can be traced back to the work in the 1920's by *Irving Langmuir* and *Harnord Mott-Smith*. In 1958, *Hannes Alfvén* [10] was the first to suggest that DLs could be important in space plasmas. Soon afterward, in 1960, *Carl McIlwain* [11] hypothesized that the monoenergetic electrons in the auroral region were accelerated by magnetic field-aligned electric fields. *Albert* and *Lindstrom* provided more evidence of DLs in the auroral region in 1970 based on analysis of data from a rocket probe launched in 1966. They suggested the auroral electrons were accelerated by a DL rather than stochastic processes [12]. A number of laboratory plasmas and computer simulations have been carried out to study the dynamics of DLs and the conditions required to form DLs.

A one dimensional electrostatic DL in a collisionless plasma can be described by the Poisson equation [4,13]:

$$\varepsilon_0 \frac{\partial^2 \phi(x)}{\partial x^2} = -\sum_\alpha q_\alpha \int_{-\infty}^{+\infty} du f_\alpha(x,u) \tag{1.3}$$

and the Boltzmann equation for each population in steady-state:

$$u\frac{\partial f_\alpha(x,u)}{\partial x} - \frac{q_\alpha}{m_\alpha}\frac{\partial \phi(x)}{\partial x}\frac{\partial f_\alpha(x,u)}{\partial u} = 0, \tag{1.4}$$

where $f_\alpha(x,u)$ is the particle distribution function. α identifies either positive or negative species, m_α and q_α are the corresponding mass and charge for each species, and $\phi(x)$ is the spatial potential profile. Introducing the particle energy $W = mu^2/2 + q_a\phi$, the general solution of Eq. (1.3) can be written as:

$$f_a = f_a(W) \tag{1.5}$$

Thus, Eq. (1.3) can be transformed:

$$\varepsilon_0 \frac{\partial^2 \phi(x)}{\partial x^2} = -\sum_\alpha q_\alpha \int_{W_{\alpha 1}}^{W_{\alpha 2}} \frac{dW f_\alpha(W)}{\sqrt{2m_a(W + q_a\phi(x))}} \tag{1.6}$$

$W_{\alpha 1}$ and $W_{\alpha 2}$ are the energy limits of particle α. Eq. (1.6) is a non-linear equation with unlimited classes of solutions. Multiplying Eq. (1.6) by $d\phi/dx$ and integrating with respect to *x, Bernstein, Greene,* and *Kruskal* (BGK) [14] obtained the differential equation:

$$\frac{1}{2}\varepsilon_0 (d\phi/dx)^2 + V(\phi) = const. \ , \tag{1.7}$$

which describes particle thermal pressure balance in an electric field. The potential term, $V(\phi) = -\sum_{\alpha} q_\alpha \int_{W_{\alpha 1}}^{W_{\alpha 2}} dW f_\alpha(W)\sqrt{2m_\alpha(W + q_\alpha \phi(x))}$, is called the Sagdeev or classical potential [13] because Eq. (1.7) is analogous to the standard energy conservation equation if one treats the x as 'time' t and ϕ as the 'position'. Using fluid theory, *Block* (1972) obtains for the DL equation $\sum_{\alpha}(n_\alpha kT_\alpha + n_\alpha m_\alpha u_{D\alpha}^2) - \varepsilon_0 E^2/2 = const.$, which is the same as Eq. (1.7) if one integrates the distribution function over all velocities.

If the electric field strength, $d\phi/dx$, is zero at both ends of the DL, then one obtains

$$V(0) = V(\phi_{DL}) \text{ or } \sum_{\alpha}(n_\alpha kT_\alpha + n_\alpha m_\alpha u_{D\alpha}^2) = const. \tag{1.8}$$

For very strong DLs, the ion kinetic energy after acceleration through the DL and the electron kinetic energy before DL retardation dominate the other terms in Eq. (1.8). Therefore, $(n_e m_e u_{De}^2)_+ = (n_i m_i u_{Di}^2)_-$ and where index + and – represents the high and low potential side of DL, respectively. Since they are accelerated by same DL, their energies are about equal. Thus, this relationship can be rewritten as:

$$\frac{n_e u_{De}}{n_i u_{Di}} = (m_i/m_e)^{1/2}, \tag{1.9}$$

the so-called Langmuir condition. The Langmuir condition implies a non-vanishing current in the DL since the electron flux is a factor of $(m_i/m_e)^{1/2}$ larger than the ion flux through a strong DL. The Langmuir condition only applies for strong DLs for which the electric field in the presheath can be ignored. It is worth noting, however, that current-free DLs can be in principle exist in laboratory experiments [4].

The spatial structure of the DL is given by the second integral of Eq. (1.7)

$$x - x_0 = \pm\sqrt{\varepsilon_0 / 2}\int_{\phi_0}^{\phi} \frac{d\phi^{'}}{\sqrt{const. - V(\phi^{'})}}, \tag{1.10}$$

that in turn depends on the form of the Sagdeev potential. A Sagdeev potential for monoenergetic beams of ions and electrons entering from the high potential side of the DL and trapped Maxwellian ions and electrons can be written as [13]:

$$-V(\phi) = n_{0e}e^{-e(\phi_{DL}-\phi)/kT_e} + \frac{m_e i_e}{e}\sqrt{u_{0e}^2 + \frac{2e\phi}{m_e}} + n_{0i}e^{-e\phi/kTi} + \frac{m_i i_i}{e}\sqrt{u_{0i}^2 + \frac{2e(\phi_{DL}-\phi)}{m_i}} \tag{1.11}$$

where i_e and i_i are the injected electron and ion currents, respectively. Inserting this potential into Eq. (1.10), the DL spatial structure is obtained. In laboratory plasmas, for which the particle distributions are not precisely known, the Sagdeev potential for a weak DL can be expanded as power series of ϕ and the spatial structure obtained numerically for a specific set of boundary conditions [13].

In the absence of a complete solution for the DL structure, additional information about the physics of DLs can still be obtained from the boundary condition requirements. Since the high potential side of DL must be positively charged, and the low potential side must be negatively charged:

$V^{'}(0 + \delta\phi) < 0$, which is equivalent to $-\sum_{\alpha} q_{\alpha}\int_{W_{\alpha 1}}^{W_{\alpha 2}} \frac{dWf_{\alpha}(W)}{\sqrt{2m_a(W + q_a\phi(x - \delta x))}} < 0$

and $V^{'}(\phi_{DL} - \delta\phi) > 0$, which is equivalent to

$$-\sum_{\alpha} q_{\alpha}\int_{W_{\alpha 1}}^{W_{\alpha 2}} \frac{dWf_{\alpha}(W)}{\sqrt{2m_a(W + q_a\phi(x + \delta x))}} > 0$$

These two expressions imply that the electron density decreases faster than the ion density on the high potential side and vise versa. Considering an ion entering the DL with speed u_0 from the high potential side, the ion density at position δx inside the DL is given by:

$$n_i(\delta x) = \frac{n_{i0} u_0}{\sqrt{u_0^2 + 2e\delta\phi / m u_0^2}}, \tag{1.12}$$

and the electron density is given by the Boltzmann equation:

$$n_e(\delta x) = n_{e0} \exp(-e\delta\phi / kT_e), \tag{1.13}$$

where $\delta\phi$ is a negative and first order quantity. Taylor expanding $n_i(x)$ and $n_e(x)$, the boundary conditions on the potential lead to the condition $m_i u_0^2 > kT_e$. Thus, ions must enter the DL with speeds larger than the ion sound speed ($\sqrt{kT_e / m_i}$). An identical criterion is known as the Bohm criterion for ions entering a sheath at a plasma boundary. Similar analysis on the low potential side yields $m_e u_{e0}^2 > kT_{ti}$, where kT_{ti} is the trapped ion thermal energy. A fluid model yields a more restrictive condition, $m_e u_{e0}^2 > k(\gamma T_{fe} + T_{ti})$,where kT_{fe} is the free electron thermal energy and γ is the specific heat ratio. However, laboratory experiments and computer simulations suggest the electrons must drift into the DL from the low potential side with a minimum speed equal to the electron thermal speed, $m_e u_{e0}^2 > 2kT_{fe}$, which implies a critical current density $j_c = ne\sqrt{2kT_e / m_e}$ to maintain the DL – the Bohm current criterion [4]. It should be pointed out that both the Langmuir condition and the Bohm criterion are only valid for strong DLs.

If the Bohm criterion is satisfied for a DL, it is possible that current driven instabilities will be excited in the DL, e.g., ion acoustic and cyclotron instabilities. Since there are four different populations of particles, excitation of the two-stream instability should also be considered. Among these instabilities, the threshold for the Buneman instability is the same current criterion as the Bohm criterion. Thus, some authors argue that this instability may play an important role in the formation of DLs. Other instabilities, e.g., the Pierce instability, may trap ions in a narrow strongly varying potential and form a laminar double layer [15]. Once formed, the charge separation of the DL can persist without the presence of the Pierce instability since the charge distribution of a DL is one of the solutions of the BGK equation. Ion-acoustic driven DLs, characterized by an ion hole on the low potential side and a potential difference equal to or less than the electron temperature [16], are observed to coincide with the existence of ion acoustic instabilities in computer simulations [17]. Whether ion-acoustic instabilities play an important role in DL formation or are a side effect of DL formation remains an open question.

An analysis of DL stability when the particle distributions are well known was given by *Knorr* and *Goertz* [18]. They used the Penrose criterion to determine DL stability in a homogeneous plasma [19],

$$P = \int_{-\infty}^{+\infty} \frac{1}{(u - u_0)} \frac{dF(u)}{du} < 0 \tag{1.14}$$

where $F(u) = f_e(u) + f_i(u) m_e / m_i$ and f_e and f_i are the electron and ion distribution functions, respectively. Using this criterion and Eq. (1.6), *Knorr* and *Goertz* [18] calculated the P value by artificially specifying some ion and electron distribution functions. However, the usefulness of the Penrose criterion is limited in laboratory plasmas because of the requirement to know the details of the particle distribution and its application to only homogeneous plasmas. The expanding HELIX-LEIA and MNX plasmas are clearly not homogeneous.

Experimental studies of DLs have been carried out in plasmas with densities ranging from 10^6 to 10^{20} cm^{-3} [20] and electron temperatures from several eV [21] to hundreds of eV [5]. Observed DL thickness have ranged from several Debye lengths [22] to thousands of Debye lengths [6]. In laboratory experiments and simulations, DLs are typically produced in systems driven by electric current, externally imposed potential differences, or by externally imposed electron temperature differences between two plasma components. The first measurements of a DL potential structure were performed in a double plasma source. The relatively low plasma density of the double plasma source yielded a wide DL structure that was well suited for investigation with in-situ probes [23]. A few years later *Hatakeyama et al.* [24] investigated the potential depression formed between two magnetized plasmas, a potassium Q-machine plasma and an argon discharge plasma, both expanding from opposite ends towards the middle of a long vacuum chamber. A spatially narrow magnetic field perturbation, a region of weaker magnetic field, was applied near the middle of the chamber. By varying the ratio of pressures in the sources, the position of the double layer could move until a new thermal pressure balance was achieved. *Hatakeyama et al*. [24] observed a negative potential dip on the low potential side of DL that served to reflect the electrons from the downstream side of the DL. Increasing the magnetic field strength or decreasing the neutral pressure without change the pressure ratio caused the potential dip to become sharper and deeper. The DL served to separate the two plasmas from direct thermal contact.

Target plasmas for later investigations of DLs improved greatly with the introduction of the triple plasma device, i.e., TP. The TP device consists of a target chamber in the center and two identical plasma sources at each end. Each source is separated from the target by two grids, which can be biased with different potentials. The TP is essentially an improved version of the double plasma device in which the target chamber is placed between the two plasma sources. The type of double layer created in the TP is controllable by varying the potential on the biasable grids. Strong ($e\phi/T_e > 10$) [25], weak ($e\phi/T_e \sim 5$) [26], one dimensional to two-dimensional [27], and stationary to moving double layers [28] have been produced in TP devices.

DLs have also been observed in freely expanding laboratory plasmas if the plasma source contains both Maxwellian and energetic electrons. *Harapetian* and *Stenzel* studied the temporal and spatial evolution of a DL in a diffusion chamber, i.e. into where the plasma expands, with a low background neutral pressure (10^{-6} cm^{-3}) by using emissive probes and a directional energy analyzer [29,30,31]. The source plasma was found to have a 3.5 eV Maxwellian electron population plus a 30 eV tail electron population. Although the density of the tail electrons was only 1 – 5 % of the thermal electrons, their energy determined the DL strength. Decreasing the ratio of tail to thermal electron density by forcing thermal electrons to pass through the DL by applying a positive bias to one of the endplates decreased the DL amplitude. At large enough bias potential, DL formation was completely suppressed. Time resolved measurements of the DL potential profile revealed that the DL propagated into the chamber with a speed of about the ion sound speed and reached steady state after 200 microseconds. *Harapetian* and *Stenzel*

[29,30,31] concluded that the DL arose along the expansion front of the plasma where thermal electrons were trapped by a large potential drop due to the energetic tail electrons. They suggested that the DL was generated self-consistently to maintain the separation of the distinct electron populations. Their two dimensional potential measurements showed most of the electric field was concentrated at the center of the layer, as shown in Fig. 1-3, i.e. U-shape equipotential contours on both sides of DL. In TP experiments, *Hershkowitz* noted that the equipotential contours must be parallel to the boundaries (or device axis) at large radii if the boundaries are metal conductors [20].

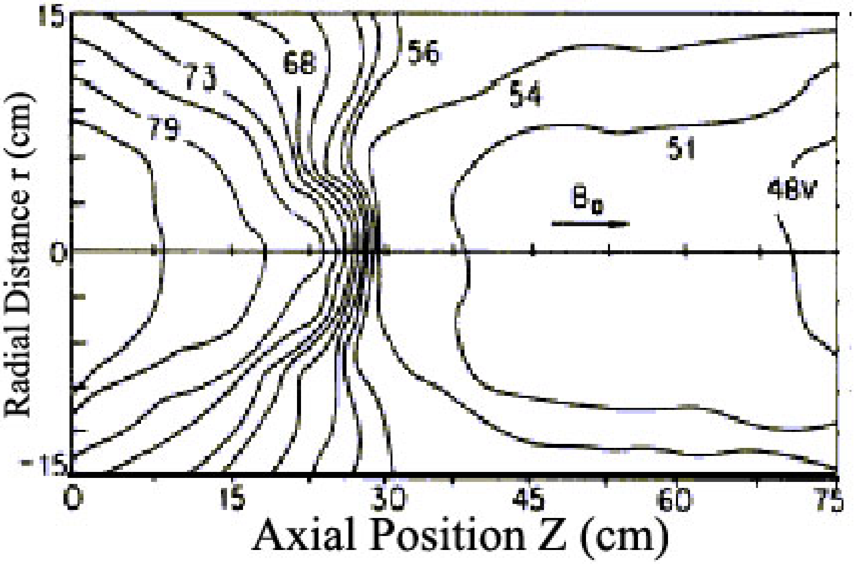

Figure 1-3. Contours of constant plasma potential showing a steady-state double layer in a freely expanding plasma. Adapted from Ref. [31].

Along the terrestrial magnetic field, ion acoustic DLs and soliton-like structures are often observed by satellites, e.g., S3 [32,33,34], Viking [35,36], FAST [37], and others [38,39,40], above 4000 km. Simultaneously, ion-cyclotron-like waves are observed propagating in the perpendicular direction. Some authors have argued that ion phase space holes seen in the satellite measurements can evolve into weak double layers [41]. Essentially (in a plasma with an electron beam and an ion hole propagating in the same direction as the electron beam), if the electron drift speed is larger than the ion hole propagation speed (the sound speed for ion acoustic solitons), reflection of electrons cause an excess of electron density on the upstream side of the propagating hole. The electron density increase makes the negative potential structure deepen and become more asymmetric – thereby leading to formation of a weak DL.

1.2 Double Layers in Helicon Plasmas

A helicon source plasma is a high-density, current-free, rf-wave driven plasma. Helicon source can operate in either a steady-state or pulsed mode. Since first built by *Boswell* [42], the helicon plasma source has been used for a variety of applications including: space-relevant, high-beta studies [43], materials processing [44], basic plasma studies [45], and plasma propulsion [46]. An often cited characteristic of an argon helicon plasma is the appearance of the 'blue core'(or helicon) mode [42] as the source transitions from the relative low density 'C' and 'L' modes (capacitive and inductive modes) into the helicon mode. The transition is typically initiated by increasing the magnetic field strength or rf power. Although the mechanism responsible for the efficient rf coupling in helicon sources is still a matter of some debate, their high efficiency, compatibility with low mass ions for high specific impulse operation, steady-state operation without electrodes, and modest magnetic field strengths make helicon plasma sources ideal candidates for thermal plasma propulsion systems.

For plasma thrusters, ion flow speed in the expanding plasma is the critical parameter. In a thermal plasma thruster, the plasma is heated and the random energy of the hot propellant converted into directed flow (i.e., thrusting out of the source), in a physical or magnetic nozzle [47, 48, 49]. Since half of a magnetic nozzle is essentially an expanding magnetic field, and the minimum specific impulse, $I_{sp}(\equiv v/g$, where $g = 9.8$ m/s), considered desirable for remote-planet missions is 3000 s, corresponding to the speed of ~30,000 m/s, control of the ion physics in the expanding plasma is critical to optimizing the characteristics of a plasma thruster.

Recently, *Charles* and *Boswell* [50] reported measurements of a discontinuity in the plasma potential, i.e., an electric double layer, at the end of a low pressure (≤ 0.5 mTorr), argon helicon plasma. Using a retarding field energy analyzer, they mapped the plasma potential along the axis of the device and found that when the neutral pressure dropped below 0.5 mTorr, a "rapid and discontinuous change in the plasma potential close to the exit of the source" appeared (see Fig. 1-4). As the neutral pressure in the source was lowered from 3 mTorr to 0.2 mTorr, the electric field inside the source increased from approximately 50 V/m to 220 V/m. The total potential drop from the closed end of the source to near the open end of the helicon source was approximately +50 V, equivalent to the acceleration of an argon ion at rest to a velocity of 15,500 m/s. Beyond the end of the helicon source, the plasma potential decreased only slightly. Given the measured electric fields, it was assumed that ions inside the source were accelerated out of the source and into the diffusion chamber. Very recent retarding potential analyzer measurements in the same system confirmed that ions are accelerated through the double layer structure in both argon [51] and hydrogen [52] plasmas.

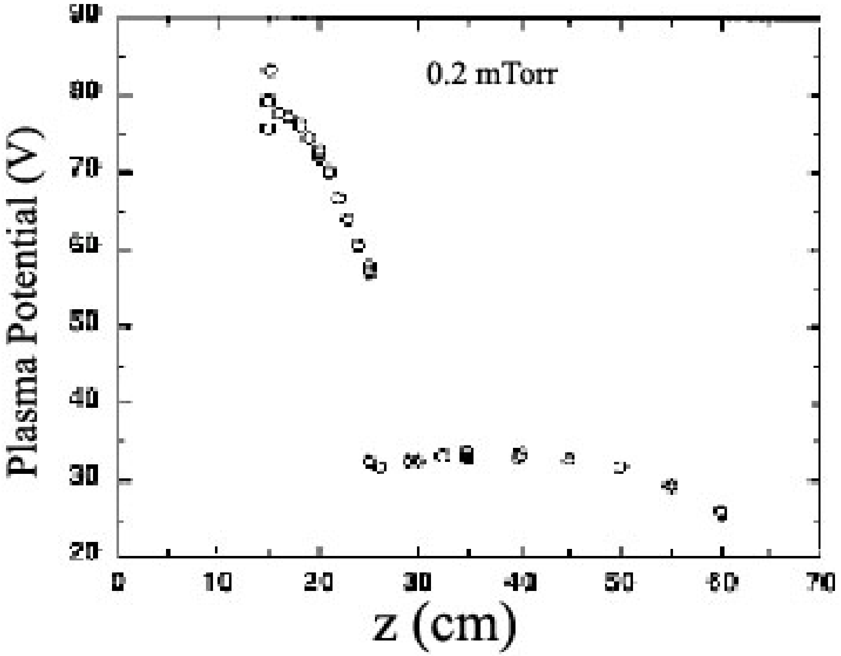

Figure 1-4. Measured plasma potential (using a retarding field energy analyzer) along *z*-axis of the Chi-Kung helicon plasma source [49].

Cohen et al. [53] reported measurements of supersonic ion flows emanating from a small aperture placed at the end of a low pressure, high power density, argon helicon plasma source with a magnetic nozzle. In those experiments, a population of ions flowing out of the aperture at supersonic speeds was observed at low neutral pressures – independent of the magnetic nozzle field strength. The *Cohen et al.* [53] experiments were performed at a helicon source neutral pressure of 0.5 mTorr. The maximum ion energy observed, 30 eV, corresponded to an ion flow speed of roughly 12,000 m/s, i.e., a specific impulse I_{sp} of 1200 s. The ion flow speed was measured with a tunable diode laser based LIF diagnostic [54]. Inside the source chamber, ion flows at or below the ion thermal speed were observed. Based on the rapid acceleration of the ion flow in the vicinity of the aperture, within a few centimeters, it was suggested that an electric double layer was responsible for the observed ion acceleration.

All three DLs observed in helicon plasmas, i.e. Chi-Kung at Australia National University, MNX at Princeton Plasma Physics Laboratory, and HELIX-LEIA at West Virginia University, are formed in the magnetic field expansion region. The divergent magnetic field appears to play a critical role in the formation of double layers, probably through introducing a rapid decrease in electron density along the system axis. As the helicon DLs are current-free and steady-state, the existence of self-consistently driven internal currents (and any instabilities those currents might excite) remains an open and interesting fundamental DL physics question [55]. That such instabilities might limit the efficiency of a helicon source plasma thruster has not gone unnoticed by the plasma thruster community.

1.3 Helicon Plasma Source at WVU

The helicon plasma source at WVU, shown in Fig. 1-5, consists of two regions: HELIX (Hot hELIcon eXperiment) where the plasma is produced and LEIA (Large Experiment on Instabilities and Anisotropies) into which plasma flows from HELIX. The high β ($\beta = nk_bT\mu_o/B^2$) characteristics of LEIA plasmas are used to study magnetospherically relevant plasma physics in the laboratory. The HELIX source can also be operated in pulsed mode. Detailed descriptions of HELIX and LEIA can be found in the dissertations of *Keiter* [56], *Balkey* [57], and *Kline* [58].

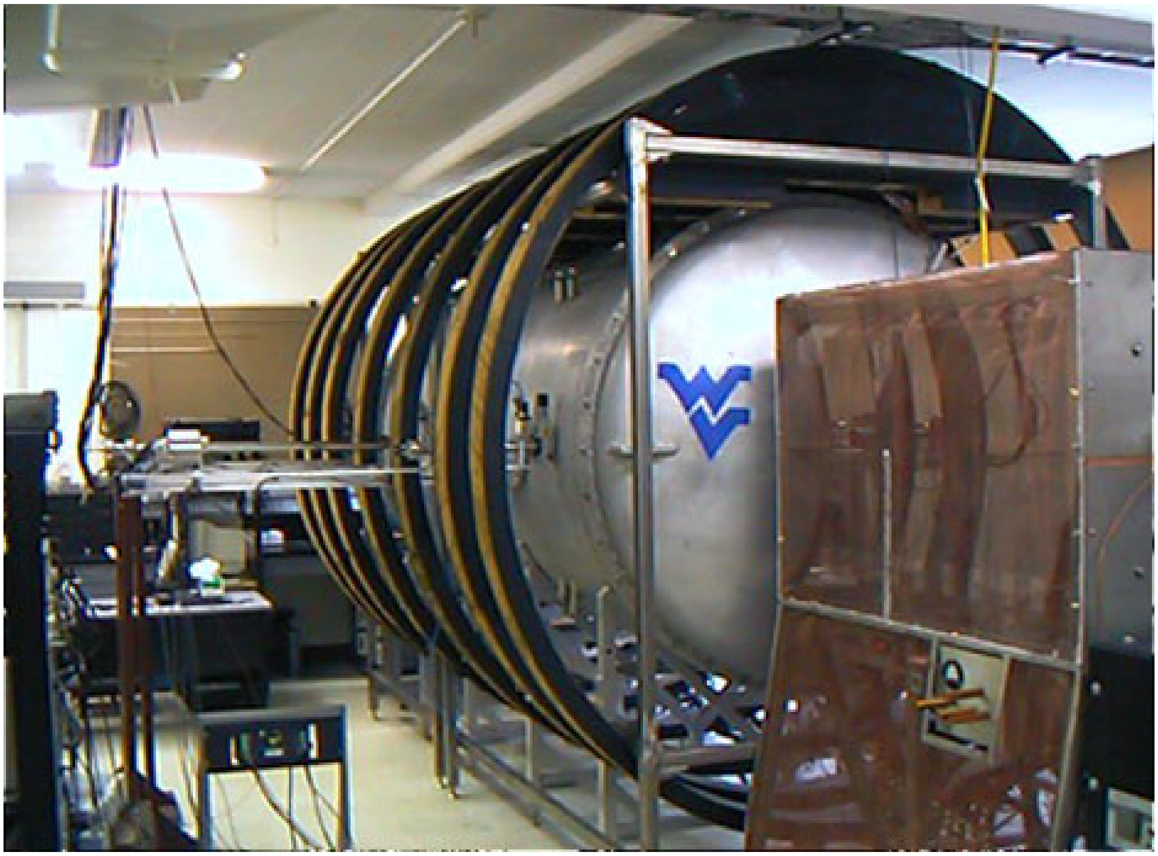

Figure 1-5. HELIX (foreground) and LEIA (large aluminum chamber) system. HELIX resides inside a Faraday cage (rf shielding). The large electromagnets surrounding LEIA are roughly 3 m in diameter [56].

1.3.1 The HELIX-LEIA system

The HELIX-LEIA system (Fig. 1-5) is shown schematically in Fig. 1-6. Starting from the HELIX end, there is a glass tee connected to a pumping station and to a 12” diameter stainless steel flange. The stainless steel flange, which includes the gas inlet for the source, connects to a 4” OD 24” long Pyrex tube. The Pyrex tube connects to a 6” ID, 36” long stainless steel chamber, with one set of four 6” Conflat™ crossing ports and four sets of four 2 ¾” Conflat™ crossing ports. The 2 ¾” Conflat™ crossing ports are spaced evenly on either side of the set of 6” crossing ports. The left end of the stainless steer chamber is directly connected to the LEIA chamber which has an inner diameter of 1.8 m and a length of 4.4 m.

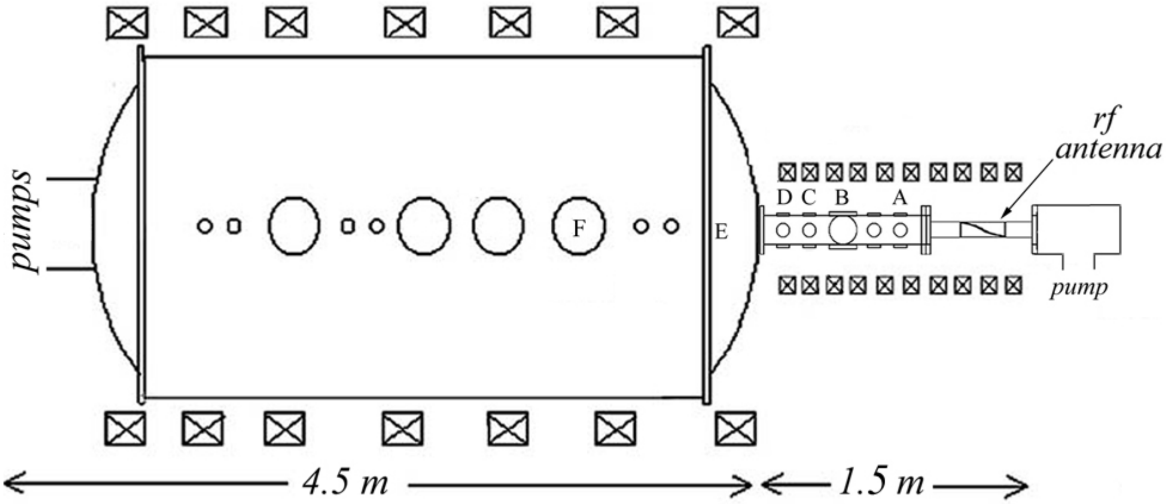

Figure 1-6. The plasma chamber and locations of diagnostics (at locations A, B, C, D, E, and F).

1.3.2 Vacuum System

The vacuum for the system is maintained by three turbomolecular drag pumps. The HELIX pumping station consists of a Pfeiffer TMU 520 turbomolecular drag pump connected to a Pfeiffer MD 4T diaphragm roughing pump. The pumping station at the far end of LEIA has two Pfeiffer TMU 1600 turbomolecular pumps with Pfeiffer MD-8 backing pumps. Each turbomolecular pump has two pumping speeds. For gas flow control, a MKS1179 mass flow valve with a PR-4000 flow controller is used to maintain the neutral pressure at the desired value. The controller can regulate the flow of argon, helium or a mixture of the two gasses.

1.3.3 The Magnetic Field

The HELIX magnetic field is created by ten electromagnets donated by the Max Planck Institüt in Garching, Germany. The water-cooled magnets have 46 internal copper windings with a resistance of 17 mΩ and an inductance of 1.2 mH. A Macroamp 400 Ampere power supply provides the current for the electromagnets. The magnetic field strength in HELIX can be varied from 0 to 1300 Gauss.

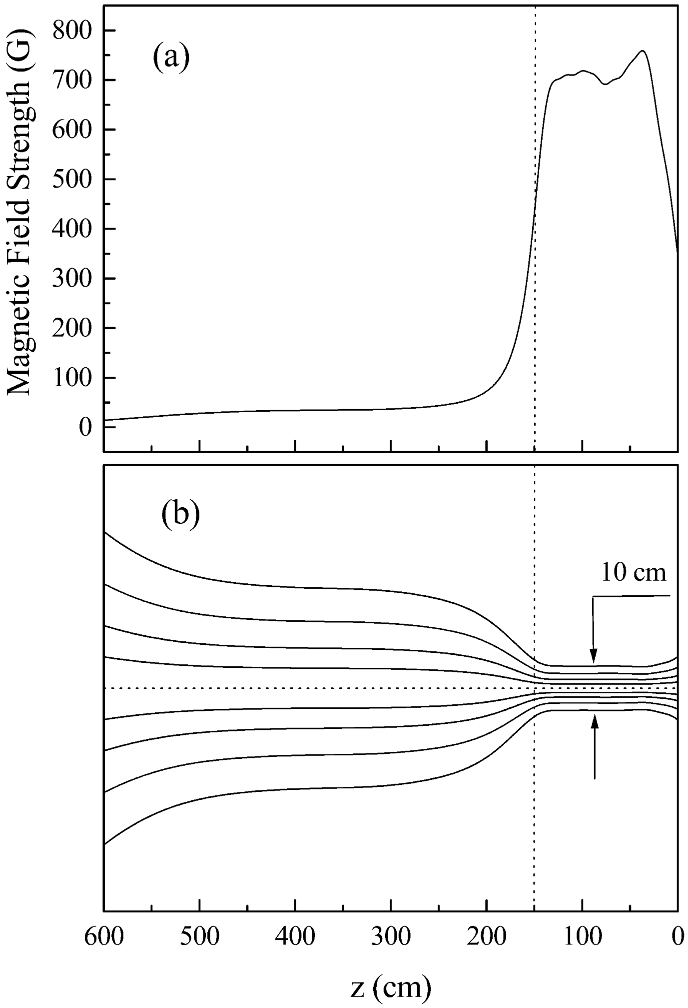

Figure 1-7. a) Axial magnetic field strength versus axial position in the combined HELIX/LEIA system. B) Contours of constant magnetic flux versus axial position. The outermost contours correspond to the plasma boundary in the source. The dashed vertical lines indicate the junction between the source chamber and the diffusion chamber.

The LEIA magnetic field is created by seven, custom built 9’ diameter electromagnets. For the experiments described here, each magnet contained 20 turns (2 layers of 10 turns) of water cooled, 0.36" x 0.41" hollow rectangular aluminum tubing. The total resistance of the seven magnets is 0.56 Ω. With a 200 Amp DC EMHP power supply, the LEIA magnetic field strength has a range of 0 to 74 Gauss. Fig. 1-7 shows the on-axial magnetic field in HELIX-LEIA calculated from a two-dimensional numerical model that was validated with single point measurements. The inhomogeneity in the magnetic field between 25 and 50 cm is due to displacement of the coils by the feeds for the rf antenna.

1.3.4 RF Generation and Matching

The rf system for HELIX consists of a 50 MHz Wavetek model-80 function generator that supplies the rf signal to an ENI 2000 amplifier with a bandwidth from 0.3 MHz to 35 MHz. The rf power is transmitted from the amplifier to the source via a high frequency coaxial cable and a *pi*-matching network. The matching network consists of one load and three tuning capacitors. The load capacitor is a Jennings high voltage tunable (20-2000 pF) capacitor. The three tuning capacitors (two with a range of 4-250 pF and one with a range of 5-500 pF) are all Jennings high voltage tunable capacitors. The three tuning capacitors are in parallel with each other and in series with the antenna. This combination is then in parallel with the load capacitor, as shown in Fig. 1-8.

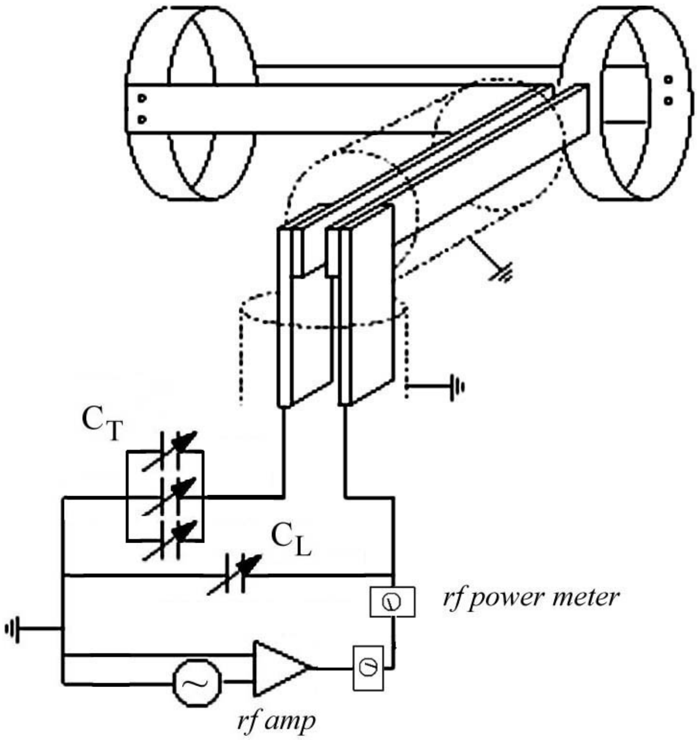

Figure 1-8. Antenna matching circuit for HELIX [57]

To maximize the antenna coupling efficiency, the real impendence of the matching network must equal the output impendence of the amplifier, $R_o = 50\ \Omega$, and the imaginary part of the combined matching network-antenna circuit must be zero. Denoting the load capacitance by C_L and the total tuning capacitance by C_T, the real resistance of antenna by R, and the reactance, ωL, by X, *Chen* [59] calculated the load and tuning capacitances for an inductive load to be

$$C_L = \frac{1}{2\omega R}\left[1-\left(1-\frac{2R}{R_o}\right)^2\right]^{1/2} \tag{1.15}$$

$$C_T = \left[\omega X - \frac{1-R/R_o}{C_L}\right]^{-1} \tag{1.16}$$

After the discharge is initiated, the effect of the inductive load of the plasma on the antenna has to be considered. For a typical helicon plasma source in the ‘inductive’ or ‘helicon’ mode, Eq. (1.16) becomes

$$C_T^{-1} = \omega^2 L - (1-R/R_o)/C_L$$

where L is the total inductance in the antenna portion of the circuit.

1.3.5 Antenna

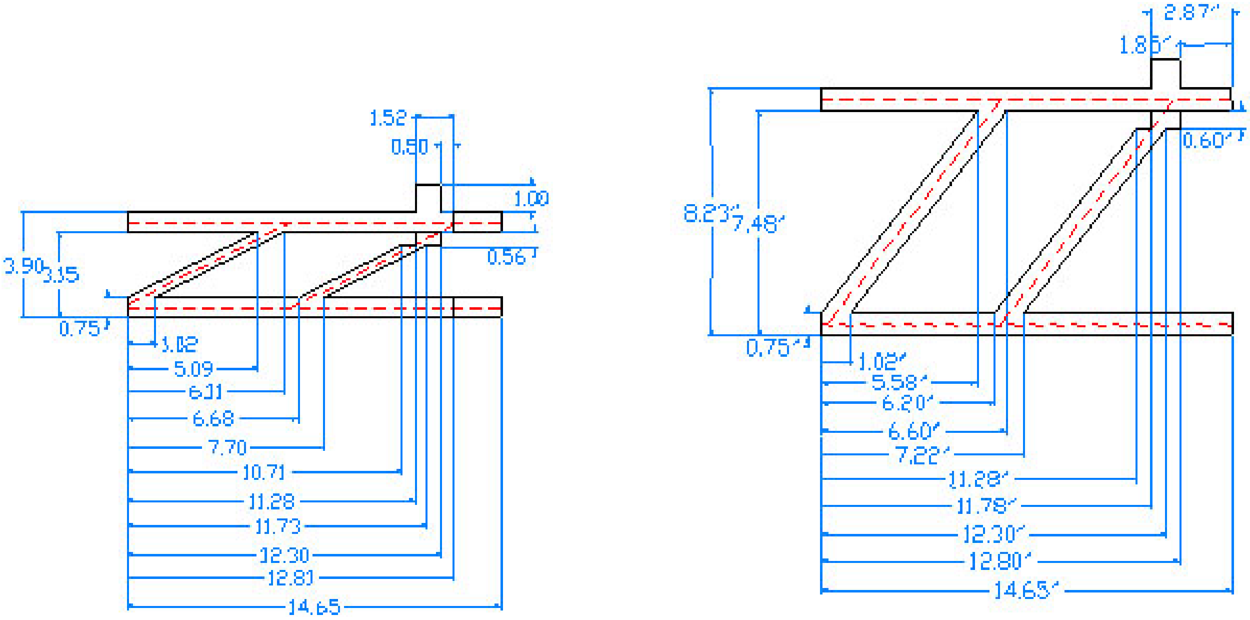

Figure 1-9. The 5 cm and 19 cm helical antenna with 1.9 cm wide copper straps.

Two helical antennas were made for launching the rf wave: 5 cm long and 19 cm long. Their dimensions are shown in Fig. 1-9. The antenna was wrapped around the Pyrex tube and right and left ends of the antenna joined together by two short screws. The transmission line used to connect the antenna to the matching circuit was both mechanically attached and silver-soldered onto the antenna. In this work, only the 19-cm antenna was used. The bounded whistler, helicon, waves have either right- or left-hand polarization. The left-hand polarization cannot propagate in the cylindrical chamber because the direction of magnetic field component generated by the displacement current is in the wrong direction for propagating of EM waves [60]. To determine the polarization of a helical antenna, one looks along the axis and imagines a circle drawn along the antenna helix. If the circle is drawn in a counterclockwise direction and magnetic field is same direction as the viewing direction, then the antenna is a R-type, or right circularly polarized, antenna. An example of such an antenna is shown in Fig.1-10.

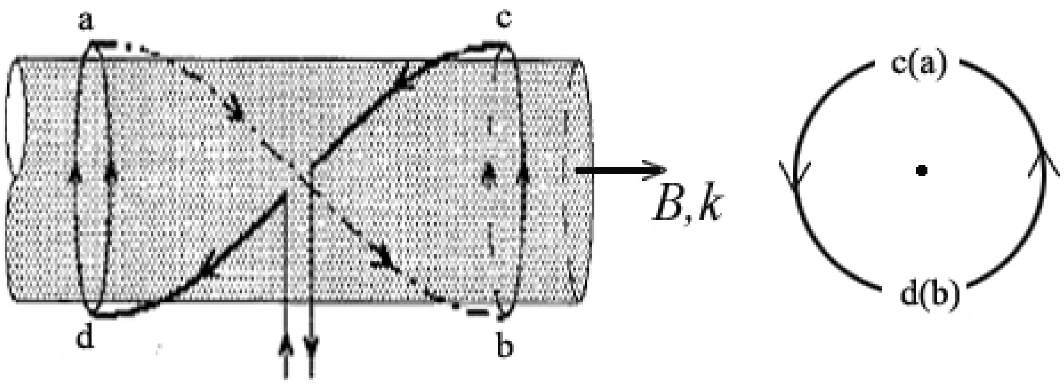

Figure 1-10 A diagram of m= +1 helical antenna. The left figure is from *Light and Chen* [61]. The point in the right figure represents the magnetic field and wave vector towards the reader. The arrow represents the direction of the twist in the antenna.

1.3.6 Typical Plasma Parameters in HELIX-LEIA

The typical operating parameters for HELIX are listed in Table 1.1

Parameter	Helicon Source (Ar)
Plasma lifetime	Steady-state
n	$>1\text{x}10^{19}$ m^{-3}
B	440 G – 1300 G
Pressure	1.5 mTorr – 10 mTorr
T_e	~5 eV
T_i	<1 eV
λ_D	$5\text{x}10^{-6}$ m
ρ_i	$1\text{-}4\text{x}10^{-2}$ m
ρ_e	~$9 \text{ x } 10^{-5}$ m
L (chamber length)	1.6 m
Ion β	~ $4 \text{ x } 10^{-4}$
f_{ce}	1.2 - 2.7 GHz
f_{ci}	16.7 – 49.7 kHz
ν_{in}	~ 2.8 kHz
f_{pe}	~ 28 GHz
f_{pi}	105 MHz

Table 1.1

Chapter 1 References

[1] L. D. Landau and E. M. Lifshitz, Fluid Mechanics, (Pergamon Press, 1959)

[2] W. M. Manheimer and R. F. Fernsler, IEEE Trans. Plasma Sci. **29**, 75 (2001)

[3] N. Hershkowitz, IEEE Trans. Plasma Science **22**, 11 (1994)

[4] L. P. Block, Astrophys. Space Sci. **55**, 59 (1978)

[5] H. Inuzuka, Y. Torri, M. Nagatsu, and T. Tsukishima, Phys. Fluids **28**, 703 (1985)

[6] Y. Takeda, and K. Yamgiwa, Phys. Rev. Lett. **55**, 711 (1985)

[7] N. Sato, R. Hatakeyama, S. Iizuka, T. Mieno, K. Saeki, J. J. Rasmusten, and P. Michelsen, Phys. Rev. Lett. **46**, 1330 (1981)

[8] S. Torvén, J. Phys. D: Appl. Phys. **15**, 1943 (1982)

[9] C. Chan, N. Hershkowitz, and T. Intrator, Phys. Rev. Lett. **52**, 1782 (1984).

[10] H. Alfvén, Tellus **10**, 104 (1958)

[11] C. E. McIlwain, J. Geophys. Res. **65**, 2727 (1960)

[12] R. D. Albert, and P. J. Lindstrom, Science **170**, 1398 (1970)

[13] M. A. Raadu, Physics Reports **178**, 25 (1989)

[14] I. B. Bernstein, F. M. Greene, and M. D. Kruskal, Phys. Rev. **108**, 546 (1957)

[15] S. Iizuka, K. Saeki, N. Sata, and Y. Hatta, Phys. Rev. Lett. **43,** 1404 (1979)

[16] C. Chan, N. Hershkowitz, and T. Intrator, Phys. Rev. Lett. **57,** 3050 (1986).

[17] T. Sato, and H. Okuda, Phys. Rev. Lett. **44**, 740 (1980)

[18] G. Knorr, and C. K. Goertz, Astrophysics and Space Science **31**, 209 (1974)

[19] O. Penrose, Phys. Fluids **3**, 258 (1960)

[20] N. Hershkowitz, Space Sci. Rev. **41**, 351 (1985)

[21] C. Chan, M. H. Cho, N. Hershkowitz, and T. Intrator, Phys. Rev. Lett. **52**, 1782 (1984)

[22] R. L. Stenzel, M. Ooyama, and Y. Nakamura, Phys. Rev. Lett. **45**, 1498 (1980)

[23] B. H. Quon, and A. Y. Wong, Phys. Rev. Lett. **37**, 1393 (1976)

[24] R. Hatakeyama, Y. Suzuki, and N. Sato, Phys. Rev. Lett. **50**, 1203 (1983)

[25] P. Coakley, N. Hershkowitz, R. Hubbard, and G. Joyce, Phys. Rev. Lett. **40**, 230 (1978)

[26] N. Hershkowitz, G. L. Payne, C. Chan, and J. DeKock, Plasma Physics **23**, 903 (1981)

[27] P. Coakley, and N. Hershkowitz, Phys. Fluids **22**, 1171 (1979)

[28] P. Coakley, and N. Hershkowitz, Phys. Lett. **83A** 131 (1981)

[29] Hairapetian G and Stenzel R L, Phys. Rev. Lett. **61**, 1607 (1988)

[30] Hairapetian G and Stenzel R L, Phys. Rev. Lett. **65**, 175 (1990)

[31] Hairapetian G and Stenzel R L, Phys. Fluids B **3**, 899 (1991)

[32] F. S. Mozer, C. W. Carlson, M. K. Hudson, R. B. Torbert, B. Parady, J. Yatteau, and M. C. Kelley, Phys. Rev. Lett. **38**, 292 (1977)

[33] M. Temerin, K. Cerny, W. Lotko, and F. S. Mozer, Phys. Rev. Lett., **48**, 1175 (1982)

[34] E. L. Bennett, M. Temerin, F. S. Mozer, and M. H. Boehm, Geophys. Res. Lett. **88**, 7107 (1983)

[35] R. Boström, G.Gustafsson, B. Holback, G. Holmgren, H. Koskinen, and P. Kintner, Phys. Rev. Lett. **61**, 82 (1988)

[36] R. Boström, IEEE. Tran. Plasmas **20**, 756 (1992)

[37] R. E. Ergun, L. Anderson, D. Main, Y. –J. Su, C. W. Carlson, J. P. McFadden, and F. S. Mozer, Phys. Plasmas **9**, 3685 (2002)

[38] A. J. Hull, J. W. Bonnell, and F. S. Mozer, J. Geophys. Res. **108**, 1265 (2003)

[39] J. L. Burch, Adv. Space Res. **8**, 353 (1988)

[40] J. P. McFadden, C. W. Carlson, and M. H. Boehm, J. Geophys. Res. **95**, 6533 (1990)

[41] M. K. Hudson, et. al., J. Geophys. Res. **88**, 916 (1983)

[42] R. W. Boswell, Phys. Lett. **33A**, 457 (1970)

[43] P. A. Keiter, E. E. Scime, M. M. Balkey, R. Boivin, J. L. Kline, and S. P. Gary, Phys. Plasmas **7**, 779 (2000)

[44] A. J. Perry and R. W. Boswell, Appl. Phys. Lett. **55**, 148 (1989)

[45] J. Hanna, and C. Watts, Phys. Plasmas **8**, 4251 (2001)

[46] F. R. Chang Diaz, et. al., Fusion Technol. **35**, 243 (1999)

[47] F. Chang-Diaz, R. H. Goulding, R. D. Bengtson, F. Wally-Baity, D. Sparks, R. G. Bussell Jr., C. G. Barber, G. McCaskill, V. T. Jacobson, M. D. Carter, A. V. Ilin, and T. W. Glover, Fusion Technol. **35**, 243 (1999)

[48] J. P. Squire, F. R. Chang Diaz, T. W. Glover, V. T. Jacobson, D. G. Chavers, R. D. Bengtson, E. A. Bering, R. W. Boswell, R. H. Goulding, and M. Light, Fusion Sci. Technol. **43**, 111 (2003)

[49] J. T. Scheuer, K. F. Schoenberg, R. A. Gerwin, R. P. Hoyt, I. Henins, D. C. Black, R. M. Mayo, and R. W. Moses Jr, IEEE Transactions on Plasma Science **22**, 1015 (1994)

[50] C. Charles and R. W. Boswell, Appl. Phys. Lett. **82**, 1356 (2003)

[51] C. Charles and R. W. Boswell R W, Phys Plasmas **11**, 1706 (2004)

[52] C. Charles, Appl. Phys. Lett. **84**, 332 (2004)

[53] S. A. Cohen, N. S. Siefert, S. Stange, R. F. Boivin, E. E. Scime, and F. M. Levinton, Phys. Plasmas **7**, 2593 (2003)

[54] R. F. Boivin and E. E. Scime, Rev. Sci. Instrum. **74**, 4352 (2003)

[55] I. D. Kaganovich, V. A. Rozhansky, L. D. Tsendin, and I. Yu. Veselova, Plasma Sources Sci. Technol. **5**, 743 (1996)

[56] P. Keiter, Ph. D Dissertation, West Virginia University (1999)

[57] M. Balkey, Ph. D Dissertation, West Virginia University (2000)

[58] J. Kline, Ph. D Dissertation, West Virginia University (2002)

[59] F.F. Chen, UCLA Internal Report PPG-1401 (1992)

[60] F. F. Chen, Phys. Plasma **3**, 1783 (1996)

[61] M. Light, and F. F. Chen, Phys. Plasma **2**, 1084 (1995)

Chapter 2: Diagnostics

2.1.1 Langmuir Probe

Perhaps the most natural approach to measuring plasma parameters is to insert some kind of probe into the plasma that directly senses the quantities of interest. Indeed, this approach is one of the oldest in plasma diagnostics and is associated with the name of Irving Langmuir for his investigations of the operation of the electric probe known as the Langmuir probe. A Langmuir probe is essentially a biased conductor that draws current when inserted into the plasma. The relationship between the bias voltage and the collected current is referred to as an I-V characteristic, or an I-V trace. An ideal I-V trace is shown in Fig. 2-1.

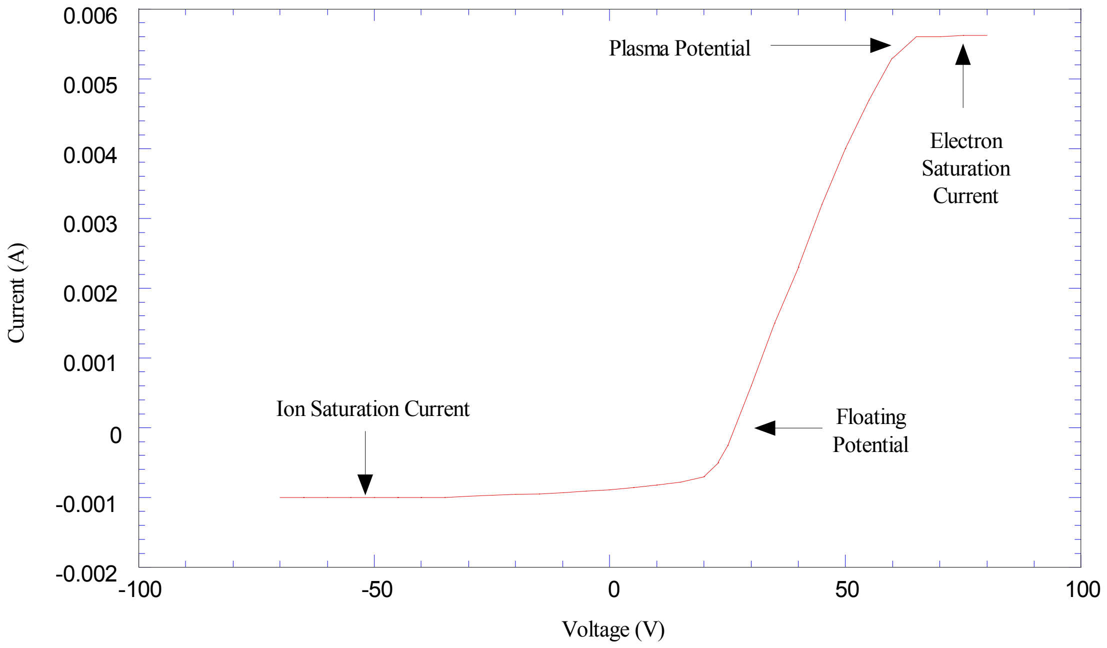

Figure 2-1: Ideal Langmuir probe trace [1,2,3].

If a conducting probe is electrically insulated from ground and other parts of the plasma device (a "floating" probe), then it would rapidly charge up negatively until the electrons were repelled and the net electrical current to the probe is zero. The electrical potential of a floating probe, the floating potential, is denoted V_f. The floating potential is not the electric potential of the plasma. This latter potential is called the plasma or space potential, and is denoted V_p. If the probe is at the plasma potential, the collected current is nearly the maximum electron current possible. If the applied voltage is increased well above the plasma potential, the collected electron current saturates because all the arriving electrons are collected (see Fig. 2-1). Decreasing the applied potential to V with $V<V_p$, the probe is negative with respect to the ambient plasma and electrons without enough energy to overcome the potential difference will be repelled while more ions will be collected. Further reducing the applied potential, the ion current will equal the electron current at the floating potential V_f. For applied potentials more negative than the floating potential, the probe will collect more ions than electrons and eventually the collected ion current also saturates.

Assuming the plasma is collisionless, the particle distribution is Maxwellian and there is no magnetic field, the current in the region around floating potential (the knee in the curve in Fig. 2-1) can be approximated by [4],

$$I\left(V_o - V_p\right) = n_\infty e A_p \left(\frac{kT_e}{m_i}\right)^{1/2} \left[\frac{1}{2}\left(\frac{2m_i}{\pi m_e}\right)^{1/2} \exp\left(\frac{e(V_o - V_p)}{kT_e}\right) - \frac{A_s}{A_p}\exp\left(-\frac{1}{2}\right)\right] \qquad (2.1)$$

where m_e is the electron mass, m_i is the ion mass, A_s is the area of the sheath, A_p is the surface area of the probe and V_o is the applied voltage. To zeroth order, the ratio A_s / A_p is equal to 1 if the probe size is much larger than the Debye length. The sheath is the region of spatially varying potential and is created when the ions in the plasma Debye shield the potential applied to the probe. The two unknowns in Eq. 2.1 are n_∞, the electron density far from the probe, and T_e, the electron temperature. The derivative of the current with respect to the bias voltage is

$$\frac{dI}{d(V_o - V_p)} = \frac{e}{kT_e}(I - I_{si}) + \frac{dI_{si}}{d(V_o - V_p)} \tag{2.2}$$

where $I_{si} = -eJ_i$ and

$$J_i = 0.61 n_\infty A_p \sqrt{(kT_e/m_i)} \tag{2.3}$$

Since the ion saturation current, I_{si}, is small compared to the current collected by the probe when biased above the floating potential, $dI \big/ d(V_o - V_p) >> dI_{si} \big/ d(V_o - V_p)$, T_e can be approximated by

$$T_e = e(I - I_{si}) \Big/ \frac{dI}{d(V_o - V_p)} \tag{2.4}$$

Once the electron temperature is obtained from the slope of the I-V characteristic, it is straightforward to use Eq. 2.3 to calculate the electron density of the plasma from the probe, i.e., well outside the Debye shielded region.

The plasma potential can be determined from the bias voltage at which the I-V characteristic begins to enter electron current saturation. However, a cylindrical probe cannot achieve complete electron current saturation because the actual collection area (A_s) increases with the applied voltage. The increase in collection area occurs because the thickness of sheath around the probe increases at high applied voltages. More electrons orbiting around the probe fall onto the probe at higher voltages and the collected electron current never saturates. Furthermore, because of the relatively high densities in helicon sources, the magnitude of the electron saturation current is sufficient to overwhelm the current handling capability of the rf compensation circuit. RF compensation involves the use of bypass capacitors and series rf chokes to reduce pickup from the rf antenna [5]. An alternative approach to determining the plasma potential can be obtained by setting Eq. 2.1 equal to zero, i.e., setting the applied potential to the floating potential,

$$\frac{e(V_f - V_p)}{T_e} = \frac{1}{2}[\ln(2\pi \frac{m_e}{m_i}) - 1]. \tag{2.6}$$

For argon plasma, this relationship is approximated by [6,7]

$$V_p \approx V_f + 5.2T_e \tag{2.7}$$

Unlike cylindrical or spherical probes, the collection area of planar probe does not change significantly at large positive bias voltages. The sheath still thickens, but the collection area of the probe (the cross-sectional area of the sheath) does not increase. Thus, a planar probe can reach electron current saturation current particularly if the probe diameter is much larger than the Debye length. For plasma potential measurements, the planar probe shown in Fig. 2-2 was constructed. The probe is made of tungsten sheet cut into a circle to avoid sharp edges and tungsten rod. The diameter of the disk is ¼”, which is at least 100 times larger than the Debye length. One side of the probe surface is coated with alumina powder to limit current collection to one side of the disk. The tungsten rod, length 0.97”, is shielded from the plasma with an alumina tube. The length of stainless steel shaft on which the probe is mounted is 83¾” so that the probe can be inserted into LEIA through a rotating port and reach the junction between the HELIX and LEIA chambers. Similar to the standard rf-compensated Langmuir probes used in HELIX and LEIA, an rf choke is placed in series with the probe tip to eliminate rf pickup [5].

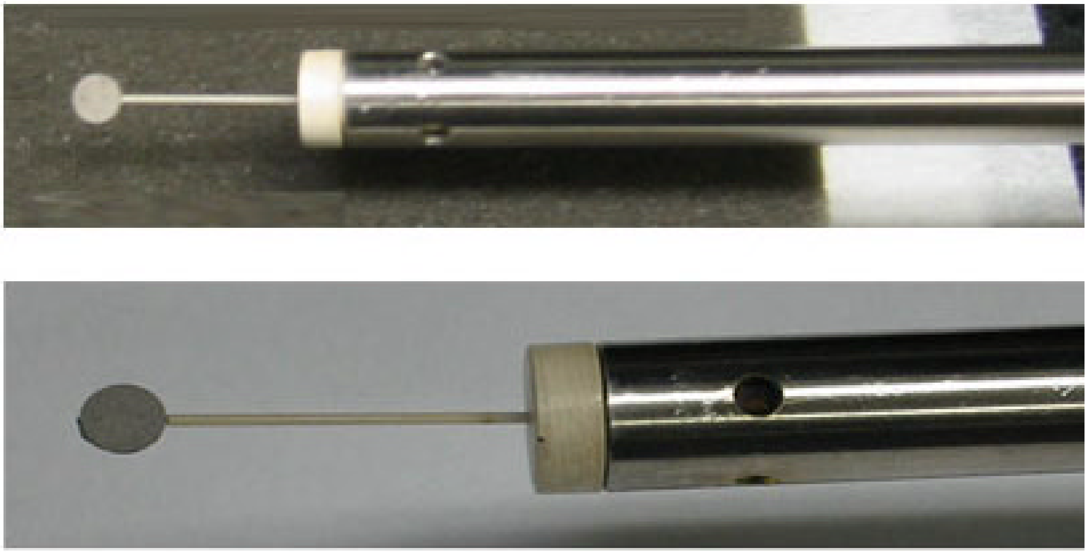

Figure 2-2. Photographs of the planar Langmuir probe. The top picture shows the coated side and the lower picture shows the uncoated side of the probe surface.

2.1.2 Magnetic Fluctuation Probe

The simplest way to measure the fluctuating magnetic field at a point in the plasma is with a small loop of wire. According to the Faraday' s law, the time-dependant magnetic field passing through a coil of wires will induce a voltage: $V(t) = NAdB(t)/dt$ where N is the number of turns on the coil, A is the area of each turn and $dB(t)/dt$ is the magnitude of the time derivative of the magnetic field.

If the induced voltage is measured over a time period, a time series of the fluctuating magnetic field will be recorded. Using Fourier analysis, the frequency spectrum of the magnetic fluctuation can then be determined. The induced voltage is usually very small. For instance, for the magnetic coil used in LEIA (with an effective area of 5×10^{-5} m^{-2} at a frequency of 20 kHz) and a magnetic field fluctuation amplitude of 10 Gauss at 20 kHz, the induced voltage around the coil is several mV. To measure such low voltage signals and reduce electrostatic pickup, the two ends of the coil are connected to a differential amplifier (Tektronix 4780) through two co-axial cables. The amplified signals are low pass filtered at 100 kHz to prevent aliasing and recorded with a Tektronix 4244 waveform analyzer sampling at 200 kHz.

2.1.3 Laser Induced Fluorescence (LIF)

In a laser-induced fluorescence (LIF) measurement of the ion velocity distribution function (IVDF) in a plasma, the frequency of a narrow line-width, tunable laser is scanned across an absorption line of an ion in the plasma and fluorescent emission from the excited state measured as a function of laser frequency. For LEIA and HELIX parameters, the only significant line broadening mechanisms are Zeeman splitting and thermal Doppler broadening [1,2,3,8,9]. In the presence of a magnetic field, Zeeman splitting yields linearly polarized π lines ($\Delta m = 0$) and circularly polarized σ lines ($\Delta m = \pm 1$) for absorption between the initial state and the upper state, see Fig.2-3 (a) and (b) for details of the Zeeman splitting for the primary 611 nm and 668 nm absorption lines used in this work. The π lines are symmetrically distributed around the zero magnetic field transition. The σ lines include two clusters of lines, σ+ and σ-. The amplitude envelope of each σ+ or σ- cluster is asymmetric, but each cluster is symmetrically distributed around the central line. The shifted in frequency of each cluster from the central line depends linearly on the magnetic field strength. The measured shift of theσ clusters can be used to determine the strength of the magnetic field at the measurement location.

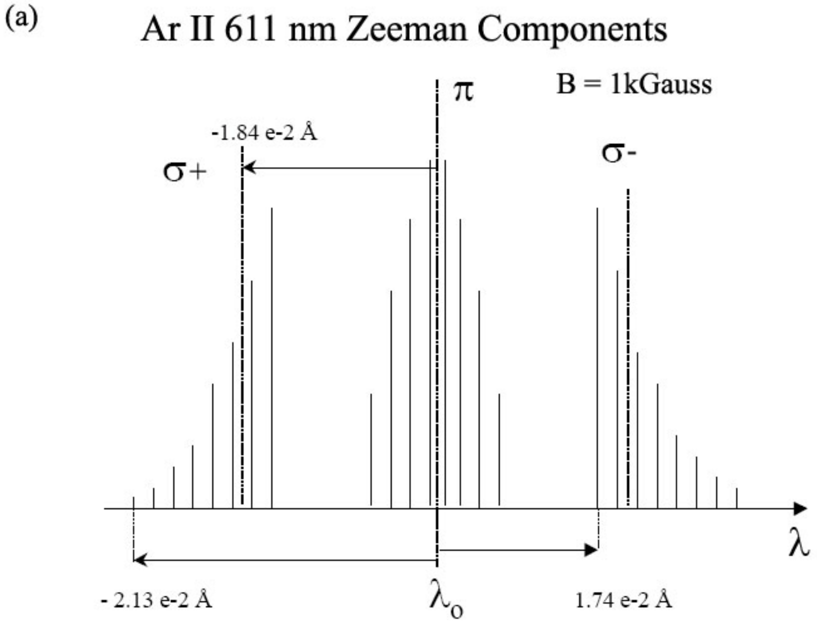

Figure 2-3a. Schematic of the σ, and π transitions for the 611.6616 nm argon ion absorption line. The height of each line corresponds to the statistical weighting of each transition as a function of wavelength.

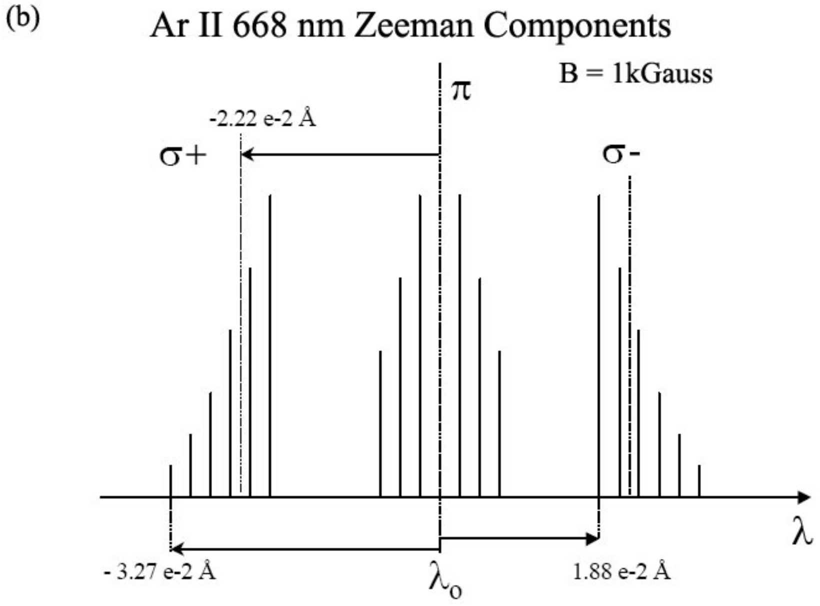

Figure 2-3b. Schematic of the σ, and π transitions for the 668.6136 nm argon ion absorption line. The height of each line corresponds to the statistical weighting of each transition as a function of wavelength.

Due to ion motion along the laser injection direction, all the absorption lines are Doppler shifted. The line broadening resulting from random thermal motion is used to measure the temperature of the ions along the laser injection direction and the overall shift of the absorption line provides a measure of the bulk ion flow speed along the laser direction. In these experiments, the laser light is injected either perpendicular or parallel to the magnetic field lines. In the case of perpendicular injection, the polarization of the laser light is oriented parallel to the magnetic field line to excite only the π lines. In the case of parallel injection, the laser light is either right or left circularly polarized light to excite only one of σ line clusters

2.1.3.1 Ring Dye Laser

For the ring dye laser, the LIF scheme used is shown in Fig. 2-4.

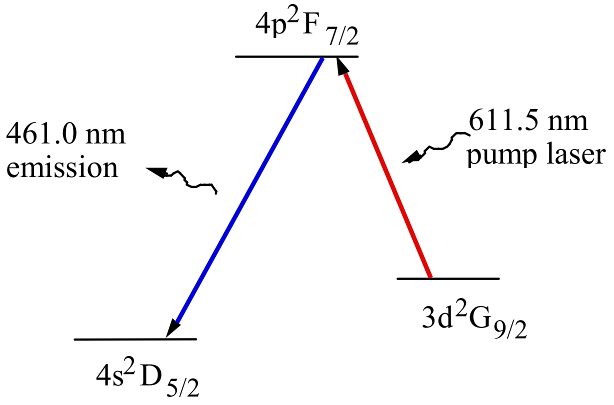

Figure 2-4. LIF scheme for dye laser

The single mode output of laser light was tuned at 611.66 nm to pump Ar II ions from the metastable state $3d^2G_{9/2}$ to the upper state $4p^2F_{7/2}$. Ions $4p^2F_{7/2}$ state then decay to the $4s^2D_{5/2}$ state by emitting a 461.09 nm photon. Before being coupled into a fiber optic cable for transport to the plasmas, ten per cent of the dye laser light is passed through an iodine cell for a consistent zero velocity reference. Spontaneous emission from the iodine cell is recorded with a photodiode for each scan of the dye laser wavelength.

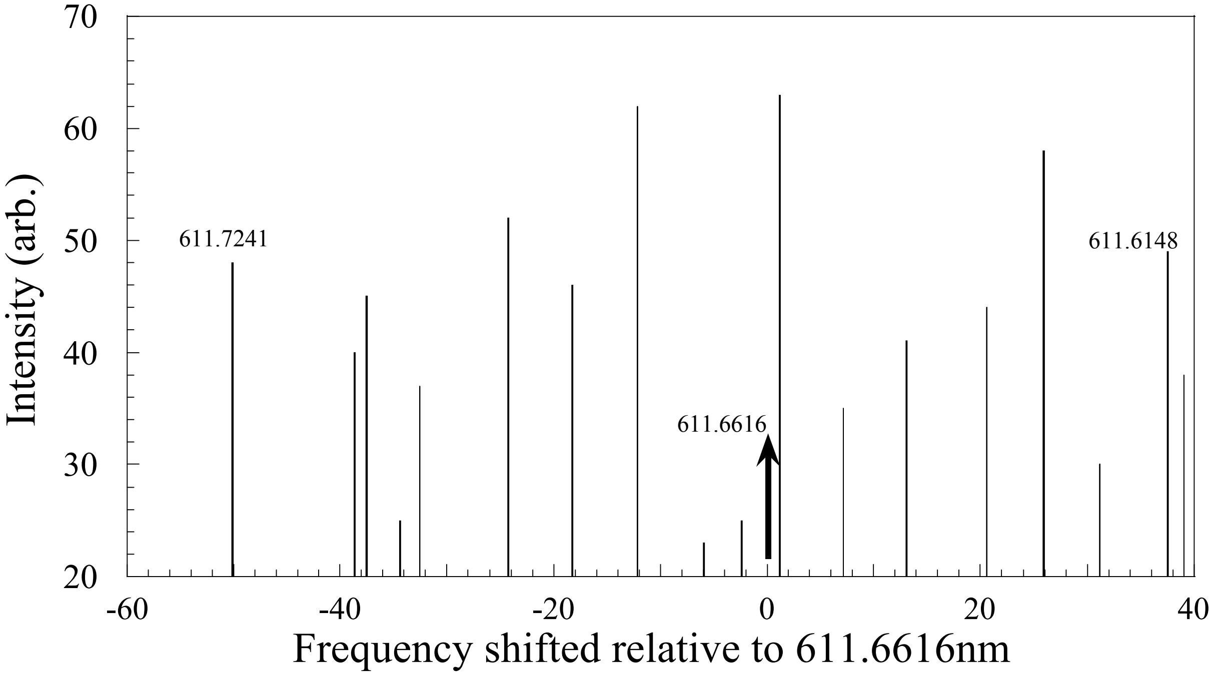

Figure 2-5: Iodine spectra for the range of +40 GHz and –60 GHz relative to 611.66 nm

Fig.2-5 shows the iodine spectra in vacuum near 611.6616 nm. The units of the three numbers in the figure are nm. The origin of the axis is the natural absorption wavelength 611.6616 nm. The frequency scan width of the laser can be varied up to 30 GHz. Drift of the electronic laser control circuit can affect the accuracy of the laser scan width. However, the actual scan width can be determined from the measured iodine spectrum. For these experiments, the actual laser scan width in GHz was equal to the scan width setting on the laser controller divided by 1.11. After passing through the beam splitter and a mechanical chopper, the bulk of the laser light is coupled into a multimode, non-polarization preserving fiber optic cable. The chopper frequency serves as a reference for a Stanford Research SR830 lock-in amplifier that eliminates all the non-correlated signals except the noise at the chopper frequency. To minimize the $1/f$ noise, the chopper frequency is usually operated at a few kilohertz. The fiber optic cable transports the laser light from the laser laboratory into the helicon source laboratory, where several sets of laser injection and light collection optics are mounted on the

HELIX and LEIA chambers. Figure 2-6 shows the experimental configuration for dye laser LIF measurements. The parallel injection optics includes a combined linear polarizer and quarter-wave plate optical element that converts the unpolarized laser light into either right or left circular polarized light. The perpendicular injection optics includes a linear polarizer to select only laser light with polarization parallel to the magnetic field direction. The fluorescence light, together with the background light, is focused into a fiber optical cable by the collection optics. The fiber used in these experiments has a numerical aperture (NA) equal to 0.22. Numerical aperture is a characteristic of a specific fiber and describes the cone angle of light that can enter the fiber. For maximum coupling of the collected light into the fiber, the focal length f and the diameter D of the convex lens in the collection optics just before the fiber should satisfy the relationship $D/2f < \sin^{-1}(\mathrm{NA})$. So for a 2.54 cm diameter lens, the focal length should be larger than roughly 5 cm. The collected light is then transported to a filtered (1 nm bandwidth centered at 460 nm) photomultiplier tube (PMT). The PMT assembly used in these experiments is a Hamamatsu HC124-06mod. The PMT type is R6095, which has a spectral range from 300 nm and to 650 nm with peak sensitivity at 420 nm. For the R6095 PMT, the current amplification (gain) as a function of supply voltage V is $\mu = K \cdot \left(V/(n+1) \right)^{\alpha n}$, where n is the number of dynodes (equal to 11 for the R6095). α and K are determined by the dynode material and geometric structure. In these experiments, the applied voltage ranged from 500 to 1000 V, which yielded a PMT gain of 10^4 to 2×10^6 [10].

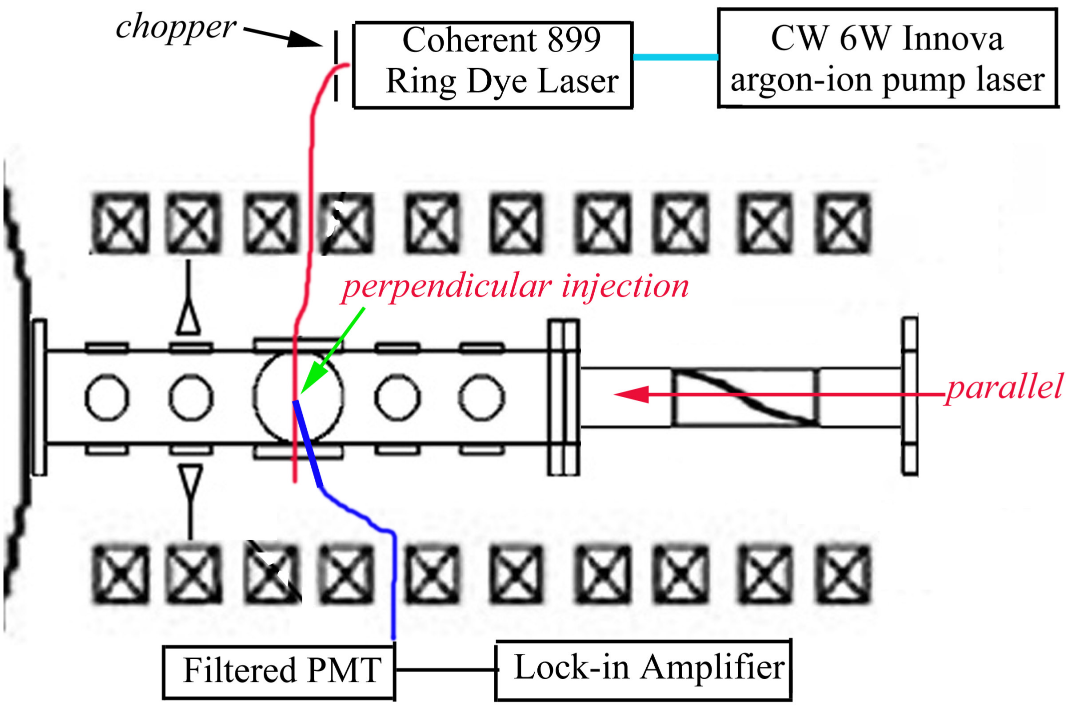

Figure 2-6: The experimental configuration of the laser and optics for LIF measurements in the plasma source.

The PMT output voltage is then sent to the input of a SR 830 lock-in amplifier. The time constant (integration time) on the lock-in for these experiments was set to 100 or 300 ms and the laser scan time was at least 30 sec. Longer integration time constants improve the signal-to-noise at the expense of time resolution (Table 2-1 gives the settling time for different time constant values [11]). The reduced time resolution compromises measurements of the IVDF full width at half maximum (FWHM) and absolute frequency shift, so the in practice the time constant was reduced until the measured FWHM became independent of the value of the lock-in time constant.

Slope	ENBW	Settling time
6dB/oct	1/(4T)	5T
12 dB/oct	1/(8T)	7T
18 dB/oct	3/(32T)	9T
24 dB/oct	5/(64T)	10T

Table 2-1: The settling time in multiples of the lock-in time constant for various choices of the order of the filter pole (slope). Also listed is the effective noise bandwidth for each order of the filter pole.

2.1.3.2 Diode Laser

The LIF scheme for the diode laser is shown in Fig. 2-7.

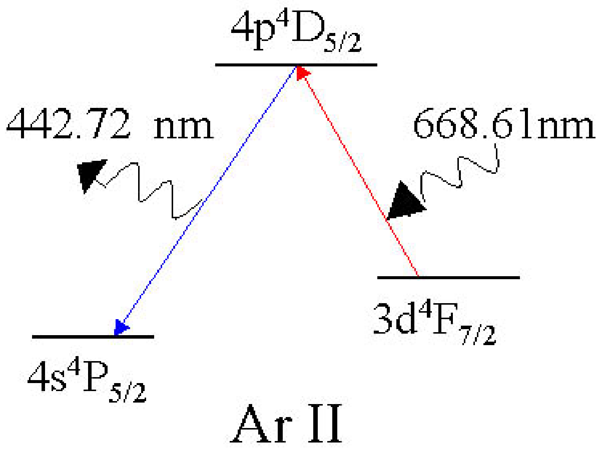

Figure 2-7: LIF scheme for diode laser based LIF measurements in argon.

The diode laser is manufactured by Sacher LaserTechnik [12] and can be coarse tuned from 662 to 674 nm with bandwidth 1.5 MHz. The laser light is generated by sending a current through the active region of the diode located between the *n*- and *p*-type cladding layers. The injected current produces electrons and holes, which in turn recombine and emit photons. The photon energy is determined by the electron energy in the conduction band and the hole energy in valence band. In contrast to the gas laser, the excited state (conduction band) and ground state (valence band) are continuous energy bands for optical transitions in semiconductors. Fine tuning the wavelength of the laser is accomplished by changing the diode temperature (increasing the diode temperature shifts the cavity modes and the wavelength at maximum gain towards higher wavelengths) or changing the characteristics of an external resonant cavity. Scanning the laser by temperature modification is impractical because the laser takes several minutes stabilize at each new temperature setting. The laser intensity is also a strong function of temperature (increasing temperature increases the threshold current to lase, thus the laser intensity decreases at fixed laser current), thus temperature scanning also leads to unacceptable variations in laser intensity during a wavelength scan. Thus, external cavity tuning is preferred .for fine tuning.

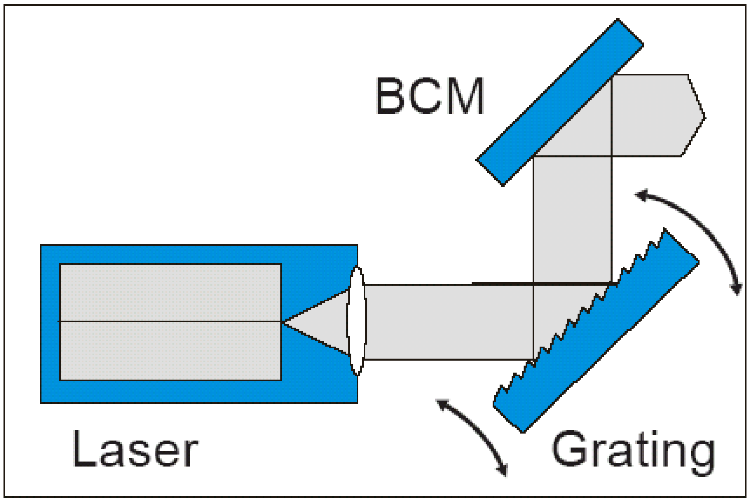

Figure 2-8: Schematic of diode laser [12].

Two possible external cavity configurations are currently available: Littrow or Littman. In the Littrow configuration, tuning is achieved by rotating the angle of the external diffraction grating. The Littrow cavity offers more output power at the expense of tuning range. In the Littman configuration, tuning is achieved by tilting a separate tuning mirror. The Littman cavity is a double pass grazing incidence cavity that naturally achieves multimode suppression. The Littman configuration typically has larger mode-hop free tuning range but at the expense of output power. Because of the crucial importance of laser power for LIF measurements, we choose a Littrow cavity diode laser (Fig. 2-8). Laser power output from diode is inversely proportional to the reflectivity of the front facet of the diode chip. To increase the output power of the Littrow laser, Sacher added an anti-reflection coating to front facet. The anti-reflection coating also increases the total tuning range of the laser. To minimize feedback into the internal cavity as the laser output is coupled into the external cavity, a low efficiency grating is employed.

In the Littrow configuration, the external cavity has two elements that determine the laser wavelength: the cavity length and the grating. The grating angle is varied by changing the voltage on the piezoelectric (PZT) crystal on which the grating is mounted. The grating directs the first order diffraction beam back into laser chip and acts as a frequency filter. Only the wavelength selected by the grating can form a standing wave in the cavity can survive and be amplified in the lasing medium. To achieve a mode-hop-free wavelength scan, the gratings and cavity length must be synchronously tuned. Sacher provides a current-compensation operating mode to synchronize these tuning these two tuning elements. By changing the injection current, and thereby changing the temperature and effective length of the diode chip, during the wavelength scan, the laser mode-hop-free tuning range is significantly increased from 8 GHz to 15 GHz. To compensate for changes in the laser direction that arise as the grating angle is changed during a wavelength scan, a beam correction mirror (BCM) is attached to the grating so that it compensates for the movement of the grating (see Fig. 2-8). With the BCM, the total shift of the laser beam is on the order of one micrometer. Example tuning curves for a scan of the PZT crystal voltage and a scan of the diode temperature scan are shown in Fig. 2-9 and 2-10. A 15 GHz mode-hop-free range is easily achieved with a PZT voltage scan.

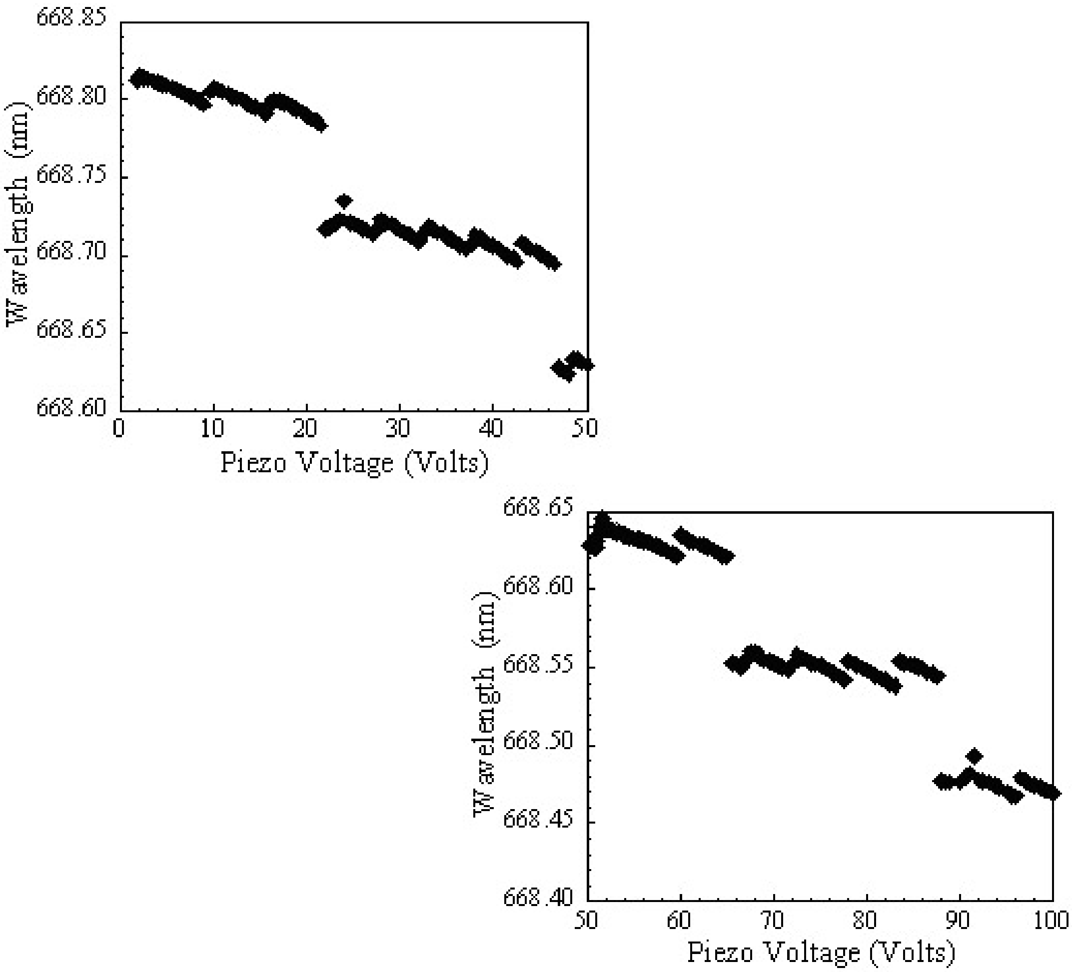

Figure 2-9: Tuning curve of Sacher diode laser. The temperature is set at 21.2^{o}C.

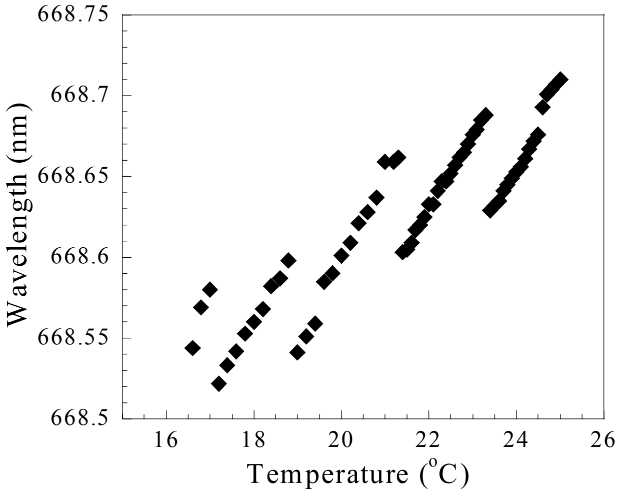

Figure 2-10: Tuning curve of Sacher diode laser. The piezo voltage is set at 50V.

2.1.3.3 LIF Amplitude and Plasma Density

An important result of recent LIF measurements in HELIX is the observation that the total LIF signal is roughly proportional to the square of the plasma density times the square root of the electron temperature. Therefore, although the LIF system is not absolutely calibrated, the LIF signal amplitude provides a non-invasive measure of qualitative changes in the plasma density in argon helicon plasmas. Although the relationship between the total LIF signal and ion density is complex, if the metastable ions interrogated via LIF are created by electron impact excitation of ground state ions, the LIF signal intensity should be roughly proportional to the square of the plasma density [13,14];

$$n^2 = n_i n_e \approx \frac{n_j}{\langle \sigma v \rangle_{0j}} \sum_{i<j} A_{ij} \tag{2.8}$$

where n is the plasma density, n_i the ion density, n_e the electron density, n_j the density of ions in the metastable state, j, probed with the laser (proportional to the total LIF signal), $\langle \sigma v \rangle_{0j}$ is the velocity distribution averaged cross section for electron impact excitation from the ion ground state into state j, and $\sum_{i<j} A_{ij}$ is the sum of the spontaneous transition rates from the metastable state to all lower states. The assumption that transitions from other metastable states are not significant source of the interrogated metastable ions is equivalent to claiming that the ion state populations in argon helicon plasmas can be calculated with a Steady State Coronal (SSC) model [15]. In support of this assertion, the LIF intensity in the helicon source as a function of rf driving frequency and radial position is compared to the square of the Langmuir probe measured plasma density times the square root of the electron temperature (as suggested by Eq. (2.8)) in Fig. 2-11 (a) and (b), respectively. That the trends in the LIF and Langmuir probe measurements are remarkably similar indicates that LIF intensity measurements can be used a qualitative measure of changes in the source plasma density. Perhaps more importantly, the similarity between the LIF and Langmuir probe measurements suggests that the high collisionality of high density argon helicon plasmas rapidly de-populates the

ion metastable states and those metastable ions observed with LIF are locally and recently created via electron impact excitation of ground state ions.

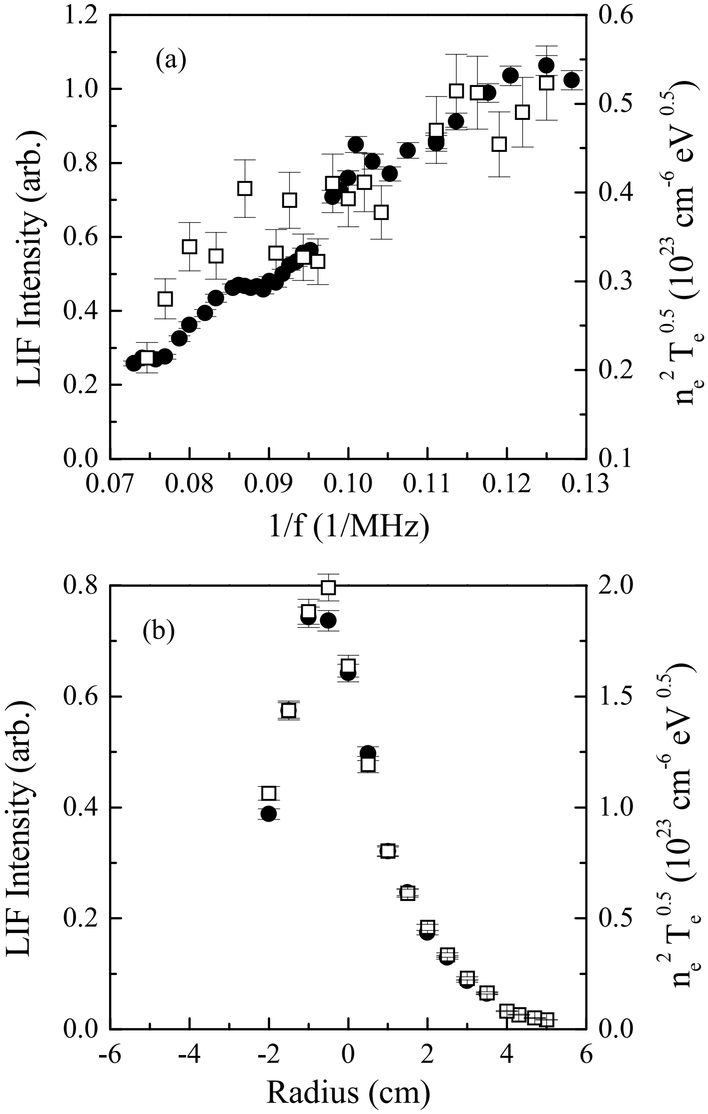

Fig. 2-11 For a rf power of 750 W, B_H = 730 G, and B_L = 34 G the LIF intensity (solid circles) and the square of the plasma density times the square root of the electron temperature (open squares) (a) versus rf driving frequency and (b) verses radial position in HELIX. The frequency scan was performed at a neutral pressure of 1.2 mTorr and the radial scan at a neutral pressure of 1.8 mTorr.

2.2 Scanning Internal Probe (Superprobe)

The scanning internal probe installed in LEIA is designed to obtain spatially resolved measurements throughout a horizontal plane 100 cm in length along the *z*-axis and 40 cm wide in the radial direction. As shown in Fig. 2-12, the measurement area begins in the divergent magnetic field region near the HELIX-LEIA junction and extends to the middle of the LEIA chamber.

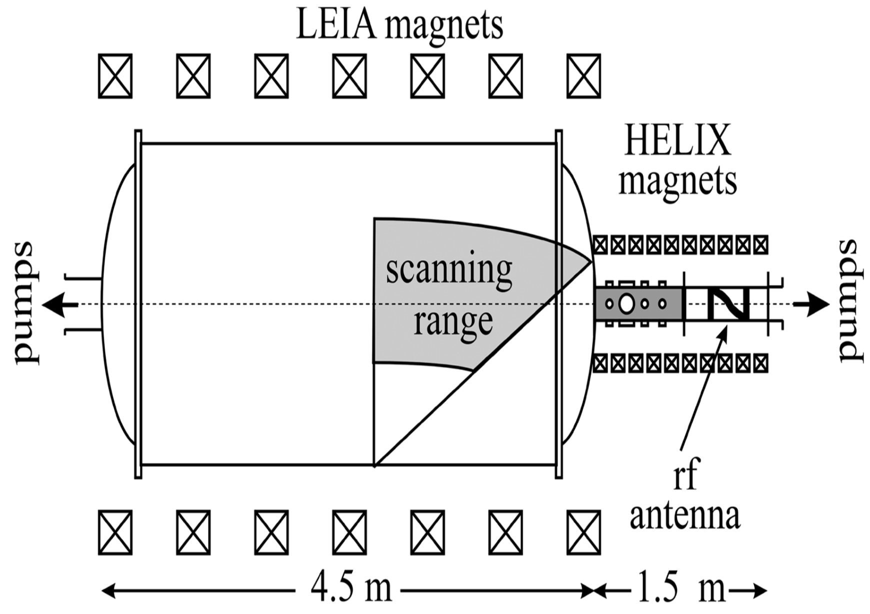

Fig 2-12: The combined HELIX-LEIA system with the region accessible with the scanning probe shaded in gray [16].

The backbone of the probe is a 6’ long, ¾”-o.d. stainless steel shaft with 0.083”-thick walls supported by a stainless steel ball joint bearing mounted on the interior of the feedthrough flange. The bearing is captured in a stainless steel ring supported on a ½” threaded shaft. The ring is free to rotate around the axis of the threaded shaft. Two linear motion bearings mounted on a fixed 1”-o.d. guide shaft align and support the heavy probe shaft as it passes through a double o-ring sliding seal. The double o-ring sliding seal consists of a modified ¾” Cajon^{TM} fitting with two Viton^{TM} o-rings separated by an intermediate vacuum region evacuated through a ¼” port. In combination with the ball joint bearing and the rotating supporting shaft, a welded bellows provides for ± 35° of angular motion of the probe. The feedthrough flange and vacuum seals are described in detail in Ref. [17]. The bearings, vacuum fittings, and bellows are readily available from commercial vendors.

Placement of the probe shaft in the *z-r* plane is accomplished by two computer-driven VELMEX^{TM} stepping motor assemblies that control the insertion depth of the probe and the tilt angle between the probe and the chamber axis. A VELMEX^{TM} rotary stepping motor spins the probe shaft around its axis to switch between parallel and perpendicular (with respect to the magnetic field) LIF measurements and for optical tomography. The spatial and angular resolutions are determined by the precision of the stepping motors and are ≈ 1 mm and ≈ 0.5°, respectively.

The diagnostic complement mounted on the probe head (Fig. 2-13a) includes: laser induced fluorescence (LIF) optics [18,19,20], an rf compensated cylindrical Langmuir probe [21] and a 3D magnetic sense coil array [4]. When inserted into the plasma, the LIF interrogation volume is upstream of the Langmuir probe, which is upstream of the magnetic sense coil array. Thus, the most perturbative component of the probe, the magnetic sense coil array, is the last part of the probe to interact with the plasma flowing out from HELIX. The previous internal LIF probe suffered from poor signal-to-noise, was limited to scans along a single radial chord, and was solely a LIF probe [22]. To improve the LIF single-to-noise, this probe includes optimized collection optics including light baffles, an easily aligned and replace-able mirror for laser injection, and an integrated photomultiplier tube (PMT) detector.

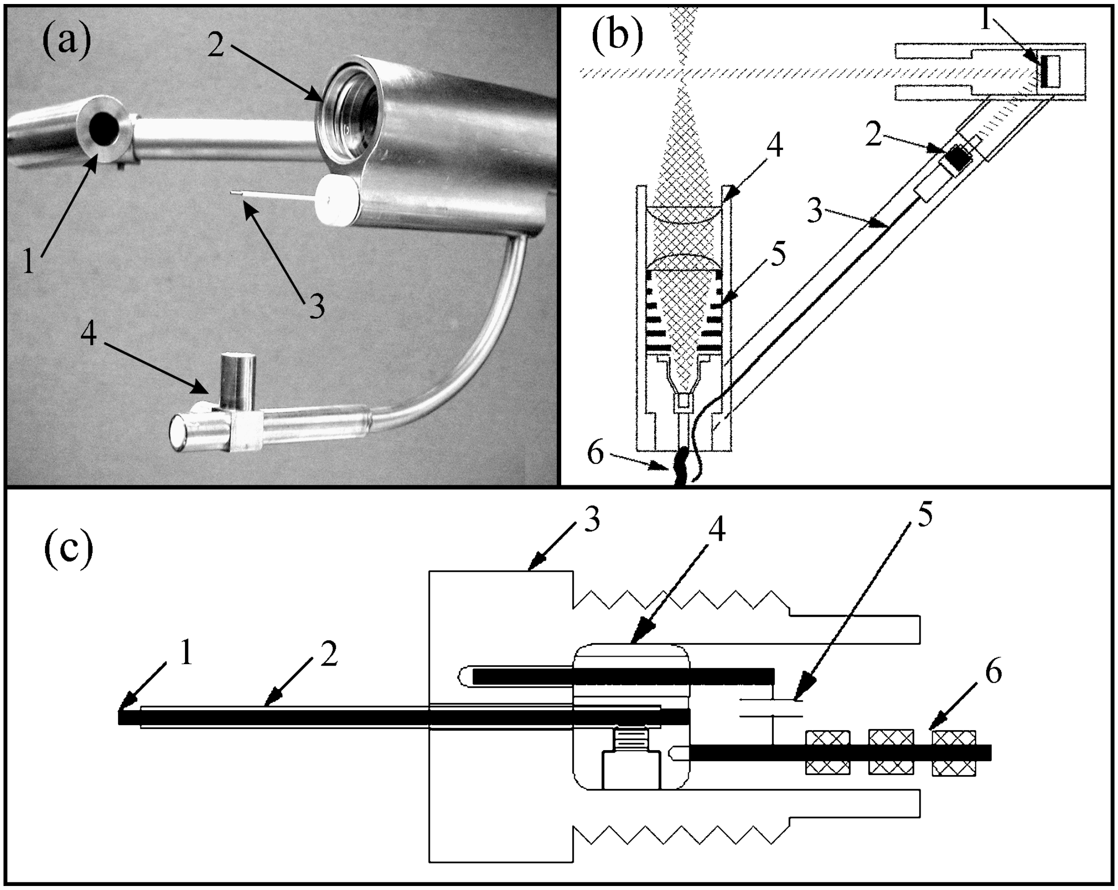

Fig 2-13: Scanning probe head diagnostics: (a) 1—LIF injection optics;2—LIF collection optics; 3—rf compensated Langmuir probe; 4—3D magnetic sense coil array. (b) 1—injection mirror; 2—collimating injection optic; 3—injection fiber; 4—collection lens; 5—light baffles; 6—collection fiber. (c) 1–0.5 mm graphite rod; 2—alumina tube; 3—boron nitride cap;4—brass slug; 5—10 nF shorting capacitor; 6—rf choke chain. [16]

For argon ion LIF, laser light is coupled into the internal 200 μm fused silica fiber through a fiber-fiber vacuum feedthrough. The injection fiber is terminated with a ¼" collimating lens to create a weakly divergent beam that reflects from a plane mirror and passes 5 cm in front of the collection optics (Fig. 2-13b). The power of the final scanning probe beam is approximately 40% of the output power of the ring dye laser. To ensure proper alignment of the injection and collection optics, the probe head was machined from a single piece of stainless steel. Before final cutting, the injection optics shafts and mirror mount were mechanically aligned to the probe head with a jig and the injection optics shafts welded into place. Then the pockets for the collection optics and the Langmuir probe were machined into the probe head.

The 2.54 cm diameter collection optics consists of a 5 cm focal length collection lens followed by a 5 cm focal length focusing lens. The numerical aperture of the focusing lens was chosen to match the numerical aperture of the 1 mm core diameter, 2 m long, fused silica collection fiber (NA = 0.22). Between the focusing lens and the collection fiber, a series of circular apertures (shown in Fig. 2-13b) prevent off-axis rays from passing through the lenses and into the collection fiber. Because the plasma emits strongly at the fluorescence wavelength, reduction of background light is critical to improving the measurement signal-to-noise. To avoid loss of fluorescence light at another fiber-fiber vacuum feedthrough, the collected light is coupled into a Hamamatsu HC124-06 PMT [10] mounted on the end of the probe shaft. Light exiting the collection fiber is collimated inside the probe, passes through a standard quartz fused silica window, a 1 nm wide interference filter (centered around 461 nm) and into the PMT. The PMT moves with the probe as it scans through the measurement plane in LEIA. The total lengths of injection and collection fiber optic cables are 2.1 and 1.8 m, respectively.

Measurements of the plasma density, electron temperature, and floating potential are accomplished with an rf compensated, cylindrical Langmuir probe. To withstand the intense thermal environment of a steady-state helicon plasma, the probe consists of a 0.5 mm diameter graphite rod, standard mechanical pencil graphite, surrounded by an alumina tube. 3 mm of the graphite protrudes from the alumina tube for particle collection. Electrical connection to the probe tip and the rf compensating electronics is made through a brass slug; to which the graphite rod, alumina tube, 10 nF shorting capacitor, and rf chokes are attached (Fig. 2-13c). One lead of the shorting capacitor nearly penetrates the boron nitride shield of the probe and serves to short out high frequency electrostatic fluctuations that are picked up by the graphite tip. A series of five Lenox-Fugle rf chokes, [23] covering the frequency range 6-18 MHz, provide additional rf rejection between the probe tip and the Keithley 2400 Sourcemeter used to sweep the probe tip voltage from -20 V to + 50 V. High pressure bulkhead mount BNC fittings, modified for high vacuum use, are used as inexpensive signal feedthroughs for the Langmuir probe and the magnetic sense coils at the sealed end of the scanning probe.

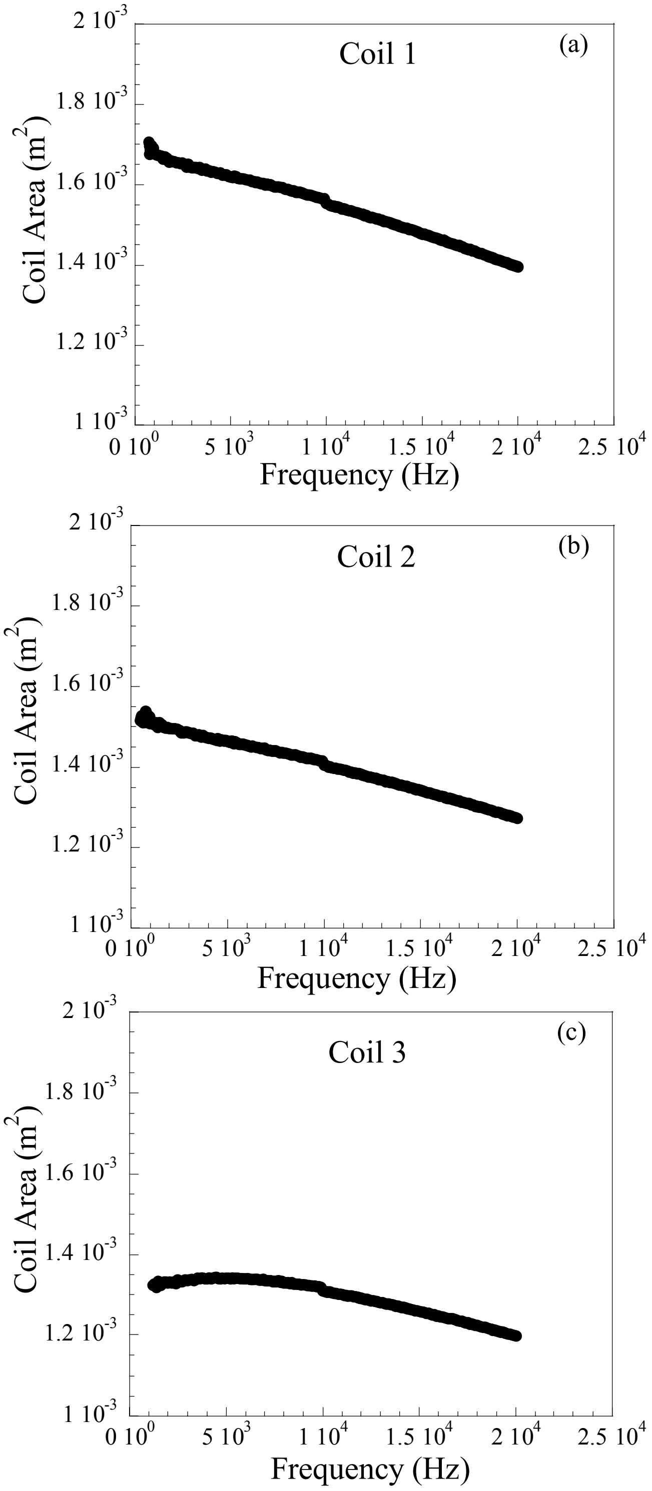

Figure 2-14: Effective area of each magnetic sense coil in the superprobe as a function of signal frequency.

Measurement of the spectrum and amplitude of electromagnetic fluctuations over the frequency range 1 to 100 kHz in the expanding helicon source plasma was another design goal of the scanning probe. Each of the three magnetic sense coils is made from 300 turns of 40 HML gauge, coated copper wire (MWS Wire Industries) wound on a 7 mm long, 3 mm diameter boron nitride reel. The sense coils are enclosed in three, mutually perpendicular cylinders machined from a single block of stainless steel and welded to the end of a precision 90° bend of ¼" stainless steel tubing that was welded to the main probe head. Electrostatic shielding along the axis of each coil is accomplished with a thin piece of aluminum foil placed under the protective boron nitride cap.

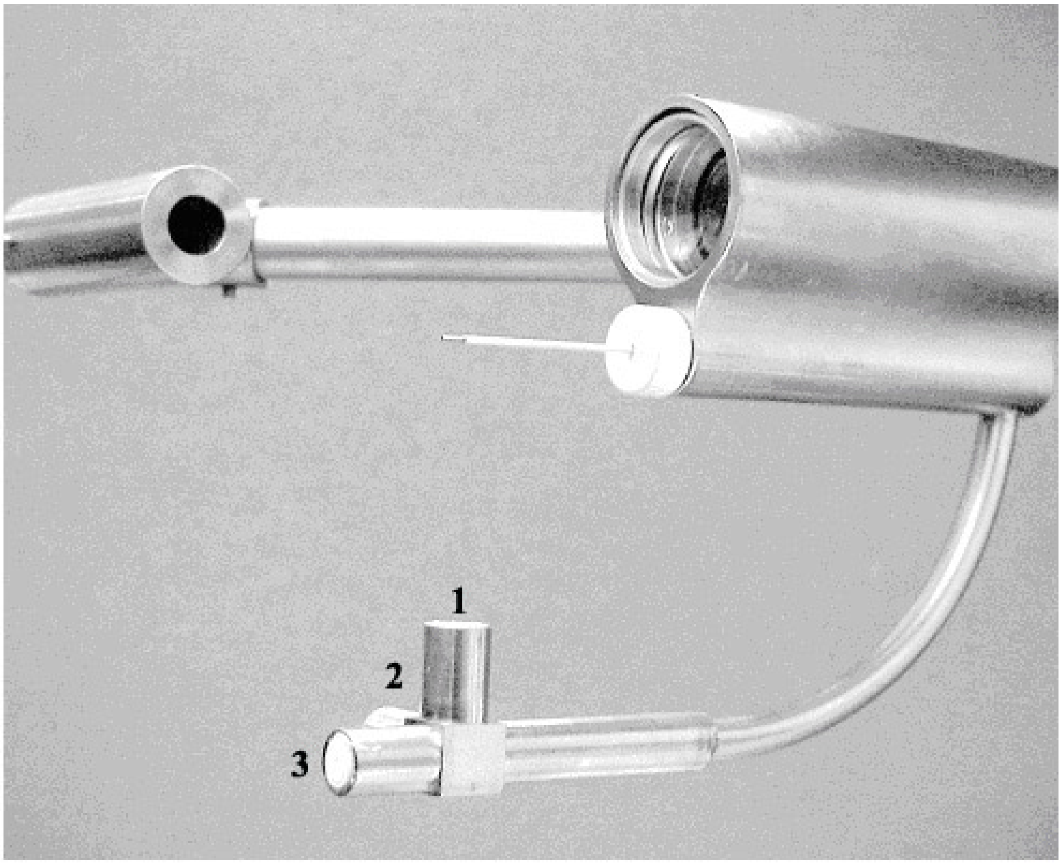

Figure 2-15: The corresponding coils in the internal scanning probe (superprobe) for coils labels #1,#2, and #3.

The effective coil area (*NA*) as a function of signal frequency is shown in Fig. 2-14 for all three coils. The effective coil area is given by $NA(\omega) = V(\omega)/\omega B$, where the magnetic field B is provided by a calibrated solenoid, ω is the frequency of the current through the solenoid, and $V(\omega)$ is measured voltage signal from coil. Each coil is identified by location on the probe array in the photograph shown in Fig. 2-15. For future checking of sense coil properties, it is worth noting that coil #3 has a resistance of 28.6 Ω and both coil #1 and #2 have resistances of 32.2 Ω. Signals from both leads of the coils are low-pass filtered at 100 kHz with a 16 channel, differential amplifier and recorded with a 200 kHz, 16 channel, 16 bit digitizer (Tektronix VX4780 and VX4244, respectively).

2.3 Angular Motion Vacuum Feedthrough

In addition to the superprobe feedthrough assembly, another rotatable feedthrough was constructed for use with Langmuir and other probes in LEIA (Fig. 2-16). The feedthrough design was based on schematics available in Ref. [24]. For compatibility with existing probe hardware at WVU, the feedthrough was been modified to use a QF-40 flange instead of a QF-50 flange. The ball, sealed with two O-rings, enables angular motion of the probe and linear motion is provided by a double O-ring seal that is connected to the end of the ball by the QF-40 flange.

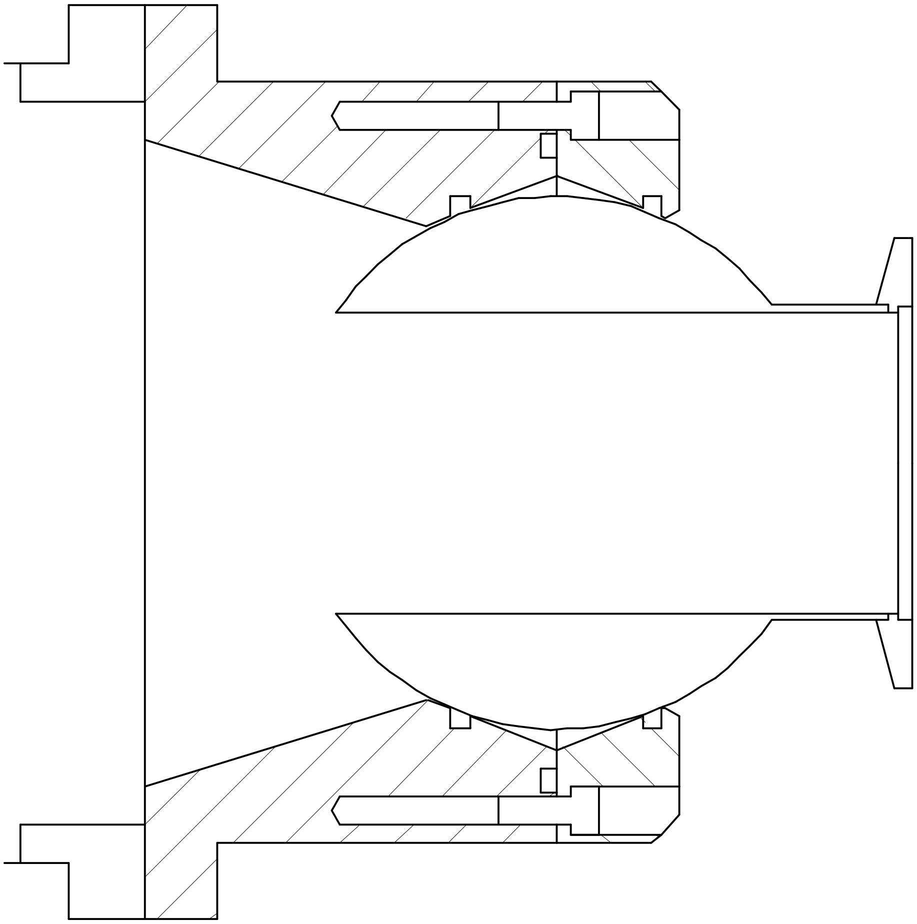

Figure 2-16: Mechanical drawing of the UCLA tilting port as modified for use at WVU

Chapter 2 References

[1] P. Keiter, Ph. D Dissertation, West Virginia University (1999)

[2] M. Balkey, Ph. D Dissertation, West Virginia University (2000)

[3] J. Kline, Ph. D Dissertation, West Virginia University (2002)

[4] I. H. Hutchinson, Principles of Plasma Diagnostics (Cambridge University Press, Cambridge 1987)

[5] I D. Sudit, and F. F. Chen, Plasma Sources Sci. Technol. **3**, 162 (1994).

[6] F. F. Chen, Mini-Course on Plasma Diagnostics IEEE-ICOPS Meeting (Jeju, Korea, June 5, 2003)

[7] M. Lieberman, and A. Lichtenberg Principles of Plasma Discharges and Materials Processing (New York: Wiley, 1994)

[8] R. Boivin, West Virginia University Plasma Physics Lab Report No. PL-039 (December 2000)

[9] R. Boivin, West Virginia University Plasma Physics Lab Report No. PL-050 (December 2001)

[10] Hamamatsu Co., Technical Datasheets, http://www.usa.hamamatsu.com

[11] Stanford Research Systems, SR844 RF Lock-in Amplifier Manual

[12] Sacher LaserTecknik, http://www.sacher-laser.com

[13] R. Boivin, West Virginia University Plasma Physics Lab Report No. PL-046 (December 2000)

[14] H. R. Griem, Principles of Plasma Spectroscopy, (Cambridge University Press, 1997)

[15] R. W. P. McWhirter, Spectral intensities, in Plasma Diagnostics Techniques (Academic Press, New York, 1965)

[16] C. Biloiu, E. Scime, and X. Sun, Rev. Sci. Instrum. **75**, 4296 (2004)

[17] E. E. Scime, J. L. Kline, D. Mathess, and C. Weber II, Rev. Sci. Instrum. **73** 1970 (2002)

[18] R. A. Stern and J. A. Johnson III, Phys. Rev. Lett. **34**, 1548 (1975)

[19] D. H. Hill, S. Fornaca, and M. G. Wickham, Rev. Sci. Instrum. **54**, 309 (1983)

[20] R. F. Boivin and E. E. Scime, Rev. Sci. Instrum. **74**, 4352 (2003)

[21] I. D. Sudit and F. F. Chen, Plasma Sources Sci. Technol. **3**, 162 (1994)

[22] E. E. Scime, Paul A. Keiter, S. Peter Gary, Matthew M. Balkey, Robert F. Boivin, J. L. Kline, and M. Blackburn, Phys. Plasmas **7,** 2157 (2000)

[23] Lenox Fugle Inc., Product Catalog, http://www.brotherselectronics.com

[24] D. Leneman, and W. Gekelman, Rev. Sci. Instrum. **72**, 3473 (2001)

Chapter 3: Double layer measurements in HELIX-LEIA

3.1: Parallel velocity and ion temperature measurements in HELIX

In the HELIX-LEIA system, the helicon plasma is produced in HELIX and expands into LEIA. The LEIA neutral pressure is typically 10 times lower than the neutral pressure in HELIX. Investigations of high-density plasmas expanding into a vacuum or into a low-density background plasma date back to the 1930s when researchers observed high velocity plasma jets in low-pressure dc discharges [1,2]. Later experiments demonstrated acceleration of ions to supersonic speeds during plasma expansion [3, 4, 5] and some researchers have reported detailed measurements of both electron and ion velocity distribution functions during the expansion process in a pulsed plasma [6, 7, 8]. As discussed in Ref [8], the physics of expanding plasmas plays a key role in a wide range of phenomena: in the filling of the wake region behind objects moving supersonically through a plasma [9]; in laser-fusion experiments when the laser heated target material expands away from the target [10]; and in the expansion of ionospheric plasma into the magnetosphere along the earth's magnetic field [11]. Laboratory experiments designed to probe the details of expanding plasmas have employed pulsed plasma sources [6, 7, 8], Q-machines with shaped magnetic fields [12,13], cathode-anode plasma sources [14], and triple plasma devices [15,16]. Interest in controlling the characteristics of expanding plasmas has been on the rise as expanding plasmas have become more common in plasma processing systems and plasma thrusters.

The high plasma densities and the possibility of either supplying an independent bias to the sample substrate or allowing the sample to electrically float make helicon sources potentially attractive plasma processing sources. Typically, the sample to be processed is placed into a diffusion chamber connected to the helicon source. The plasma then expands from the strong magnetic field region of the source into the weaker magnetic field of the diffusion chamber. For materials processing applications involving deposition, surface modification, or etching, control of the ion temperature, ion speed, plasma density, and uniformity in the expanding plasma is of paramount importance. Researchers have shown that in the diffusion chamber, charge-exchange-collisions associated with plasma expansion reduce the average energy of the ions impinging on a substrate. Thus, by operating at neutral pressures of several mTorr, helicon plasma sources have been used to generate uniform plasma fluxes with a high plasma density and reduced ion energies at the substrate location in the diffusion chamber [17, 18, 19]. Arrays of compact helicon plasma sources have also been shown to produce uniform plasmas over large surface areas [20]. For plasma etching, high etching rates (1.5 μm/min) with a minimum anisotropy of 0.97 were obtained with an expanding SF_6 helicon plasma [21]. Control of both ion flow speed and ion temperature in the expanding plasma would provide important additional capabilities in a helicon source based etching system.

Recently, double layers were observed in two different rapidly expanding helicon plasmas when operated at low neutral pressure: Chi-Kung at Australia National University [22] and the Magnetic Nozzle eXperiment (MNX) at Princeton Plasma Physics Laboratory [23]. In Chi-Kung, double layers were observed in both argon and hydrogen plasmas [24]. Evidence for double layer formation in both systems came from measurements of ion beams and in Chi-Kung, measurements of the plasma potential profile along the axis of the source. In this work, measurements of the parallel ion velocity distribution function in expanding HELIX plasmas (see Fig. 1-6 and Fig. 1-7 for location of the measurements) reveal that double layers also spontaneously form in HELIX. Because the ion beam energy measurements in the low density Chi-Kung plasmas relied on potentially perturbative retarding field energy analyzer probe measurements and optical access to the double layer region in MNX was restricted, HELIX is an ideal experimental facility in which to investigate double layer formation in helicon plasmas. In this chapter, ion flow speed measurements in HELIX and LEIA as a function of plasma source parameters are presented and the double layer measurements at the interface of HELIX and LEIA described in detail.

3.1.1 Effects of RF Driving Frequency

The parallel ion speed and parallel ion temperature measured on axis at location C (z = 126 cm) versus the rf driving frequency for an rf power of 750 Watts and a neutral pressure of 1.2 mTorr is shown in Fig. 3-1. The magnetic field in HELIX, B_H, was 730 Gauss and the lower hybrid frequency on axis $\omega_{ch} \approx \sqrt{\omega_{ce}\omega_{ci}} \approx 8MHz$, where ω_{ce} and ω_{ci} are the electron and ion cyclotron frequencies respectively. Since the plasma density decreases towards the edge of the source, the ion plasma frequency term in the full lower hybrid frequency calculation becomes significant and the lower hybrid frequency at the plasma edge is smaller than on axis [25]. Apart from a slight increase (≈10%) at rf driving frequencies just above the lower hybrid frequency on axis, the parallel ion flow speed of ≈1000 m/s and parallel ion temperature of 0.7 eV are independent of the rf driving frequency. At higher neutral pressures (≈ 4 mTorr), the parallel ivdf is collisionally coupled to the perpendicular ivdf and significant ion heating occurs for rf driving frequencies equal to the lower hybrid frequency at the plasma edge [26].

As already shown in Fig. 2-11a, the LIF intensity (estimated plasma density) and the measured plasma density increase with decreasing driving frequency in these low pressure helicon discharges. The slight increase (decrease) in the LIF intensity (plasma density) for rf driving frequencies close to the lower hybrid frequency (ω_{LH}) on axis ($1/f \approx 0.11$ MHz^{-1}) is reminiscent of changes in the power coupling into the source observed at higher neutral pressures (≈ 4 mTorr) for $\omega \approx \omega_{LH}$ [25]. However, the overall inverse scaling of plasma density with rf driving frequency is only observed at low neutral pressures (< 3 mTorr) and is consistent with the helicon wave dispersion relation. For a fixed magnetic field strength and fixed parallel and perpendicular wavelengths, the simple helicon wave dispersion relation for a homogeneous, small aspect ratio ($L >> a$, where L is the length of the system and a is the plasma radius), helicon source [27],

$$n = \frac{B_0 k_{\|}}{\omega \mu_0 e \alpha}, \tag{3.1}$$

predicts an inverse relationship between plasma density and rf driving frequency, where $\alpha(r)^2 = k_{\parallel}^2 + k_{\perp}^2$, $k_{\parallel}$ and $k_{\perp}$ are the parallel and perpendicular wave numbers respectively, B_0 is the source magnetic field, μ_0 is the free space permeability, e is the electron charge and n is the electron density.

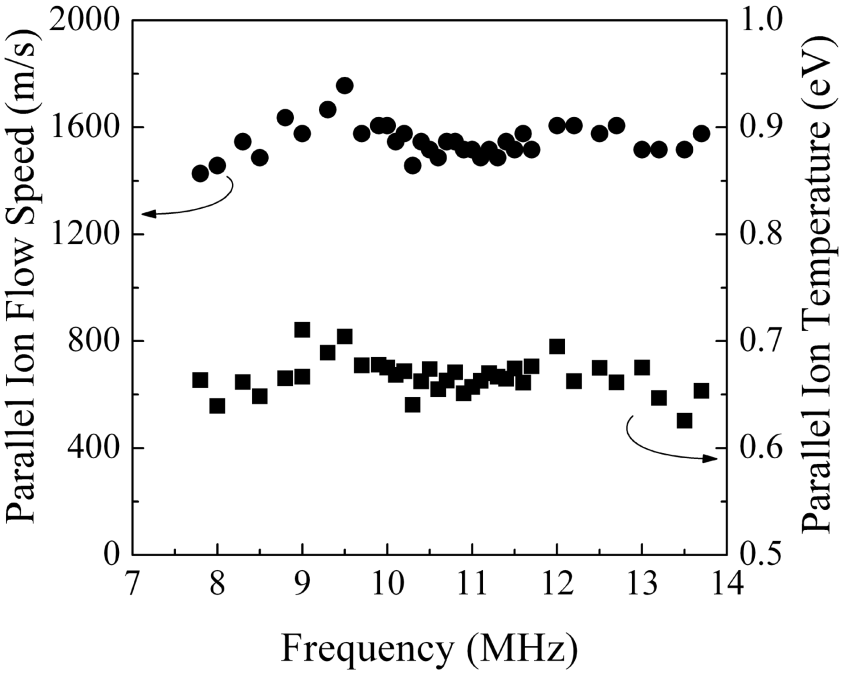

Figure 3-1. Parallel ion flow speed (solid circles) and parallel ion temperature (solid squares) versus rf driving frequency. The measurements were taken at location C (z = 126 cm) for a rf power of 750 W, B_H = 730 G, B_L = 34 G, and neutral pressure of 1.2 mTorr in HELIX.

3.1.2 Effects of RF Power

For a fixed rf driving frequency of 9.5 MHz, and a source magnetic field of 730 G, the rf power was varied from 250 W to 1000 W for two different neutral pressures: 1.2 and 1.7 mTorr as measured in the middle of the source chamber (corresponding to pressures of 2.0 and 3.1 mTorr at the gas inlet in the helicon source). The parallel ion flow speed was measured on the source axis at z = 126 cm (location C) for the 1.2 mTorr case and at z = 146 cm (location D) for the 1.7 mTorr case (Fig. 3-2a). In both cases and at both locations, there is a general trend of increasing flow speed with increasing rf power. The parallel ion flow speed is roughly twice as fast near the end of the source as at z = 126 cm, even though the measurements at z = 146 cm were obtained at a much larger neutral pressure. Also shown in Fig. 3-2a is the parallel ion temperature versus rf power at z = 126 cm for the 2.0 mTorr case. The parallel ion temperature is nearly constant at roughly 0.7 eV until the rf power exceeds 600 W. Above 600 W, the parallel ion temperature rises to nearly 1.0 eV at an rf power of 800 W.

The square root of the LIF signal amplitude as a function of rf power is shown in Fig. 3-2b. At both locations and at both pressures, the estimated plasma density (proportional to the square root of LIF signal assuming constant electron temperature) rises steadily with increasing rf power until a pressure dependent critical rf power is reached. In the 1.2 mTorr case, at location C, the plasma density stops increasing for rf powers greater than 600 Watts. Similar plateaus in measured plasma density have been observed in previous HELIX experiments [28]. At the higher neutral pressure, 1.7 mTorr, the plateau in estimated plasma density does not occur until the rf power reaches 800 W.

Note that in these measurements, the parallel ion flow speed at the upstream, z = 126 cm, location is much lower than the ion sound speed, $C_s \approx 4500$ m/s ($C_S = \sqrt{\gamma k T_e / m_i}$, where $\gamma = 1$ is assumed for isothermal expansion, k is Boltzmann's constant, and m_i is the ion mass), while at the end of the source the parallel ion flow speed increases slightly with rf power and remains roughly equal to the ion sound speed throughout the rf power scan. In laboratory plasmas with an open magnetic field geometry, it is typically assumed that the electrons stream out along the magnetic field and the ions are dragged out at the ion sound speed by the ambipolar electric field [29]. However, ionization of neutrals along axis of the system, radial transport, ion-electron recombination, and neutral drag (due to ion-neutral collisions including charge exchange) can all modify the ion flow along the magnetic field. In the case of a constant total ion flux along the axis of the system (arising perhaps from a plasma created upstream that then flows downstream without further ionization or recombination), as the surfaces of constant magnetic flux expand and the plasma density decreases, the parallel ion flow must increase to conserve the particle flux. These measurements clearly show an increase in parallel ion flow speed as the ions enter the region of weakening magnetic field at the end of the helicon source; a substantial increase in parallel flow speed even though the further downstream measurements were made at a higher neutral pressure. The slight increase in parallel ion flow speed with increasing rf power could simply be due to the decrease in ion drag due to collisions with neutrals at higher rf powers. The drag due to neutrals decreases at the higher rf power powers because the plasma density increases (Fig. 3-2b) while the neutral pressure was held fixed, i.e., the neutral density decreases with increasing rf power.

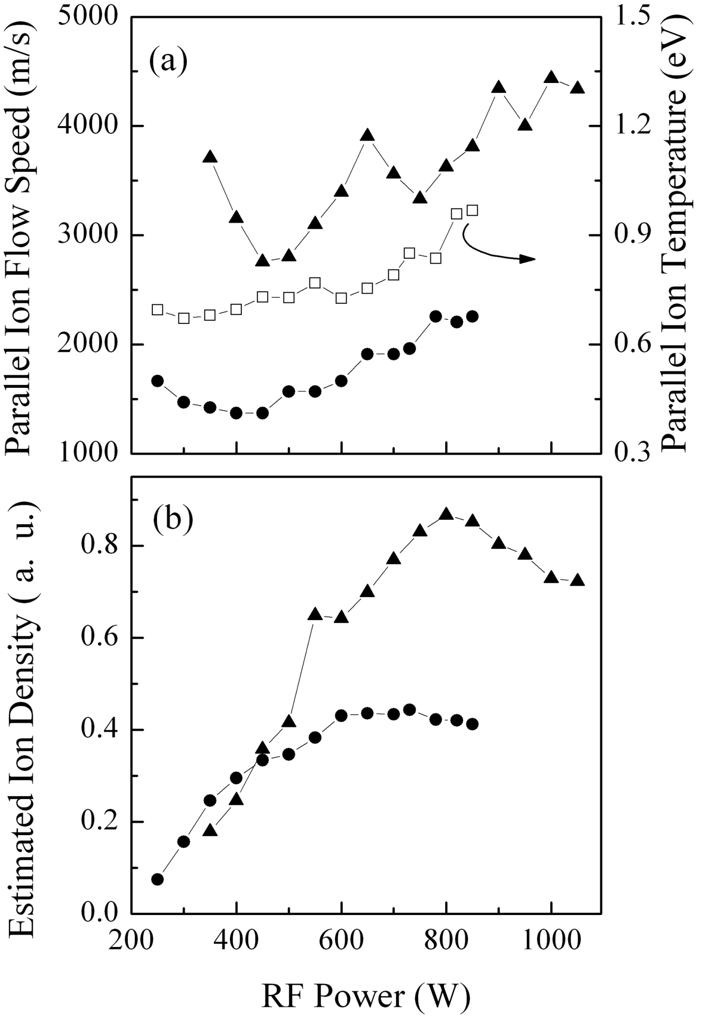

Figure 3-2. (a) Parallel ion flow speed in HELIX versus rf power for a neutral pressure of 1.2 mTorr at z = 126 cm (solid circles) and 1.7 mTorr at z = 146 cm (solid triangles). Also shown is the parallel ion temperature for a neutral pressure of 1.2 mTorr at z = 126 cm (open squares). (b) The ion density estimated from the LIF intensity versus rf power for a neutral pressure of 1.2 mTorr at z = 126 cm (solid circles) and 1.7 mTorr at z = 146 cm (solid triangles). For these measurements, B_H = 730 G, B_L = 34 G, and the rf driving frequency was 9.5 MHz

3.1.3 Effects of HELIX Magnetic Field Strength

As a function of HELIX magnetic field, the parallel ion flow speed for four locations and parallel ion temperature for three locations in HELIX are shown in Fig. 3-3a-b. The rf power was 750 W, the rf driving frequency was 9.5 MHz, and the neutral pressure in the source was 1.2 mTorr; except for the parallel ion flow speed measurements at the end of the helicon source (z = 146 cm) which were obtained at a neutral pressure of 1.5 mTorr. Clearly, there is axial gradient in parallel ion flow speed (Fig 3-3a) and in parallel ion temperature (Fig 3-3b) in the source. At all four locations, the parallel ion flow speed in the source is independent of magnetic field strength while the parallel ion temperature measured closest to the antenna, z = 80 cm, increases with source magnetic field strength. Further downstream, the parallel ion temperature is larger than at z = 80 cm, but the relative increase in parallel ion temperature with increasing source magnetic field strength is much smaller. Since both the parallel ion flow speed and parallel ion temperature increase with increasing distance from the antenna, it is likely that the observed ion heating results from thermalization of the ion flow, i.e., ion scattering converts a fraction of the flow energy into random motion.

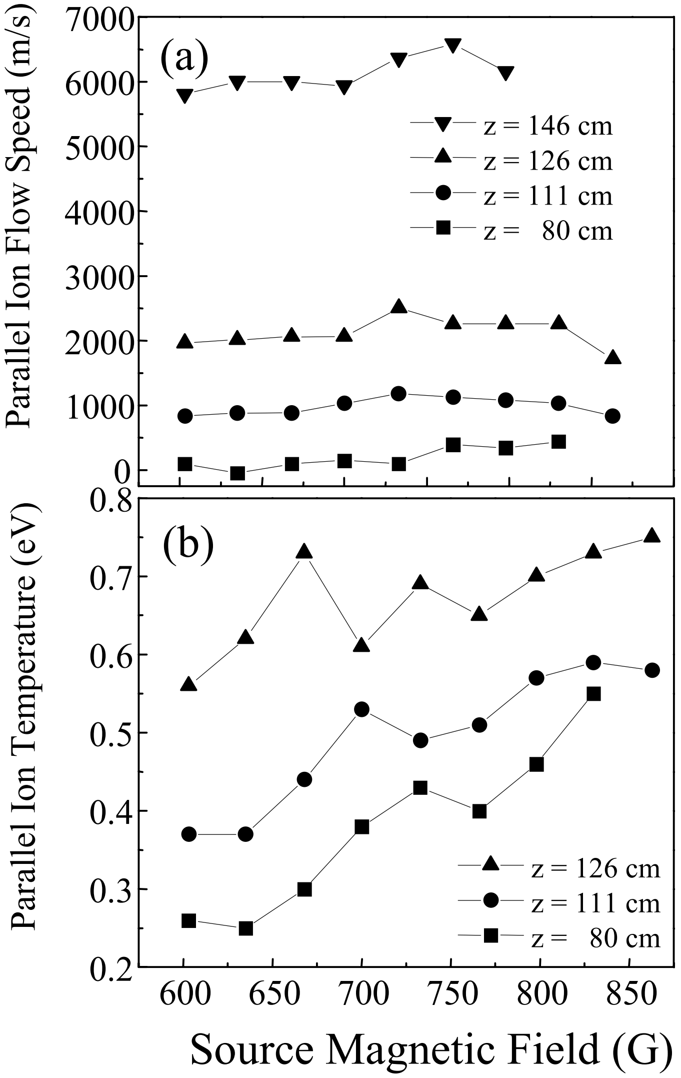

Figure 3-3. Parallel ion flow speed and parallel ion temperature measured at four locations in HELIX (a) and (b), respectively, versus HELIX magnetic field strength for B_L = 34 G, rf driving frequency of 9.5 MHz, rf power of 750 W, and a source neutral pressure of 1.2 mTorr; except for the z = 146 cm measurements in HELIX which were obtained at a neutral pressure of 1.5 mTorr.

3.1.4 Effects of LEIA Magnetic Field Strength

The parallel ion flow speed in HELIX, at z = 126 cm and z = 146 cm, and in LEIA, at z = 216 cm, are shown in Fig. 3-4 as a function of LEIA magnetic field strength. For these measurements, the rf power was 750 W, the rf driving frequency was 9.5 MHz, the source magnetic field strength was 730 G, and the neutral pressure in the source was 1.5 mTorr. Decreasing the LEIA magnetic field strength from 65 G to 10 G increases the parallel ion flow speed in HELIX at z = 146 cm from 5200 m/s to 7500 m/s, corresponding to an increase in ion energy of 5.3 eV to 11.1 eV.

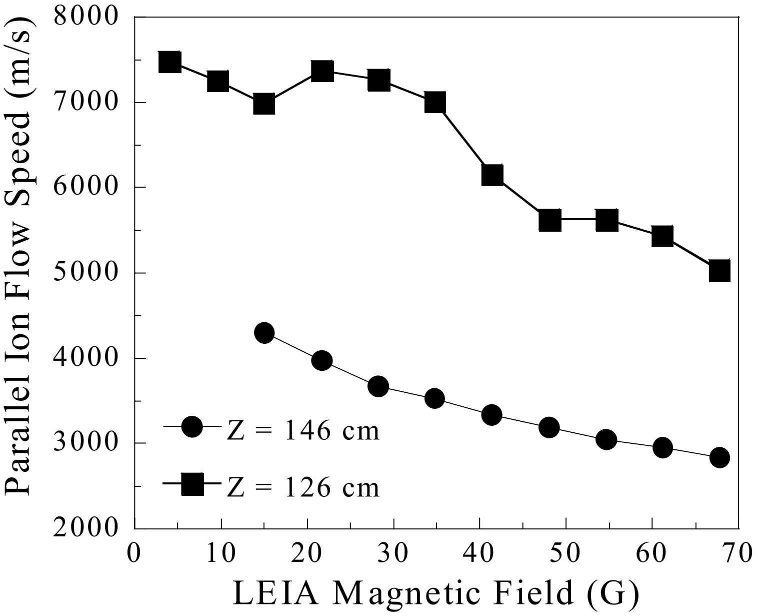

Figure 3-4. Parallel ion flow speed in HELIX, at z = 146 cm (solid squares) and z = 126 cm (solid triangles), and in LEIA, at z = 216 cm (open circles), for a HELIX magnetic field strength B_H = 730 G, rf driving frequency of 9.5 MHz, rf power of 750 W, and a source neutral pressure of 1.1 mTorr.

According to in-situ probe measurements made during the magnetic field strength scan from 65 G to 10 G, the HELIX plasma density at z = 126 cm decreased by 20% while the floating potential and electron temperature (and therefore the ion sound speed) in HELIX remained relatively constant. Thus, the parallel ion flow at the end of the source, z = 146 cm, is approximately equal to the ion sound speed at the smallest HELIX to LEIA magnetic field ratio (11.2) and increases to a little less than twice the sound speed at the largest value of the magnetic field ratio (73). Because the field expansion begins just inside the end of the helicon source (see Fig. 1-7), magnetic moment conservation, $\mu \equiv m\mathrm{v}_\perp{}^2 / 2B =$ constant, could play a role in accelerating the ions out of source. Magnetic moment conservation predicts conversion of 85% of the perpendicular energy to parallel energy for a factor of 6.5 increase in magnetic field ratio, B_H/B_L. In this scan, the parallel kinetic ion energy at z = 146 cm in the source increases from 5.3 eV to 11.1 eV, yet the parallel ion temperature is only 1 eV at the same location. For magnetic moment conservation to account for the observed ion acceleration, the perpendicular ion temperature at z = 146 cm (which we cannot measure), would have to be nearly 7 eV. Although we have observed significant ion temperature anisotropy in helicon sources [30], an anisotropy of 7 is many times larger than any we have observed in the source. Therefore, these parallel ion flow measurements suggest that the strength of the hypothesized double layer increases with decreasing downstream magnetic field strength. In other words, the worse downstream confinement makes the potential drop larger.

3.1.5 Effects of Neutral Pressure

By varying the number of active turbomolecular drag pumps, by operating the pumps at different rotation frequencies, and by adjusting the input gas flow rate, the neutral pressure in LEIA was varied without altering the neutral pressure in HELIX or other source parameters. Figure 3-5 shows that the estimated plasma density measured in HELIX at z = 126 cm (location C) increased by approximately 10% for a 6% increase in the LEIA neutral pressure (from 0.13 to 0.14 mTorr). The HELIX neutral pressure remained fixed at 1.2 mTorr while the LEIA pressure increased. Also shown in Fig. 3-5 is a roughly 10% decrease in parallel ion flow speed measured at location C in HELIX. Therefore, even a minor change in the downstream neutral pressure affects the parallel ion flow speed deep inside the helicon source.

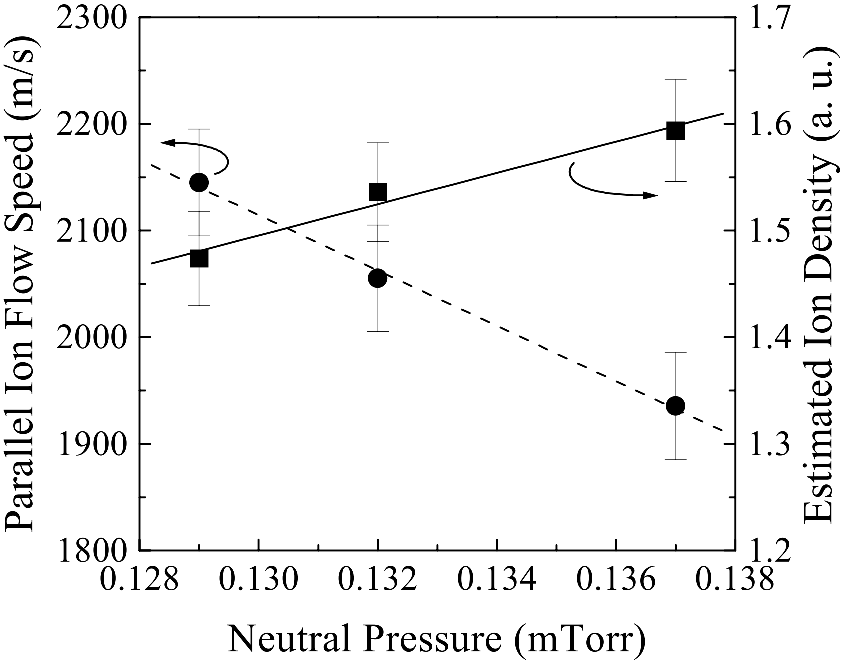

Figure 3-5. Parallel ion flow speed (solid circles) and the ion density estimated from the LIF intensity (solid squares) measured at location C in HELIX versus neutral pressure in LEIA for a fixed neutral HELIX pressure of 1.2 mTorr, $B_H = 730$ G, $B_L = 34$ G, rf driving frequency of 9.5 MHz, and rf power of 750 W.

The parallel ion flow speed and parallel ion temperature measured at four locations in the helicon source as a function of the neutral pressure in HELIX are shown in Fig. 3-6. The parallel ion flow at $z = 146$ cm normalized to the sound speed in the source shown in Fig. 3-6b. Well inside the helicon source, $z = 80$ cm, there is little parallel ion flow, $V_{i||} \leq 300$ m/s. Further downstream, $z = 111$ cm, the parallel ion flow is somewhat larger, $V_{i||} \approx 400$ m/s for neutral pressures greater than 1.2 mTorr. As the pressure drops below 1.2 mTorr, the parallel ion flow quickly increases to approximately 2000 m/s and then stays constant as the pressure is further reduced. Even further downstream, $z = 126$ cm, the parallel ion flow increases to nearly 4000 m/s at a neutral pressure of 1.1 mTorr. At 1.1 mTorr, the electron temperature in the source is roughly 10 eV, corresponding to an ion sound speed of 4900 m/s for argon ions. Thus, as can be seen in Fig. 3-6b, the parallel ion flow close to the end of the helicon source and well within the magnetic field expansion region, z = 146 cm, is close to twice the sound speed, $V_{i||} \approx$ 8000 m/s (1.7C_S) at 1.1 mTorr. Ion beams with velocities of roughly 2C_S downstream of the double layer were also observed by *Charles and Boswell* in their most recent experiments [22].

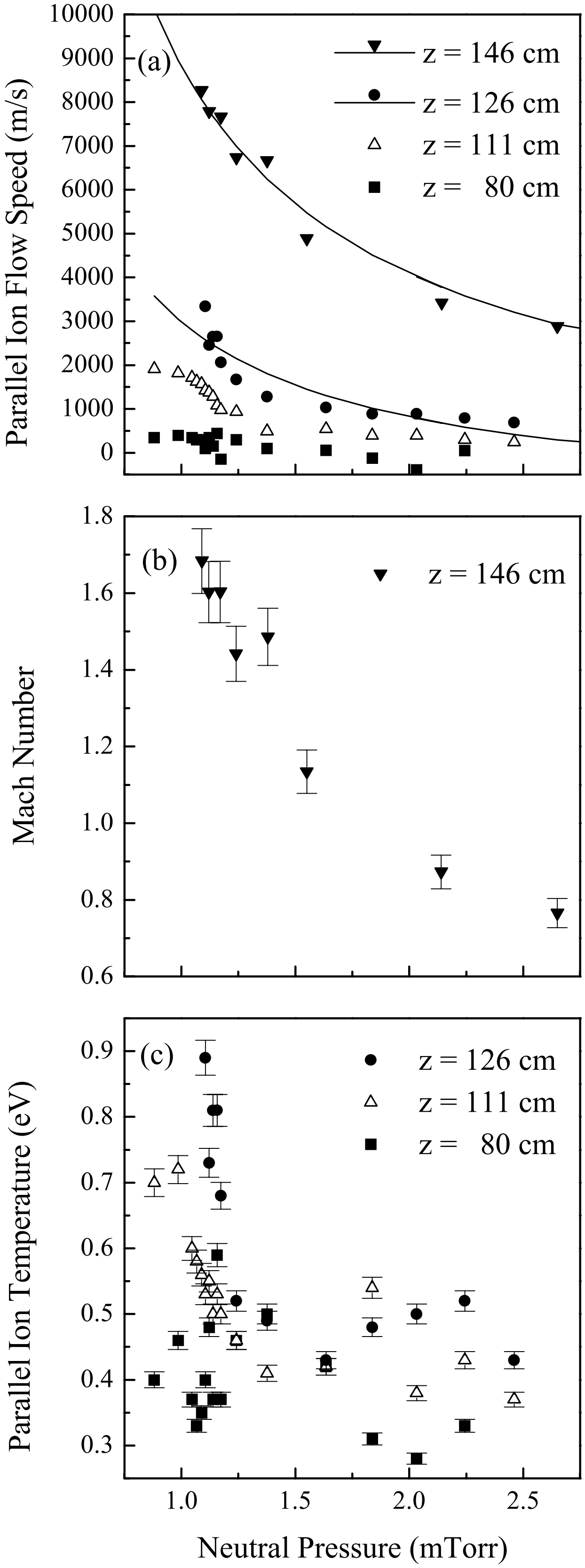

Figure 3-6. (a) Parallel ion flow speed, (b) Mach number, and (c) parallel ion temperature measured at different locations in HELIX versus source neutral pressure for B_H = 730 G, B_L = 34 G, rf driving frequency of 9.5 MHz, and rf power of 750 W. Solid lines are $v_{i||} = A/P_o + B$ fits to the measured parallel ion flow speeds

Consistent with the *Cohen et al.* [23] experiments, the rapidly flowing ion beam is one of two ion populations observed at end of the helicon source at neutral pressures below 1.6 mTorr (see Fig. 3-6a). Both ion populations drift along the system axis towards the LEIA chamber. At z = 146 cm and for neutral pressures greater than 1.6 mTorr, only a single ion population is observed. In the *Cohen et al.* [23] experiments, the two ion populations were found in the expansion region of the magnetic nozzle and downstream of a flux limiting aperture plate. Two ion populations, a "free" population and a "trapped" population are characteristic of electric double layers [31]. There is not a flux limiting aperture in these helicon experiments, nor is there a strong magnetic nozzle field. Thus, the formation of an ion beam, and by implication an electric double layer, inside the helicon source appears to be a general characteristic of these types of expanding, high-density plasmas. At the z = 126 cm location, there is also evidence of flow thermalization, probably by collisions, as the speed increases at low pressure (Fig. 3-6c). The parallel ion temperature increases 100% (from 0.5 to 1.0 eV) as the neutral pressure drops from 1.2 mTorr to 1 mTorr.

The parallel ion flow measurements shown in Fig. 3-6a indicate a complex dependence of parallel ion flow on neutral pressure. Well inside the source, the parallel ion flow is relatively independent of neutral pressure until the pressure drops below 1.2 mTorr. Below 1.2 mTorr, the upstream parallel ion flow speeds increase sharply and for the furthest upstream measurements, reach a plateau. However, the parallel ion flow speed at the end of the source appears to have a more simply defined dependence on neutral pressure. Note the lack of any threshold value of neutral pressure at which the parallel ion flow speed at z = 146 cm changes dramatically. Shown in Fig. 3-6a are fits to the two furthest downstream measurements. Each fit is of the form $\mathrm{v}_{i||} = \mathrm{A}/P_o + \mathrm{B}$ and while the fit to the z = 126 cm is poor, the fit to the z = 146 cm measurements is excellent. Assuming for the moment that z = 146 cm parallel ion flow measurements reflect a balance between acceleration in an axial electric field and some sort of drag process, the momentum balance equation

$$m\frac{d\mathrm{V}_{i\|}}{dt} = eE - \frac{m\mathrm{V}_{i\|}}{\tau}, \tag{3.2}$$

in steady state becomes

$$E\tau \propto \frac{1}{P_o}, \tag{3.3}$$

where τ is the collision time scale and the inverse scaling of parallel ion flow speed with neutral pressure has been assumed based on our experimental results. Assuming a typical form for the collisional time scale, $\tau \propto 1/n\sigma \mathrm{v}_{i\parallel}$, yields an electric field scaling of

$$E \propto \frac{1}{P_o}. \tag{3.4}$$

In other words, the dependence of the parallel ion flow at the end of the helicon source on neutral pressure suggests that the double layer strength, i.e., potential difference across the layer, increases with decreasing pressure. This result is in consistent with that the thickness of double layer is limited by the ion mean free path.

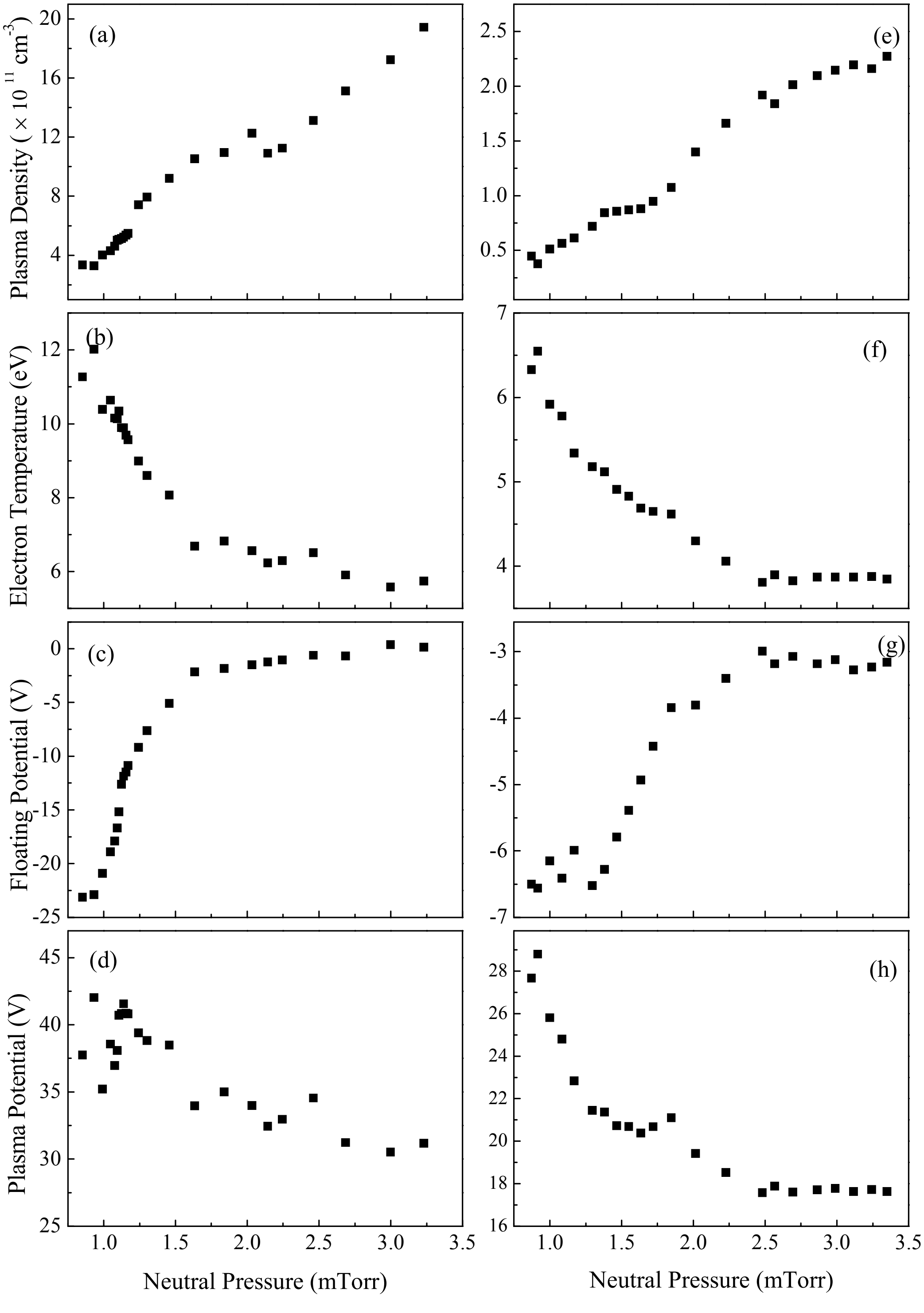

Figure 3-7. (a) Plasma density, (b) electron temperature, (c) floating potential, and (d) plasma potential according calculated from Eq. (2) at z = 126 cm in HELIX and (e) plasma density, (f) electron temperature, (g) floating potential, and (h) plasma potential measured at z = 188 cm in LEIA versus neutral pressure in the helicon source for B_H = 730 G, B_L = 34 G, rf driving frequency of 9.5 MHz, and rf power of 750 W.

The plasma density, electron temperature, floating potential, and plasma potential versus source neutral pressure measured at z = 126 cm in HELIX and z = 188 cm in LEIA are shown in Fig. 3-7. The floating potential measurements are referenced to the vacuum chamber which is held at ground potential. The increase in plasma density with increasing neutral pressure is roughly linear and the expansion chamber density is smaller than the source density by roughly one order of magnitude. In the plasma source, the electron temperature gradually increases from 5 eV to 6 eV as the neutral pressure drops below 2.5 mTorr and then sharply increases from 6 eV to 11 eV as the neutral pressure drops from 1.7 mTorr to 0.8 mTorr (Fig. 3-7b). The electron temperature in LEIA rises smoothly from 3.7 eV at a neutral pressure 2.5 mTorr to 6.5 eV at a neutral pressure of 0.8 mTorr (Fig. 3-7f).

Although the most dramatic parameter variation occurs in the floating potential in the source (Fig. 3-7c), the physically important potential is the plasma potential (Fig. 3-7d). Based on Eq. 2.7, the plasma potential in the source decreases from roughly 40 V at 0.8 mTorr to 35 V at 1.7 mTorr; identical plasma potentials to those reported by *Charles and Boswell* [22] at the same neutral pressures in their helicon source. At the highest pressure investigated, the plasma potential in the source drops to approximately 30 V. The plasma potential in our expansion region is positive and smaller in magnitude, by approximately 15 V, than in the source for a neutral pressure of 1.7 mTorr. The more positive source plasma potential is consistent with acceleration of the ions out of the source and into LEIA.

3.2 Parallel velocity and Ion Temperature Measurements in LEIA

3.2.1 The Parallel Velocity and Temperature of LEIA Ions

In LEIA, both the parallel ion flow speed (Fig. 3-8a, and 3-9) and parallel ion temperature (Fig. 3-8b) are almost independent of the HELIX and LEIA magnetic field strength. In Fig. 3-8a, and b, the parallel ion flow speed and parallel ion temperature are shown for three locations along the axis in LEIA as a function of source and LEIA magnetic field strength. In Fig. 3-10, LEIA flow measurements as a function of axial position are shown for locations from *z* = 290 cm to 188 cm, where *z* = 188 cm is 38 cm away from the end of the HELIX chamber (*z* = 150 cm). As can be seen in Fig. 3-10, the parallel flow speeds are largest closest to the plasma source.

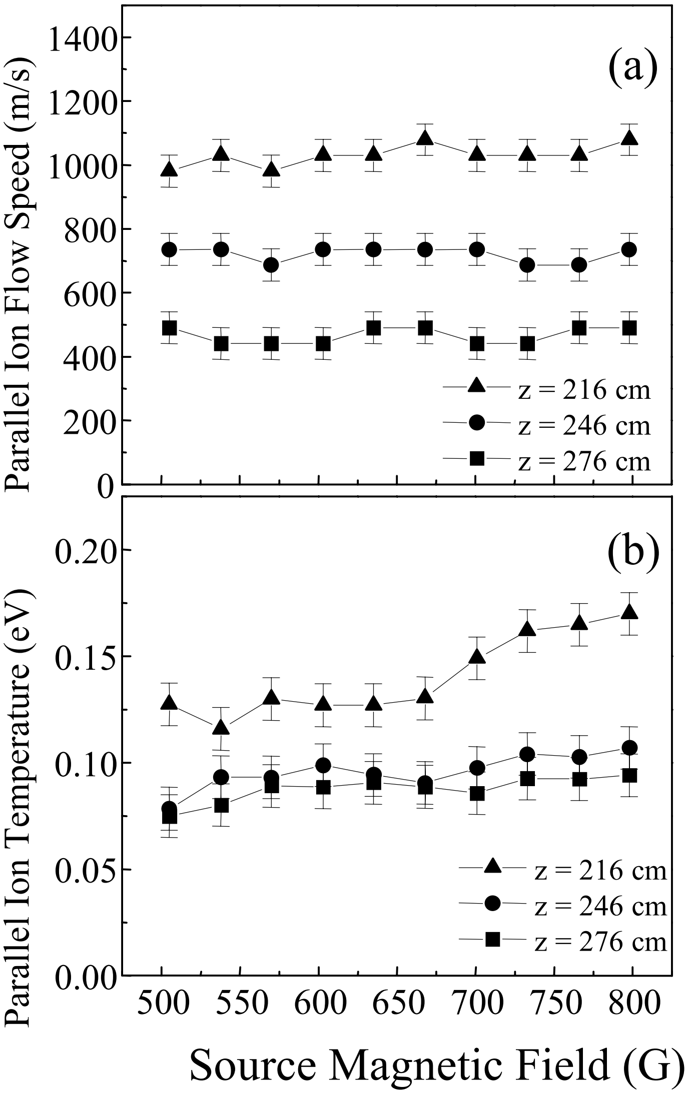

Figure 3-8. Parallel ion flow speed and parallel ion temperature measured at three locations in LEIA (a) and (b), respectively, versus HELIX magnetic field strength for B_L = 34 G, rf driving frequency of 9.5 MHz, rf power of 750 W, and a source neutral pressure of 1.2 mTorr

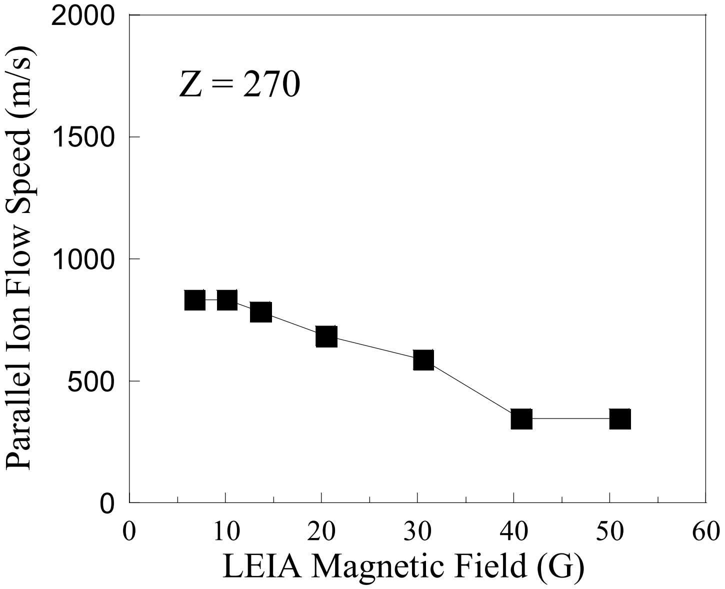

Figure 3-9. Parallel ion flow speed measured at z = 270 cm in LEIA, versus LEIA magnetic field strength for B_H = 730 G, rf driving frequency of 9.5 MHz, rf power of 750 W, and a source neutral pressure of 1.6 mTorr.

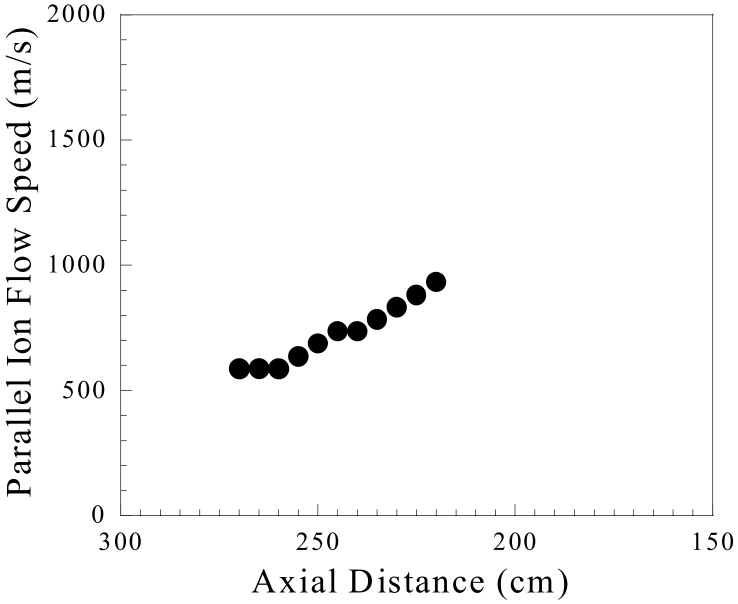

Figure 3-10. Parallel ion flow speed in LEIA versus axial position for B_H = 730 G, B_L = 34 G, rf driving frequency of 9.5 MHz, rf power of 750 W, and a source neutral pressure of 1.2 mTorr.

The flow speeds of LEIA ions are less than or equal to the thermal speed (1000m/s) and much less than the ion flow speed (8000m/s) measured near the end of HELIX. Collisions with background neutrals or scattering arising from flow driven instabilities will reduce the velocity of energetic ions. Because the parallel ion temperatures in LEIA are much colder, $T_{i||} \approx 0.1$ eV, than in HELIX, it is unlikely the ion flow is converted into random motion by ion scattering due to large amplitude waves, i.e., we would expect the ion temperature to increase as the parallel ion flow speed decreased. Collisions with background neutrals, whether charge exchange or elastic collisions, will slow down energetic ions. The total momentum transfer cross sections for Ar^+ - Ar collisions, including charge exchange and elastic collisions, at energies under 1 eV is relatively constant ($\langle \sigma \rangle \approx 1.3 \times 10^{-14}$ cm^2) [32] and yields an ion mean free path of λ_{mfp} = ($2.2/P_o$) cm, where P_o is the neutral pressure in mTorr and the neutral gas is assumed to be at room temperature. For a source pressure of 1.2 mTorr, at which the data shown in Fig. 3-10 were obtained, the expansion chamber neutral pressure is 0.16 mTorr – yielding an ion mean free path of approximately 15 cm. This value is likely an underestimate of the collisional mean free path in this system as recent LIF measurements of neutral argon have demonstrated that the neutral density profile in the helicon source is hollow [33]. The hollow neutral density profile, as well as an axial neutral pressure gradient, in helicon sources arises from a combination of neutral pumping [34] and the high ionization fraction typical of helicon sources. Over a distance of 35 cm, exponential decay of the parallel ion flow speed due to an ion mean free path of 15 cm would drop the parallel ion flow speed from 9000 m/s to roughly 900 m/s, consistent with the parallel ion flow speeds observed downstream of the helicon source. However, it cannot explain why the ion thermal energy decreases from 0.8 eV to 0.2 eV. If ion thermal energy were also transferred into neutral thermal energy during this process, then the ion temperature should be equal to the neutral temperature (0.02 eV). Thus, neutral drag processes can be excluded.

Although the HELIX plasma expands into the LEIA, the LEIA plasma may not simply be the remains of HELIX plasma. In the MNX experiment, *Cohen et al.* [23] argue that the ions in the expansion chamber were produced locally by ionization of neutral by energetic electrons from the source. A similar process could occur in HELIX. If so, the HELIX ions and LEIA ions can be produced locally in HELIX and LEIA, respectively. Then, a double layer or a sheath, if it appeared at the interface of HELIX and LEIA, would effectively separate the different HELIX and LEIA plasmas.

3.2.2 Observation of Two Ion Populations in LEIA

Given that the LIF intensity measurements inside the helicon source appear to suggest that the bulk of the metastable ions in the helicon source are excited directly from the ion ground state, it is possible that electron impact in the source is the major reason for creation of the metastable ions required for LIF [35]. When an electric double layer forms, there is usually a population of free ions and a population of trapped electrons upstream of the double layer. Indication of such an electric beam in Langmuir probe I-V measurements have been reported in the other expanding helicon source double layer experiments [23]. In such a situation, energetic ions in the appropriate metastable state passing through the double layer can be collisionally de-excited, i.e., the LIF signal for the ion beam will exponentially decrease with distance from the double layer. The quenching of the metastable ion states by collisions with neutrals, other ions, and even electrons, has been quantized in terms of a quenching cross section of $(5 \pm 1)\times 10^{-14}$ cm^{-2} in the *Cohen et al.* experiments [23]; a value that is roughly a factor of two larger than previous estimates [36]. The corresponding mean free path of 5.2 cm yields a decrease in LIF intensity of 99.9% over 35 cm in LEIA. Thus, it is difficult to observe the free ions in LEIA using LIF. Note however, that the quenching cross section reported in *Cohen et al.* experiments could be overestimated. Nonetheless, with the new angular motion probe port (see Chapter 2) pointing as close as possible to the end of HELIX, metastable ions in a supersonic beam emanating from HELIX have been observed in LEIA. By choosing optimal plasmas parameters, detection of the supersonic beam with the internal scanning probe (the superprobe) has also been accomplished.

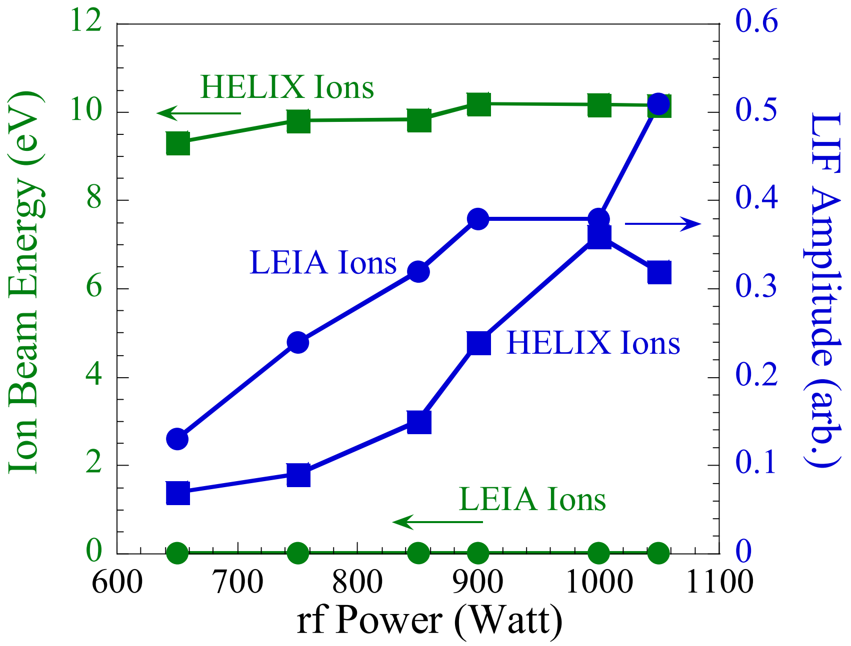

Figure 3-11. Parallel ion flow speed and LIF amplitude of supersonic ions (from HELIX) and background (LEIA) ions at z = 188 cm (in LEIA) versus rf power for B_H = 535 G, B_L = 34 G, rf driving frequency of 9.5 MHz, and a source neutral pressure of 1.5 mTorr.

As shown in Fig. 3-11, LIF signal amplitudes in both HELIX and LEIA increase with the rf power. Given that the depopulation of metastable ions is mainly due to the ion-neutral collisions, higher ionization at higher rf-power yields less neutrals and reduced depopulation of metastable ions and higher electron and ion densities and higher electron temperature. Thus, an increase in LIF amplitude in HELIX and LEIA with increasing rf-power is expected.

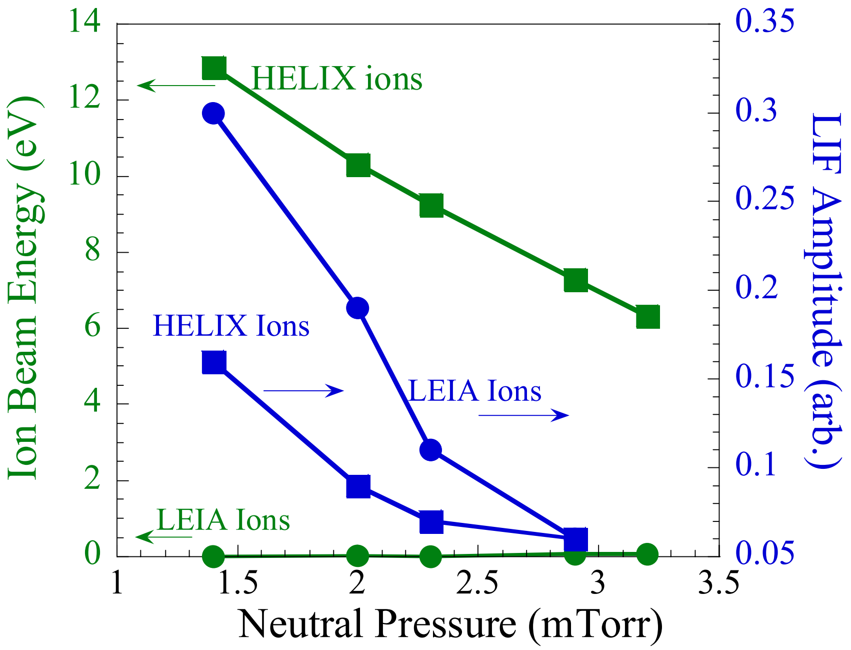

Figure 3-12. Parallel ion flow speed and LIF amplitude of supersonic ions (from HELIX) and background (LEIA) ions at z = 188 cm (in LEIA) versus neutral pressure for B_H = 530 G, B_L = 0 G, rf driving frequency of 9.5 MHz, and rf power of 900 Watts

Cohen et al. [23] reported that the LIF signal of trapped ions in the expansion region increases with increased neutral pressure in the expansion chamber and increased distance from the source. However, Fig. 3-12 shows that in HELIX-LEIA the LIF signal of trapped ions decreases with increasing neutral pressure. There is a key difference in the HELIX-LEIA and MNX experiments. In MNX, the source region is separated from the expansion region by an aperture plate with a 1-cm hole. In MNX the neutral pressure can be held nearly constant in the source while the neutral pressure in the expansion chamber is varied by closing the throttle valve in the expansion chamber. Thus, the flux of electrons (which produce the metastable ions probed by LIF) and ions into the expansion region from the MNX source remains constant for a wide range of neutral pressures in the expansion region. In contrast, HELIX-LEIA is a freely expanding plasma and increasing the pressure in HELX-LEIA increases the pressure in LEIA. Therefore, at the higher neutral pressures of Fig. 3-12 the flux of energetic electrons in the expansion region decreases. Therefore the LIF signal of the background ion population decreases with increases expansion region neutral pressure in the HELIX-LEIA system.

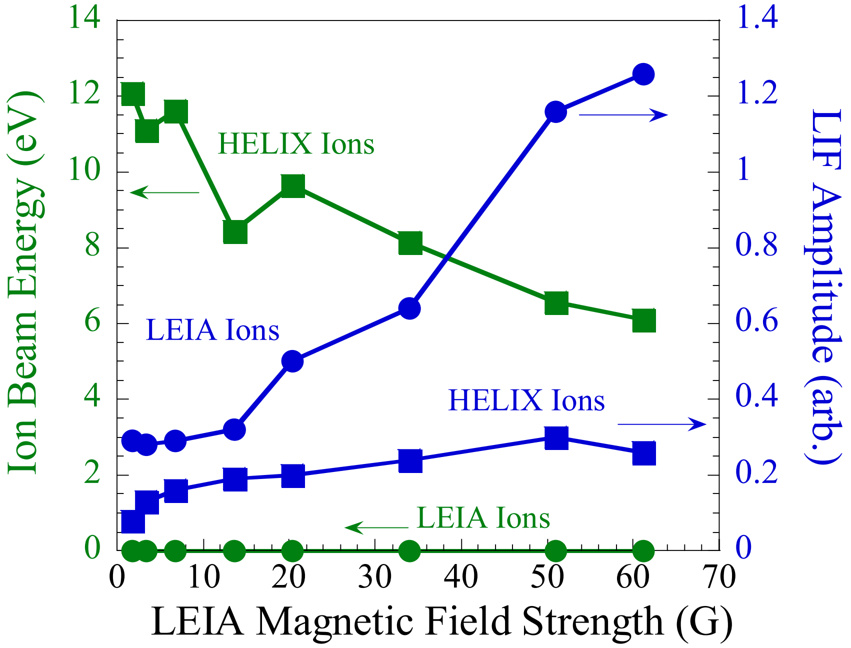

Figure 3-13. Parallel ion flow speed and LIF amplitude of supersonic ions (from HELIX) and background (LEIA) ions at z = 190 cm (in LEIA) versus B_L for B_H = 530 G, rf driving frequency of 9.5 MHz, rf power of 900 Watts, and source neutral pressure of 1.2 mTorr.

Because stronger LEIA magnetic fields improve the plasma confinement in LEIA, it is not surprising that the LIF signal from LEIA ions increases with increasing LEIA magnetic field strength (Fig. 3-13). The LIF amplitude of the fast ion population increases only slightly with the LEIA magnetic field strength (Fig. 3-13). At stronger HELIX magnetic fields, the LIF signal from the background ion population in LEIA increases and the LIF signal from the fast ion population decreases (Fig. 3-14). Since the plasma density increases significantly at larger source magnetic field strengths, these measurements suggest that the metastable quenching results from both ion-neutral and ion-ion collisions.

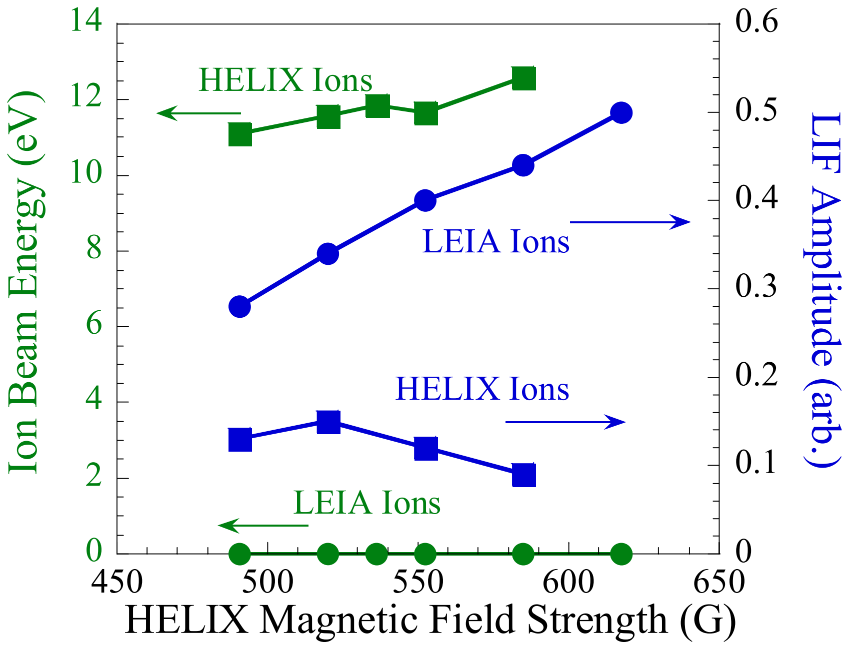

Figure 3-14. Parallel ion flow speed and LIF amplitude of supersonic ions (from HELIX) and background (LEIA) ions at z = 188 cm (in LEIA) versus B_H for B_L = 0 G, rf driving frequency of 9.5 MHz, rf power of 900 Watts, and source neutral pressure of 1.2 mTorr.

The key result of these investigations of the two ion populations in LEIA are that the parallel speed of the fast ions exiting HELIX increases with lower neutral pressure and LEIA magnetic field strength (as shown in Fig. 3-12 and Fig. 3-13) and is relatively independent of the HELIX magnetic field and rf power.

3.3 Observation of Double Layer at The Interface of HELIX-LEIA

Observations of a supersonic ion beam from HELIX and background ions flowing at roughly the ion thermal speed in LEIA are consistent with suggestions that divergent magnetic fields can play an important role in initiating DLs in a current-free expanding plasma [12]. That double layers can form in a current-free plasma expanding in a divergent magnetic field was predicted in an analytical study by Perkins in 1981 [37]. Although experimental observations of ion acceleration in expanding current-free plasmas soon followed [38, 39, 40, 41], no clear evidence of double layer formation was obtained in those experiments.

Current-free plasma expansion through a magnetic nozzle is surprisingly common and is found on a variety of spatial scales and in a variety of applications. The process of plasma expansion can be simply considered as the pressure gradient created by the change in the plasma density giving rise to a potential gradient which can be thought of as retarding the lighter plasma electrons but accelerating the more massive ions. The solar wind expansion is a classic example of this process [42]. Under isothermal, collisional conditions, the relationship between the density gradient and the potential drop agrees well with the simplified Boltzmann equation. However, in collisionless plasmas, the mean free path for ion collisions (such as elastic and charge exchange collisions) can be much longer than the scale length of the plasma expansion and/or the axial magnetic field. Under these conditions electric double-layers can arise.

A recent one-dimensional, unmagnetized, hybrid simulation (particle ions and fluid electrons) that modeled plasma expansion in a diverging magnetic field with a position dependent particle loss rate (see Fig. 3-15a for the experimental geometry and Fig.3-15b for the loss rate model) provided further evidence that a DL can form in a current-free plasma[43]. In that simulation, a clear DL formed at the location of rapid plasma expansion. Throughout the simulation volume, a low energy population of ions created by ionization and by charge-exchange collisions was observed. Downstream of the DL, a high energy ion population accelerated through the DL potential drop was observed. The roughly 14 eV potential drop across a DL with a width of a few tens of Debye lengths was obtained in the simulation for an argon plasma at a pressure of 0.5 mTorr; an electron density of 6.5 x 10^8 cm^{-3} and an electron temperature of 7.2 eV. The total ion acceleration occurred over roughly an ion mean free path.

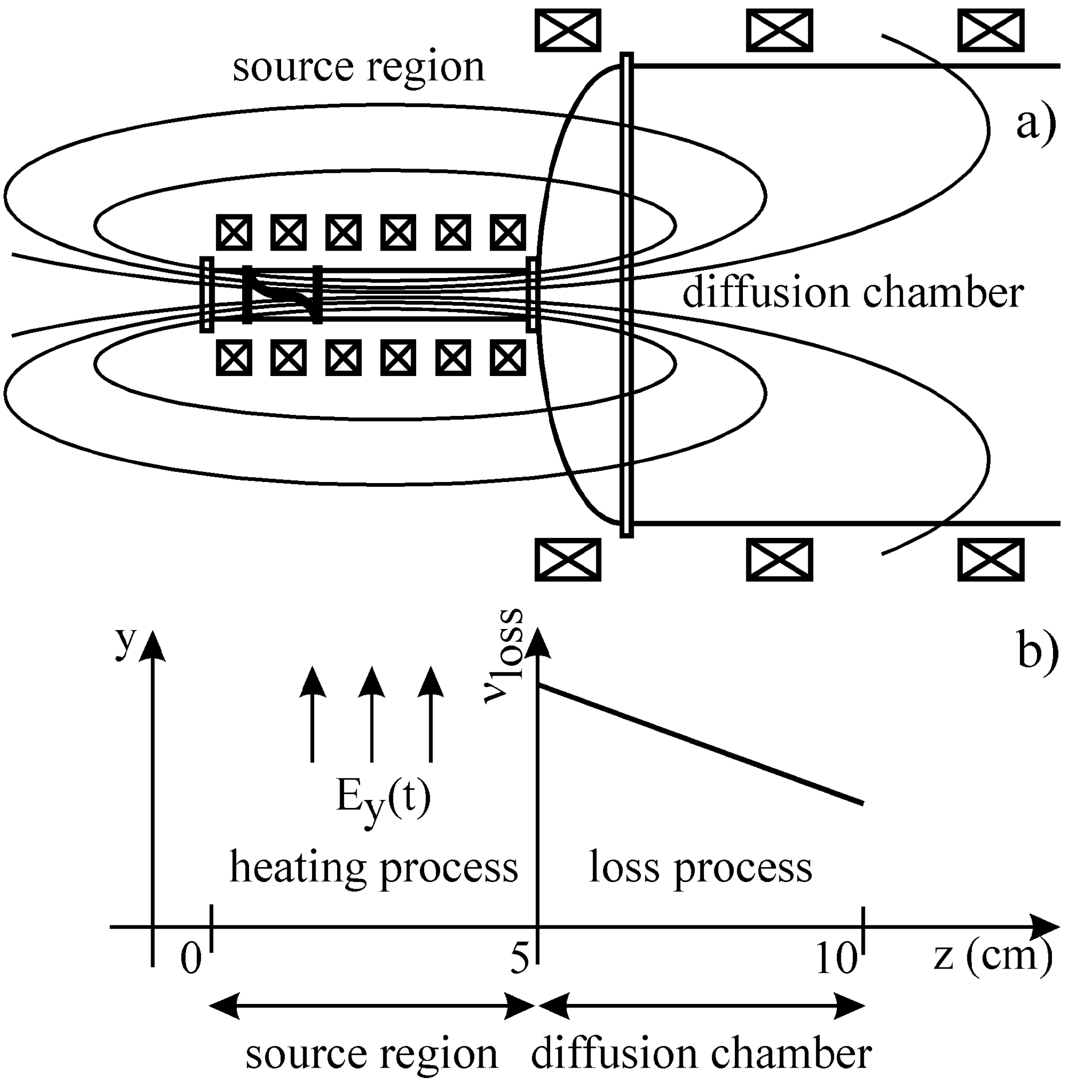

Figure 3-15. (a) Geometry of all three helicon source experiments referred to in this work with a range of magnetic field strengths (70 to 1000 G) and a larger diameter, coaxial, expansion chamber with (or without) additional magnetic field coils. Divergent region of magnetic field is near the junction of the two chambers. (b) Spatial dependence of electron heating and loss rate used in PIC model of plasma expansion.

To compare with the computer simulation, we plot the plasma potential profile and LIF measured parallel IVDF in the same 2D graph for a neutral pressure of 1.3 mTorr, shown in Figs. 3-16a and 3-16b. The end of the HELIX source is located at z = 150 cm, at nearly the same spot as the DL evident in the plasma potential and LIF data. The ions accelerate through the presheath upstream of the DL and reach a peak energy of approximately 18 eV. Each IVDF measurement used to create Fig. 3-16b has been corrected for the changing Zeeman shift as the ions move along the weakening axial magnetic field. Since the plasma electron temperature is 5.0 eV, the ion beam is supersonic with a Mach number of roughly 2.0. Consistent with the hybrid model and theory predictions [44], the ion acceleration occurs over roughly the ion mean-free-path. In HELIX, the ion mean-free-path [35] is roughly 15 cm and the LIF measurements indicate that the total ion acceleration occurs over approximately 20 cm (with strong ion acceleration occurring over a much narrower region located at the maximum of the magnetic field strength gradient). Consistent with the LIF-determined peak ion beam energy, the measured jump in the plasma potential across the DL in the plasma potential was 18 V (Fig. 3-16a). Also shown in Fig. 3-16a as solid triangles are the predicted plasma potentials upstream of the DL based on the measured gain in ion beam kinetic energy (the planar Langmuir probe could not access much of the region upstream of the DL). The solid line in Fig. 3-16a is the magnitude of the axial magnetic field strength. It is notable that the relative changes in the plasma potential, and therefore the ion beam energy, clearly track the axial magnetic field strength, i.e., the ion beam energy and magnetic field strength axial gradients are nearly identical. These LIF measurements confirm the hybrid model predictions of the location and general features (ion beam energy and trapped ion population distribution) of a magnetic field strength gradient induced DL in an expanding current free plasma.

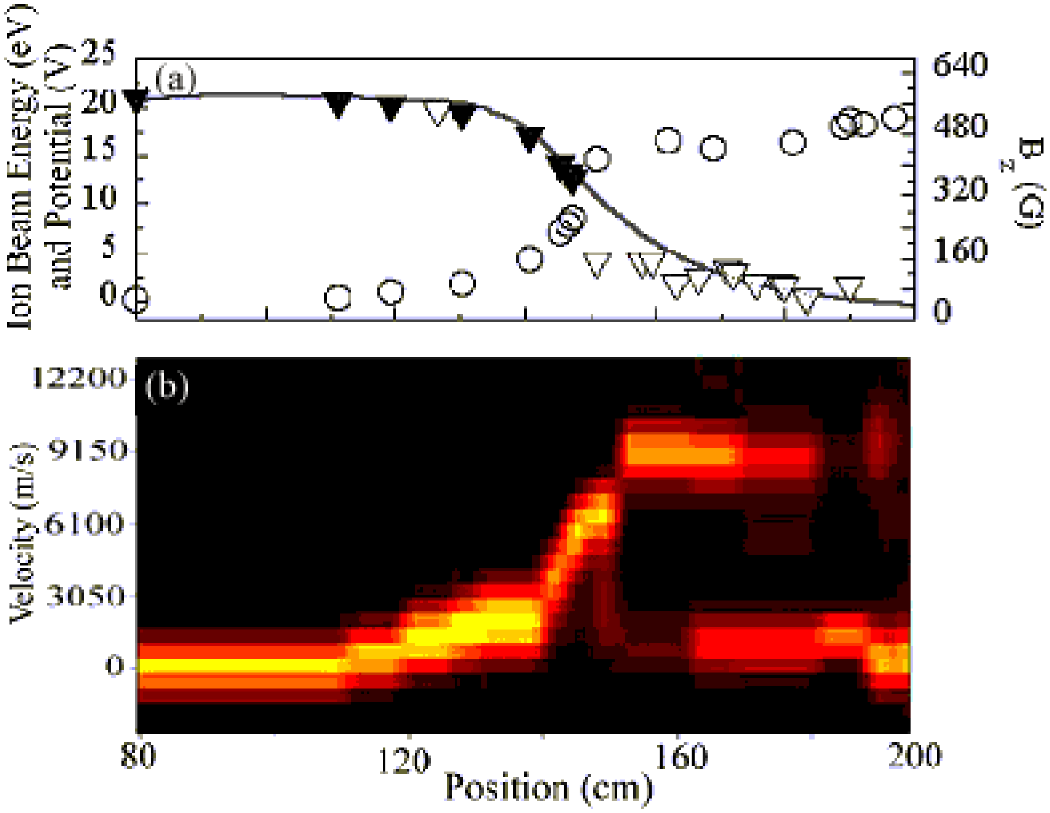

Figure 3-16. (a) Plasma potential versus axial position as measured with a rf-compensated, planar Langmuir probe (open triangle), ion beam energy as measured with LIF (open circles), predicted upstream plasma potential based on ion beam data (solid triangles), and axial magnetic field strength (solid line). (b) Natural logarithm of amplitude of parallel ion velocity distribution function (color bar) versus parallel velocity and axial position as measured by LIF. Measurements have been aligned by location of the end of the plasma source and beginning of rapidly expanding, divergent magnetic field.

Because the hybrid model used previously to examine DL formation due to rapid plasma expansion assumed a uniform Maxwell-Boltzmann distribution for the electrons, a one-dimensional Monte-Carlo Collision [45] Particle-in-Cell [46] (MCC-PIC) plasma computer code was developed to investigate electron transport through the DL and to confirm the current-free nature of the DL [47]. The PIC simulation consisted of a bounded plasma with a floating left wall and a grounded right wall. The system was separated into two regions: the source region and the diffusion chamber. In the source region, the electrons are heated up by a uniform RF electric field of 10 MHz perpendicular to the axis of the simulation. In the diffusion chamber, the expansion of the plasma in the diverging magnetic field is again modeled with a simple loss mechanism (Fig. 3-15b). Fig. 3-17a shows the density and potential profiles for the current-free DL obtained with a loss frequency slightly greater than the creation frequency (i.e. ionization frequency) for a neutral pressure of 1 mTorr and a plasma density of 7×10^{8} cm^{-3}. The potential drop across the DL is 12 V over a thickness of less than 20 Debye lengths and it is associated with a charging of the source (left wall) up to 10 V. The evolution of the DL as a function of the expansion rate (proportional to the magnetic field gradient) was studied for different pressures and we found that the expansion rate compared to the particle creation frequency (ionization frequency) was the critical parameter that determines the existence of the DL. We also found that the DL was completely current-free as long as the source is allowed to charge up and that the resultant electron energy distribution is uniformly Maxwellian and in Boltzmann equilibrium (explaining why the simpler hybrid model yielded similar DL structure). Another important result of the PIC simulation is that no electron beam is observed upstream of the DL in the simulation. One possibility under investigation is that instabilities generated in the DL region scatter electrons as they accelerate in the DL and prevent formation of an electron beam. What is clear, however, is that DLs arising from rapid plasma expansion appear to be distinctly different from those that are generally simulated or those believed to be responsible for electron acceleration in the aurora [48, 49].

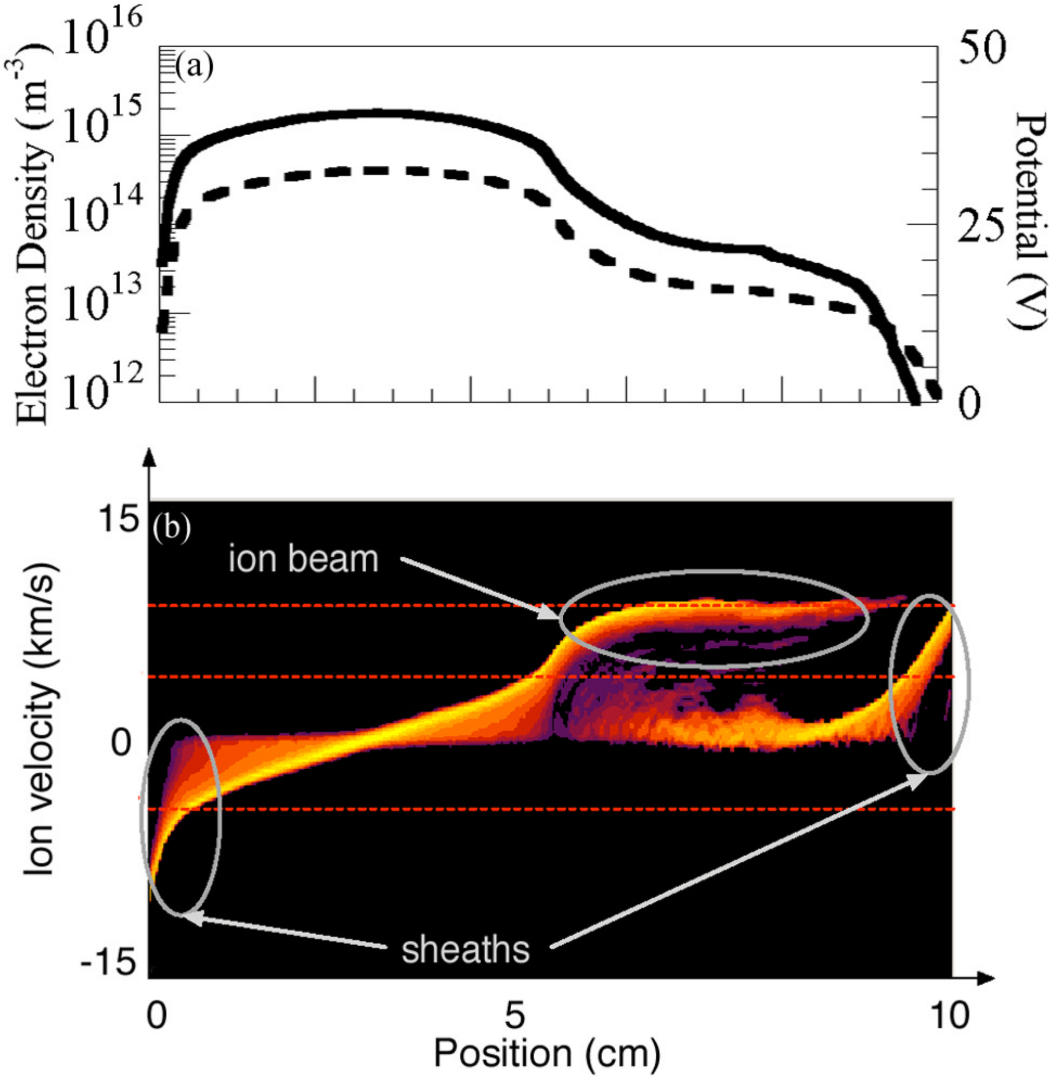

Figure 3-17. (a) Plasma density and potential along simulation axis obtained from MCC-PIC simulation. (b) Parallel ion velocity distribution function along MCC-PIC simulation axis

The magnitude of the IVDF in phase-space, as a function of position and ion velocity, predicted by the PIC code is shown in Fig. 3-17b. Throughout the simulation length, a low energy population of ions is observed which corresponds to the ions that are created by ionization and charge exchange collisions. Downstream of the DL a high-energy population can be seen which corresponds to the ions accelerated while traversing the potential drop of the DL. Note that the acceleration of the ions occurs over many centimeters in the simulation (in the pre-sheath and the sheath) while the actual DL is much narrower and appears in the ion phase-space plot as a narrow region of strong ion acceleration. The acceleration of the background ion population to the floating (left) and grounded (right) boundaries of the simulation volume as the ions fall through the sheath is also evident at the sides of Fig. 3-17b. The spatial structure, beam energy, character of the ion acceleration region, and ion heating in the pre-sheath in the simulation are all consistent with the LIF measurements shown in Fig. 3-16b. The plasma potential measurements (Fig. 3-16a) are also consistent in both magnitude and spatial structure as the predicted plasma potential axial profile (Fig. 3-17a). Therefore, the LIF measurements confirm the simulation predictions of DL formation in current-free, expanding plasmas.

In the HELIX experiments, the strength of the DL was about $3kT_e/e$, comparable to the DL formed in the free expansion Chi-Kung experiments and slightly weaker than the DL formed in the MNX experiments with a strong magnetic nozzle field. In all three helicon plasma experiments, the DLs appear in the expansion region for neutral pressures below some critical value. A recent experiment by *Plihon et al.* demonstrated DL formation in an axially uniform plasma with a uniform magnetic field by puffing SF_6 gas into the plasma at a single axial location [50]. The SF_6 gas, which is highly electronegative, induces a strong electron density gradient along the plasma axis by substantially reducing the electron density, thereby simulating rapid plasma expansion without a divergent magnetic field. If the ion-neutral mean-free-path is comparable to or larger than the scale length of the density gradient (equivalent to the scale length of the magnetic field gradient in HELIX and Chi-Kung), DL formation was observed.

In summary, the LIF measured DL potential structure and ion beam energies are consistent with the MCC-PIC computer simulation for a current-free, expanding helicon plasma. In the expansion region, the magnetic field gradient scale length ($B/\nabla B$), and therefore the probable density gradient scale length, is approximately 20 cm. In these experiments, the DL appeared at neutrals pressures such that the ion-neutral collision length was comparable to the gradient scale length.

3.4 Parallel Flow Shear and Temperature Anisotropy Measurements in HELIX

Observations of broadband electrostatic waves in the auroral region, when temperature anisotropy and parallel flow shear are present, suggested that parallel shear and temperature anisotropy could play a role in the excitation of low frequency electrostatic waves. *Ganguli et al.* [51] and *Gavrishchaka et al.* [52, 53,] demonstrated that parallel flow shear can reduce the threshold current for ion acoustic waves *Spangler et al.* [54] extended those results to include ion temperature anisotropy and demonstrated that thermal anisotropy can significantly modify the excitation threshold for ion acoustic waves. With the same theoretical model, *Scime et al.* [55] predicted that ion-cyclotron waves, including weakly damped multiple harmonics, can be excited in a completely current free plasma if the parallel flow shear and thermal anisotropy are sufficiently large. Q-machine-based laboratory investigations of shear modified ion acoustic waves [56, 57, 58] and [59], as well as shear modified ion cyclotron waves [60] demonstrated the important contributions of parallel shear to the excitation of these modes. In these experiments, we have investigated the possibility that shear modified ion acoustic or cyclotron waves can be excited in a current-free, helicon plasma. The first step in examining shear driven instabilities in our current-free helicon plasma is to measure the parallel velocity shear and temperature anisotropy. The parallel velocity shear in a helicon source occurs spontaneously and can be controlled through suitable choices of plasma source parameters.

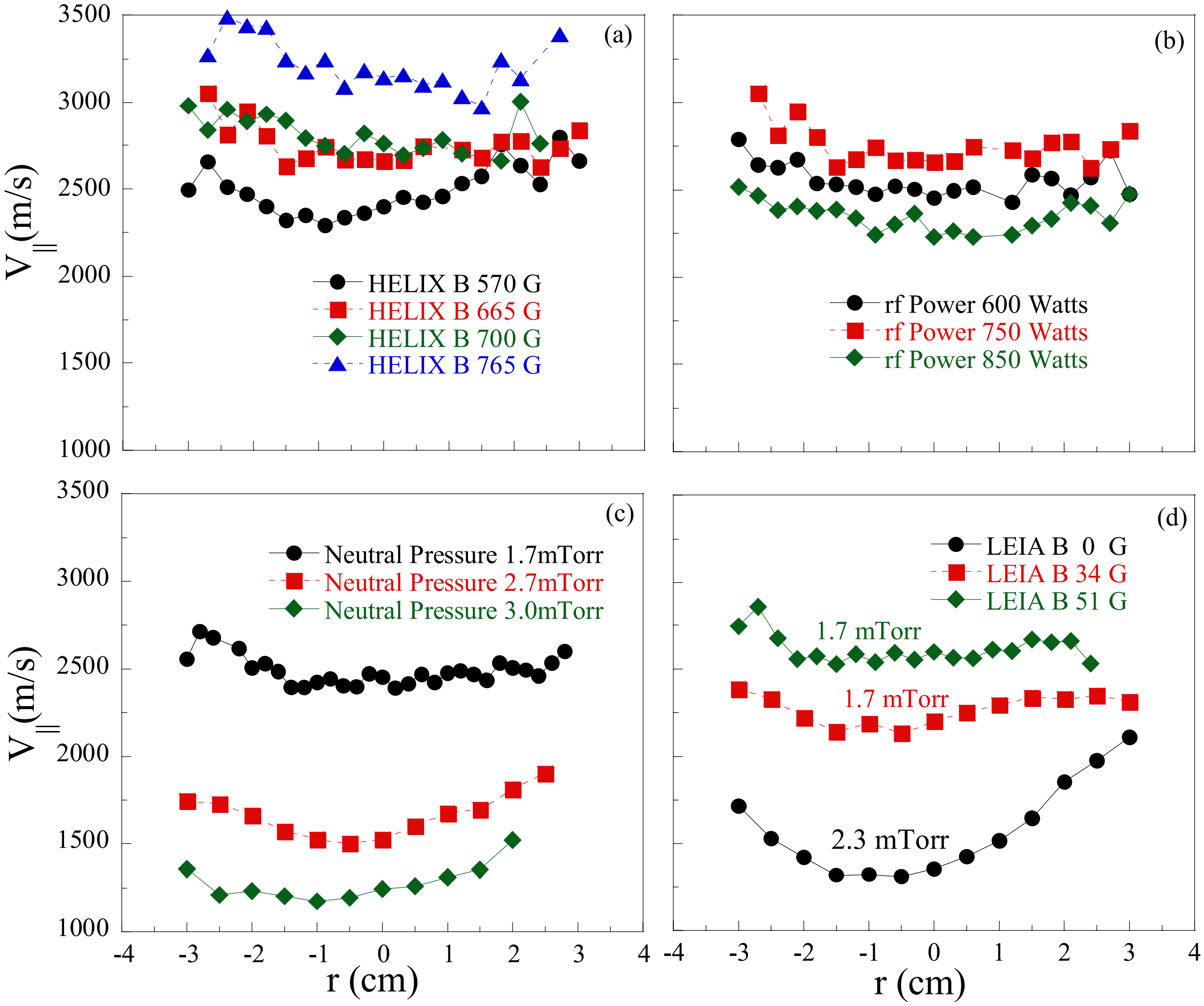

Figure 3-18. Parallel velocity shear measurements at location C (z = 126 cm) versus (a) B_H for rf power of 750 Watts, B_L = 34 Gauss, and source neutral pressure of 1.7 mTorr; (b) rf power for B_H = 663 G, B_L = 34 G, and source neutral pressure of 1.7-2.0 mTorr; (c) source neutral pressure for rf power of 750 Watts, B_H = 663 G B_L = 34 G; (d) B_L for rf power of 700-750 Watts, B_H = 580 Gauss, and source neutral pressure of 1.7 – 2.3 mTorr

Shown in Fig. 3-18 are the parallel velocity shear measurements at z = 126 cm for a HELIX magnetic field strength scan, rf power scan, neutral pressure scan, and LEIA magnetic field strength scan. Substantial parallel shear $[(dV_{||}/dx)(1/\Omega_{ci}) \sim 0.3\ ]$ in the plasma source is observed in a current-free plasma at low LEIA magnetic field strengths and low neutral pressures.

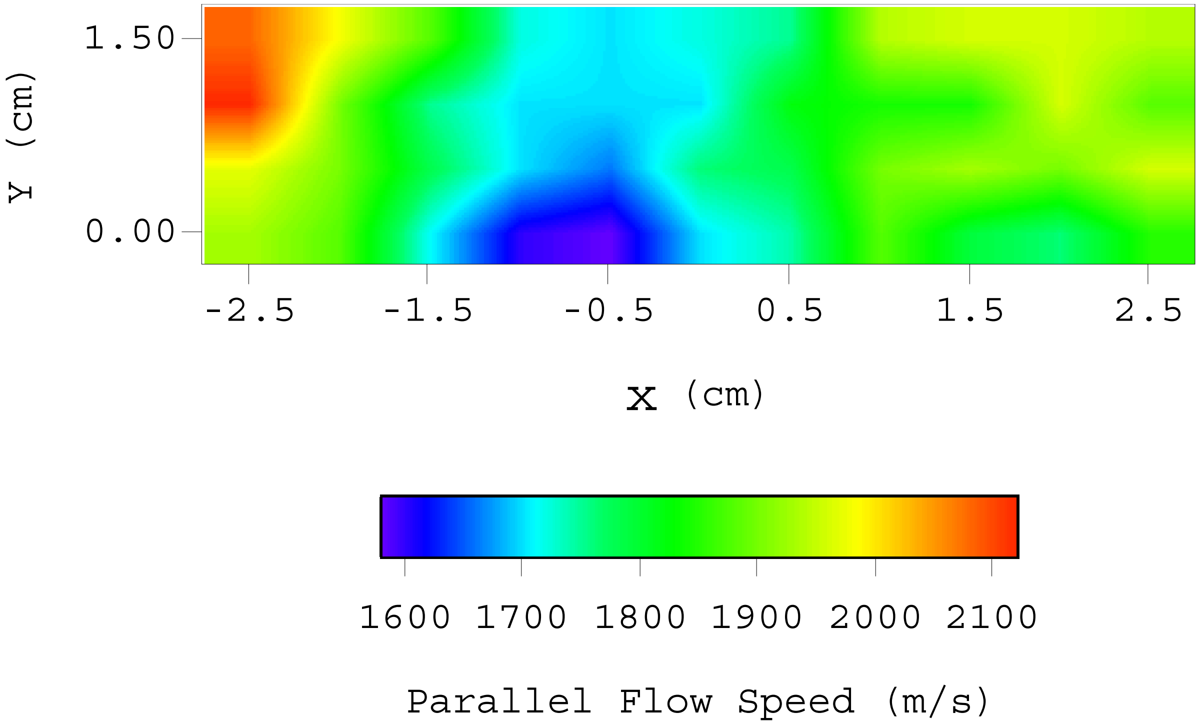

Figure 3-19. 2D parallel velocity shear measurements at location B (z = 111 cm) for rf power of 750 Watts, B_H = 730 G, B_L = 34 Gauss, and source neutral pressure of 1.5 mTorr.

Interestingly, the parallel flow shear appears at essentially the same parameters that lead to formation of the double layer [35]. The parallel velocity on axis increases significantly with decreasing neutral pressure and is faster at the edge at the larger neutral pressure values (Fig. 3-18d). The higher edge speeds are counter intuitive given that increase friction due to higher neutral pressures would be expected to lead to lower parallel ion speeds at the plasma edge. Previous investigations of DL formation in pulsed plasmas expanding into a vacuum found that double layers can have a complex two-dimensional structure [8]. If the surfaces of constant potential of the DL are convex pointing towards the LEIA chamber (i.e., normal relative to the surfaces of constant magnetic flux), a radial scan of field-aligned electric potential could yield measurements of higher field aligned potentials at the edge of the source compared to the center, i.e., faster ion speeds at the edge compared to the middle of the plasma. Closer to the rf antenna (z = 111 cm), 2D measurements of the parallel ion flow also show higher speeds at the plasma edge (Fig. 3-19). At *z* = 111 cm the parallel velocity is symmetric around *x* = -0.7 cm, very close the location of the legs of the rf antenna.

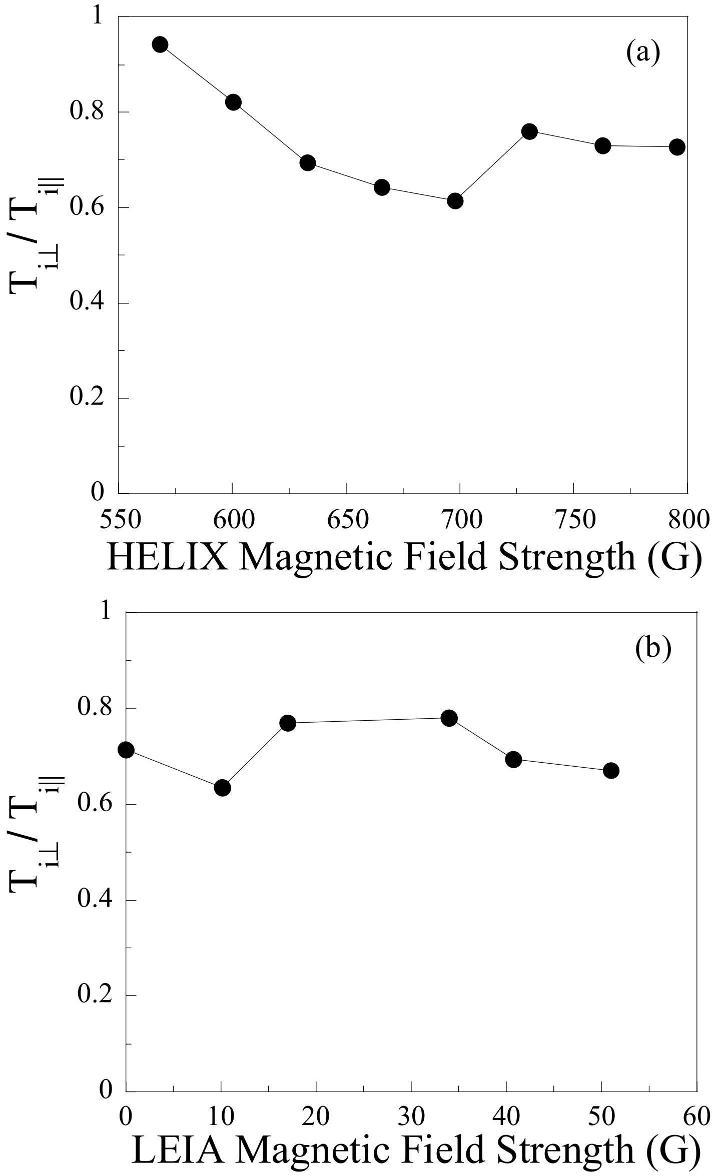

Figure 3-20. Parallel ion temperature anisotropy measurements at location C (z = 126 cm) versus (a) B_H for rf power of 750 Watts, B_H = 685 Gauss, and source neutral pressure of 1.7-2.0 mTorr; (b) B_L for rf power of 750 Watts, B_L = 34 Gauss, and source neutral pressure of 2.0 mTorr

Kline et al. [25] reported perpendicular ion temperatures larger than parallel ion temperatures at location B (z = 111 cm) over a range of HELIX magnetic field strengths, a rf power of 750 watts, and neutral pressure of 6.8 mTorr. However, at location C (z = 126 cm, where the magnetic field strength begins to decrease), the parallel ion temperature on axis exceeds the perpendicular ion temperature (Fig. 3-20). At this location, magnetic moment conservation effects are ignorable since the magnetic field strength has only decreased slightly (~2%) compared to the field strength in the source. In addition to the possibility of parallel ion heating due to thermalization of the parallel flow as suggested in Chapter 3.1.3, another possible explanation for the large parallel ion temperatures is locally created, slow, ions that co-exist with ions flowing towards the measurement location from upstream. If the parallel ion flow speed is small, so that these two ion groups overlap in LIF measurement, then the parallel ion temperature calculated from the linewidth of parallel ivdf will be anomalously large. In either case, the measured parallel ivdf is quite broad and represents a large effective parallel ion temperature. Since ion temperature anisotropy with $T_{i||} > T_{i\perp}$ suppresses the growth of shear modified ion acoustic and cyclotron waves in a homogeneous plasma, it appears that such waves can be ignored in terms of DL stability and nonlinear dynamics. Further study is warranted as the capability to create normalized parallel ion flow shears ($dV_{||} / \Omega_{ci} dx$) as large as 0.3 is significant.

Chapter 3 References

[1] R. Tanberg, Phys. Rev. **35**, 1080 (1930)

[2] E. Kobel, Phys. Rev. **36**, 1636 (1930)

[3] A. V. Gurevich, L. V. Pariiskaya, L. P. Pitaevskii, Sov. Phys. JETP. **22**, 449 (1966)

[4] V. G. Eselevich, and V. G. Fainshtein, Sov. Phys. JETP. **52**, 441 (1980)

[5] G. Samir, K. H. Wright, and N. H. Stone, Rev. Geophys. Space Phys. **21**, 1631 (1982)

[6] G. Hairapetian, and R. L. Stenzel, Phys. Rev. Lett. **61**, 1607 (1988)

[7] G. Hairapetian, and R. L. Stenzel, Phys. Rev. Lett. **65**, 175 (1990)

[8] G. Hairapetian and R. L. Stenzel R L, Phys. Fluids B **3**, 899 (1991)

[9] K. H. Wright, N. H. Stone, U. Samir, J. Plasma Phys. **33**, 71 (1985)

[10] P. Wagli, and T. P. Donaldson, Phys. Rev. Lett. **40**, 875 (1978)

[11] N. Singh, and R. W. Schunk, J. Geophys. Res. **88**, 7867 (1983)

[12] S. A. Andersen, V. O. Jensen, P. Nielsen, and N. D'Angelo, Phys. Fluids **12**, 557 (1969)

[13] P. Korn, T. C. Marshall, and S. P. Schlesinger, Phys. Fluids **13**, 517 (1970)

[14] H. Gunell, J. P. Verboncoeur, N. Brenning, and S. Torvén, Phys. Rev. Lett. **77**, 5059 (1996)

[15] T. Intrator, J. Menard, N. Hershkowitz, Phys. Fluids B **5**, 806 (1992)

[16] P. Coakley, and N. Hershkowitz, Phys. Fluids **22**, 1171 (1979)

[17] C. Charles, R. W. Boswell, R. K. Porteus, J. Vac. Sci. Technol. A **10**, 398 (1992)

[18] C. Charles, J. Vac. Sci. Technol. A **11**, 157 (1993)

[19] C. Charles, and R. W. Boswell, J. Vac. Sci. Technol. A **13**, 2067 (1995)

[20] F. F. Chen, X. Jiang, and J. D. Evans, J. Vac. Sci. Technol. A **18**, 2108 (2000)

[21] A. J. Perry, and R. W. Boswell, Appl. Phys. Lett. **55**, 148 (1989)

[22] C. Charles and R. W. Boswell, Appl. Phys. Lett. **82**, 1356 (2003)

[23] S. A. Cohen, N. S. Siefert, S. Stange, R. F. Boivin, E. E. Scime, and F. M. Leinton, Phys. Plasmas **10**, 2593 (2003)

[24] C. Charles and R. W. Boswell, Appl. Phys. Lett. **84**, 332 (2004)

[25] J. L. Kline, E. E. Scime, R. F. Boivin, A. M. Keesee, and X. Sun, Plasma Sources Sci. Technol. **11**, 413 (2002)

[26] J. L. Kline, E. E. Scime, R. F. Boivin, A. M. Keesee, and X. Sun, Phys. Rev. Lett. **88**, 195002 (2002)

[27] F. F. Chen, Plasma Phys. Contr. Fusion **33**, 339 (1991)

[28] P. A. Keiter, E. E. Scime, and M. M. Balkey, Phys. Plasmas **4**, 2741 (1997)

[29] M. Lieberman, and A. Lichtenberg A, Principles of Plasma Discharges and Materials Processing (John Wiley & Sons, New York, 1994)

[30] E. E. Scime, P. A. Keiter, M. W. Zintl, M. M. Balkey, J. L. Kline, and M. E. Koepke, Plasma Sources Sci. and Technol. **7**, 186 (1998)

[31] L. P. Block, Astrophys. Space Sci. **55**,59 (1978)

[32] A. V. Phelps, J. Phys. Chem. Ref. Data **20**, 557 (1991)

[33] A. M. Keesee, E. E. Scime, C. Biloiu, C. Compton, R. A. Hardin, X. Sun, and R. Boivin , Bull. Am. Phys. Soc. **48**, 211 (2003)

[34] J. Gilland, R. Breun, and N. Hershkowitz, Plasma Sources Sci. Technol. **7**, 416 (1998)

[35] X. Sun, C. Biloiu, R. Hardin, and E. Scime, Plasma Sources Sci. Technol. **13**, 359 (2004)

[36] F. Skiff F, G. Bachet, and F. Doveil, Phys. Plasmas **8**, 3139 (2001)

[37] F.W. Perkins and Y.C. Sun, Phys. Rev. Lett. **46**, 115 (1981).

[38] T. Nakano, N. Sadeghi, D.J. Trevor, R.A. Gottscho, and R.W. Boswell, J. Appl. Phys. **72**, 3384 (1992).

[39] D. J. Trevor, N. Sadeghi, T. Nakano, J. Derouard, R. A. Gottscho, P. Dow Foo, and J. M. Cook, Appl. Phys. Lett. **57**, 1188 (1990).

[40] N. Sadeghi, T. Nakano, D.J. Trevor, and R.A. Gottscho, J. Appl. Phys. **70**, 2552 (1991).

[41] C. Charles, R.W. Boswell, A. Bouchoule, C. Laure, and P. Ranson, J. Vac. Sci. Technol A **9**, 661 (1991).

[42] E.N. Parker, J. Geophys. Res. **62**, 509 (1957).

[43] A. Meige, et al., IEEE Trans. Plasma Sci. **33**, 334 (2005).

[44] L. R. Block, Astrophys. Space Sci. **55**,59 (1978)

[45] V. Vahedi and M. Surendra, Comp. Phys. Comm. **87**, 179 (1995).

[46] C.K. Birdsall and D. Fuss, J. Comp. Phys. **3**, 494 (1969).

[47] A. Meige et al., Phys. Plasmas **12**, 52317 (2005).

[48] C. K. Goertz and G. Joyce, Astrophys. Space Sci. **32**,165 (1975).

[49] D.L. Newman, et al., Phys. Rev. Lett. **87**, 255001 (2001).

[50] N. Plihon, C. S. Corr, and P. Chabert, Appl. Phys. Lett. **86**, 091501 (2005).

[51] G. Ganguli, S. Slinker, V. Gavrishchaka, and W. Scales, Phys. Plasmas **9**, 2321 (2002)

[52] V. V. Gavrishchaka, S. B. Ganguli, and G. Ganguli, Phys. Rev. Lett. **80**, 728 (1998)

[53] V. V. Gavrishchaka, G. I. Ganguli, W. A. Scales, S. P. Slinker, C. C. Chaston, J. P. McFadden, R. E. Ergun, and C. W. Carlson, Phys. Rev. Lett. **85**, 4285 (2000)

[54] R. S. Spangler, E. E. Scime, and G. Ganguli, Phys. Plasmas **9**, 2526 (2002)

[55] E. Scime, R. Murphy, E. Edlund, and G. Ganguli. Phys. Plasmas **10**, 4609 (2003)

[56] E. Agrimson, N. D'Angelo, and R. L. Merlino, Phys. Rev. Lett. **86**, 5282 (2001)

[57] S. Kim, E. Agrimson, M. J. Miller, N. D'Angelo, R. L. Merlino, and G. I. Ganguli, Phys. Plasmas **11**, 4501 (2004)

[58] E. P. Agrimson, N. D'Angelo, and R. L. Merlino, Phys. Lett. A **293**, 260 (2002)

[59] C. Teodorescu, E. W. Reynolds, and M. E. Koepke, Phys. Rev. Lett. **88**, 185003-1 (2002)

[60] C. Teodorescu, E. W. Reynolds, and M. E. Koepke, Phys. Rev. Lett. **89**, 105001-1 (2002)

Chapter 4: Double Layer Measurements in MNX

In Chapter 3, DL measurements in the HELIX-LEIA system, a configuration with purely divergent magnetic field, were reviewed. This chapter concerns measurements of the on-axis parallel ion flow speed in another helicon plasma source with a convergent nozzle magnetic field at one end and plasma limiting apertures placed a various locations in the source and expansion region.

4.1. Introduction to the MNX Experiment

The schematic of the Magnetic-Nozzle-eXperiment (MNX) facility is shown in Fig. 4-1. A 4-cm diameter, steady-state helicon plasma flows along the magnetic field formed by a Helmholtz-coil pair. The plasma exits the source (or main) chamber through a coaxial 2-cm-i.d., 3-cm-long nozzle coil used to control the magnetic field gradient. The nozzle coil extends from z =-1.5 cm to z = 1.5 cm. Fig. 4-1b shows the axial field strength near the nozzle at a Helmholtz coil current of 50 A and nozzle current of 400 A, typical of experimental conditions in this paper. Exiting the nozzle coil, the plasma enters a 10-cm-i.d., 100-cm-long Pyrex tube termed the expansion region (ER). By closing valves V2 and V1, the pressure in the expansion region can be increased independently of the pressure in the plasma source. The pressures are measured in the main chamber and expansion region by two capacitance manometers. The ER has 15 internal 4-cm-i.d. coaxial copper rings, of which eight may be electrically biased. The floating potentials of the copper rings in the ER were typically -40 to -120 V. Such large floating potentials suggest the presence of energetic electrons in the ER.

At low Helmholtz field strengths, MNX stably operates in the helicon mode over a wide range of main chamber pressures (from 0.4 to above 30 mTorr) AND at rf powers from 200 to over 2000 Watts. The helicon antenna was operated at 26.75 MHz. Negligible rf is detected in the expansion region because of efficient helicon absorption and because of the metal disk M2.

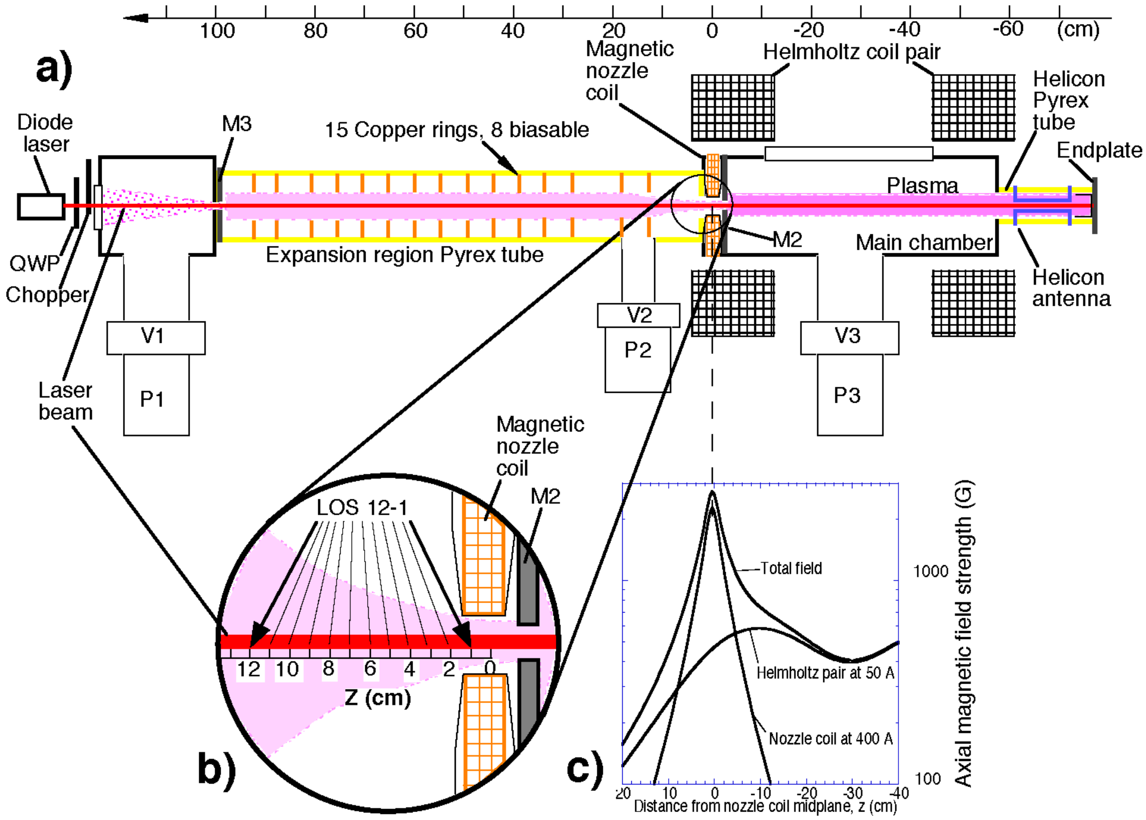

Figure 4-1. (a) The schematic of the Magnetic Nozzle experiment (MNX). Argon plasma is formed by absorption of helicon waves launched from a double-saddle antenna. The plasma flows through the main chamber along magnetic field lines created by a set of Helmholtz coils. The plasma then flows through metal aperture M2 and the nozzle coil into the expansion region (ER). The beam of a diode laser is directed along the MNX axis, allowing LIF measurements throughout MNX. (b) Scanning mechanism for the LIF collection optics allows 12 lines-of-sight (LOS) intercepting axial points in the ER near the nozzle. (c) The axial field strength near the nozzle at a Helmholtz coil current of 50 A and a nozzle current of 400 A, typical of experimental conditions.

Also shown in Fig. 4-1a are three electrically biasable metal disks, labeled *M1, M2*, and *endplate M3*. For the experiments reported here, the endplate and M1 were electrically floating. The disk M2, i.e., the aperture plate, has a hole, the aperture, which limits the plasma and neutral gas flows and helicon-wave propagation into the ER. Fig. 4-2 shows four locations where M2 may be positioned. Also, M2 may be completely removed, as shown in Fig. 4-2a. (The aperture diameters and plate thicknesses are indicated on the figure.) Sheaths of differing thickness will form on opposite sides of the aperture plate, predominantly because of the different plasma densities on the two sides of the plate. Based on Langmuir probe measurements at the center of the main chamber and in the expansion chamber 10 cm from the aperture, the ratio of the Debye lengths in the ER to that in the source chamber is ${}_{\mathrm{ER}}\lambda_D/{}_{\mathrm{s}}\lambda_D$ is ~10, with ${}_{\mathrm{s}}\lambda_D \sim 6 \times 10^{-4}$ cm. Control of pumping speed in the ER allows the ratio of ion-neutral collision lengths to be varied, $0.1 < {}_{\mathrm{ER}}\lambda_{\mathrm{in}}/{}_{\mathrm{s}}\lambda_{\mathrm{in}} < 10$, with $1 < {}_{\mathrm{s}}\lambda_{\mathrm{in}} < 10$ cm.

To permit measurement of the field-parallel $\mathrm{Ar}^{+}*$ velocity distribution in MNX, the elliptical-cross-section tunable diode-laser beam is directed along the MNX magnetic axis. Before entering the MNX vacuum chamber, the laser is sent through a quarter-wave plate, allowing creation of either right or left circularly polarized light for exciting either the σ- or σ+ transitions in Ar^{*+}. Optics to collect the fluorescence emission are located on both the main chamber and in the expansion chamber [typically 12 LOS, Fig. 4-1b]. One main-chamber LOS (LOS-P) collects photons from a segment of the plasma in the center of the chamber; the other, LOS-N, collects photons from the plasma near M2 and extending 1.2 cm back into the main chamber. Scanning optics on the ER allow LOS which intercept the laser beam from 1-cm from the nozzle-coil midplane to 12 cm from its midplane, as well as beyond, see *z*-axis in Fig. 4-1b. A detailed description of LIF measurement principles can be found in Ref. [1,2].

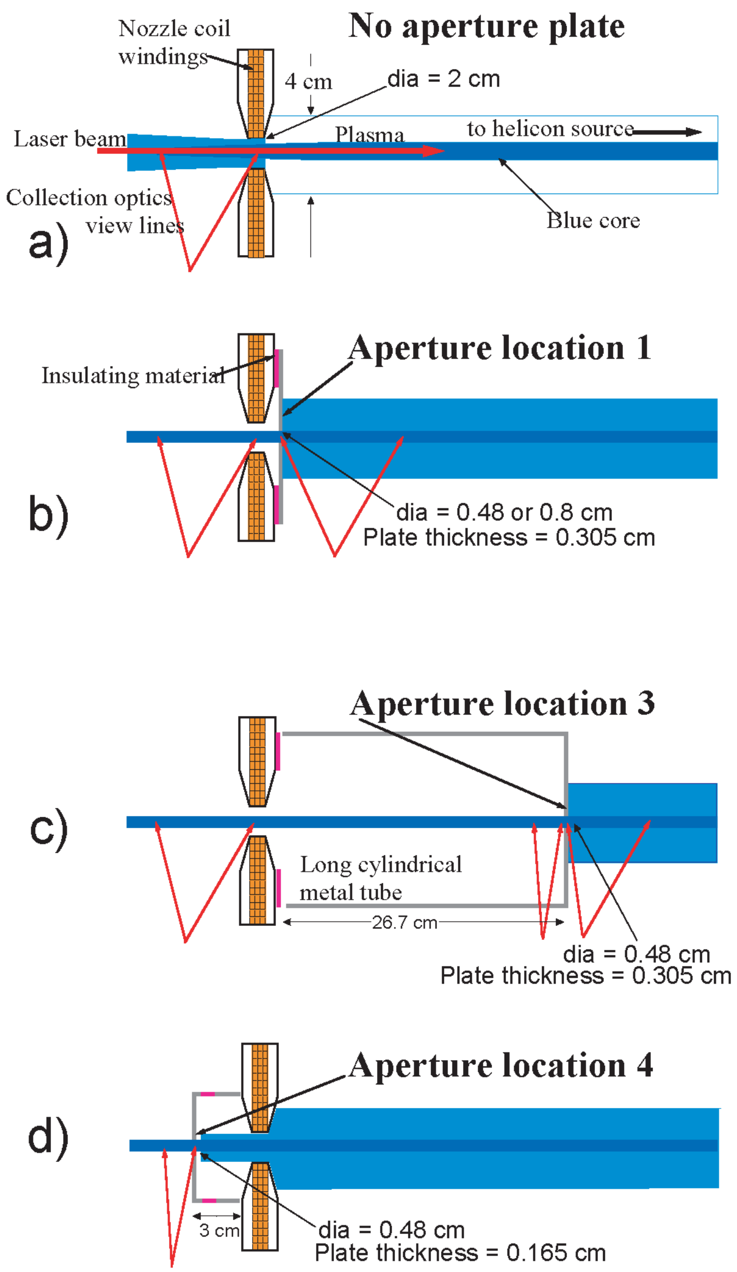

Figure 4-2. Four different configurations were taken in the experiments: (a) without aperture plate, the measurements were performed in the ER; (b) a metal disk with an aperture of 0.48 cm and thickness of 0.305 cm was placed immediately before the nozzle. The measurements were performed in both the ER and source. (the work done with 0.8-cm-aperture are no presented here); (c) the disk used in (b) was moved into the source, measurements were performed near the aperture plate and in the ER; (d) a metal disk with an aperture of 0.48 cm and thickness of 0.165 cm was placed in the ER. The measurements were performed near the aperture plate.

4.2. Experimental Results and Discussion

Some features common to the earlier mentioned helicon and non-helicon DL-producing experiments are apertures – mechanical or magnetic – and low neutral-gas pressures. Neutral-gas pressure affects both plasma diagnostics (especially Ar^{+*} LIF) and plasma parameters such as collisionality, hence the ivdf, the ionization source, and the pre-sheath length. The effects of apertures on DL formation are not as well understood and the objective of these MNX experiments was to investigate the effect of apertures on DL formation and the corresponding IVDFs.

In terms of the physics of double layers, what is an aperture? An aperture (in a plate) is a hole of radius, r_a, smaller than the plasma column's radius, r_p, which divides the plasma column into source and expansion regions (see Fig. 4-1). Apertures reduce neutral-gas flow between the plasma source and the plasma expansion regions and also separate the region of energy input *via* the helicon wave, the main (or source) chamber, from the expansion region, where the energy input is in the form of particle enthalpy. Apertures may alter the ratio of ion to electron fluxes from the source region into the ER, in part due to differing gyro-radii. (In the final analysis, the electric field, Poisson's equation, controls particle fluxes.) The large gyroradii of ions (ρ_i ~ 0.1 to 1 cm) compared to electrons ($\rho_e \sim 4 \times 10^{-3}$ to 4×10^{-2} cm) in our experiment will also change the radial distribution of ions and electrons on the downstream side of the DL. Mechanical aperture plates establish an equipotential boundary in a plane around the aperture hole. In the experiments described here, the short sheath thickness, ${}_s\lambda_D < 10^{-3}$ cm, in the source chamber results in a strong electric field at the aperture plate, $> 10^4$ V/cm. Because ${}_s\lambda_D / r_a \ll 1$, only the presheath with length ~ 3 cm (larger than the aperture diameter) can extend across the aperture [3] and modify the local potential seen by plasma transiting the aperture, see Fig. 4-3.

The hypothetical equipotential lines curving into the aperture shown in Fig. 4-3 are consistent with the experimental observation that there is a large potential drop (6-8 kT_e/e) across the aperture (as will be shown by LIF measurements near the aperture). The observed ion acceleration through the aperture indicates an imbalance of charge across the aperture with excess positive charge upstream and excess negative charge downstream. At the edge of the aperture, the equipotential lines should be parallel to the plate surface, i.e. the electric field must be conducting perpendicular to the surface. Note Fig. 4-3 cannot completely describe the real equipotential surfaces in the experiment. For instance, the chamber walls have been ignored. Thus, the real equipotential surfaces are more complicated. However, the basic structure shown in Fig. 4-3 should be representative of the actual equipotential surfaces.

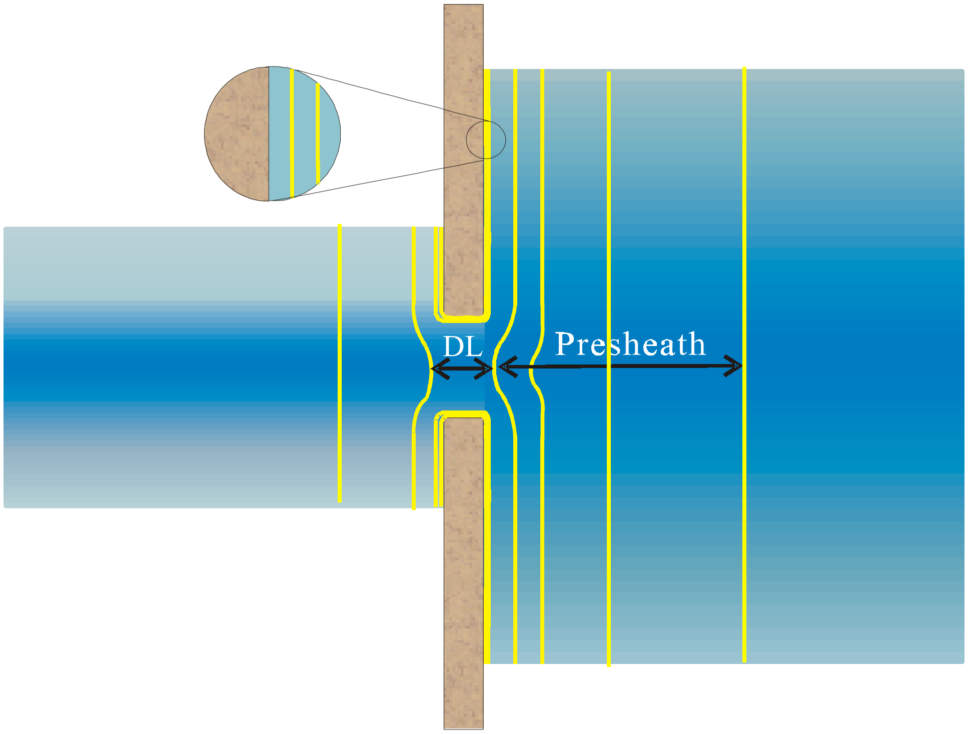

Figure 4-3. Hypothetical equipotential surfaces around and inside the aperture for the plasma conditions of the MNX experiments.

There are also other questions concerning the role of apertures in a plasma. For example, will the presheath electric field be affected if an aperture is created in an absorbing wall? *Riemann* argued that the length of presheath should be equal to the ion-neutral collision length in his model of plasma sheaths [4]. *Oksuz* and *Hershkowitz* verified *Riemann*'s presheath model experimentally on a surface immersed in a low density, low temperature, weakly collisional, argon plasma [5,6]. They found that the potential drop across the presheath is ~ kT_e/e, instead of $kT_e/2e$ as determined in the *Riemann* sheath model. The experimental data that will be presented in this work are consistent with a potential drop of ~ kT_e/e in front of an aperture in a metal plate, thereby corroborating the *Oksuz* and *Hershkowitz* experiments. We also have installed two apertures, separated by up to $10^5\ \lambda_D$, to explore whether the strongly modified (upstream) IVDF and EEDF will promote formation of a second DL at the second aperture.

A magnetic aperture is a region of converging/diverging magnetic field, commonly called a magnetic Laval nozzle. The basic idea is to compress the plasma by shrinking the cross section of magnetic flux tubes and then, as the plasma enters the expanding section of the nozzle magnetic field, supersonic ion speeds are achieved by converting the thermal (random) energy into directed (flow) energy. Magnetic Laval nozzles were used to create a supersonic ion beam in a plasma in 1969. Mach numbers as large as 3 were obtained in a Q-machine [7]. More recently, a magnetic nozzle was proposed for the VASIMR rocket to convert thermal energy into thrust [8, 9]. Note that, in the measurements reported here and in previous MNX studies, the ion beam energy decreased with increasing nozzle field strength. Therefore, the ion acceleration to supersonic speeds is not simply understood by the analogy to the mechanical Laval nozzle. Efforts must be made to understand the static electric field, i.e., the DL, which creates the energetic ion beam.

A. The magnetic nozzle as an aperture

Without an aperture plate, Fig. 4-2a, the plasma flows into the expansion region from the main chamber through the 2-cm-i.d. of the magnetic-nozzle coil. The midplane of the nozzle coil is defined as $z = 0$ cm. Figure 4-4 shows the beam energy at $z = -3.0$ cm in the ER versus the nozzle-magnetic-field strength for an rf-power of 800 Watts, magnetic field (B_H) of 580 Gauss at the center of the source chamber, and neutral pressures of 0.7 mTorr and 0.2 mTorr in source (P_M) chamber and ER (P_{ER}), respectively. The energy of the exiting ion beam decreases with increasing nozzle field strength until the (added) nozzle field strength reaches 2000 Gauss. (At $B_n = 2000$ G, the ratio, R, between the on-axis magnetic field at the nozzle midplane to that in the center of the ER was $R = 4.75$. At $R = 4$, a 4-cm-dia plasma column will pass through the nozzle without contacting the nozzle coil housing.) The ion beam energy at $z = -3.0$ cm is approximately

7 eV for B_N = 2000 G. The corresponding Mach number (V/C_s) was ~ 1.3. For nozzle magnetic field strengths below 1000 Gauss, the LIF signal was too weak to give a good measure of ion speed.

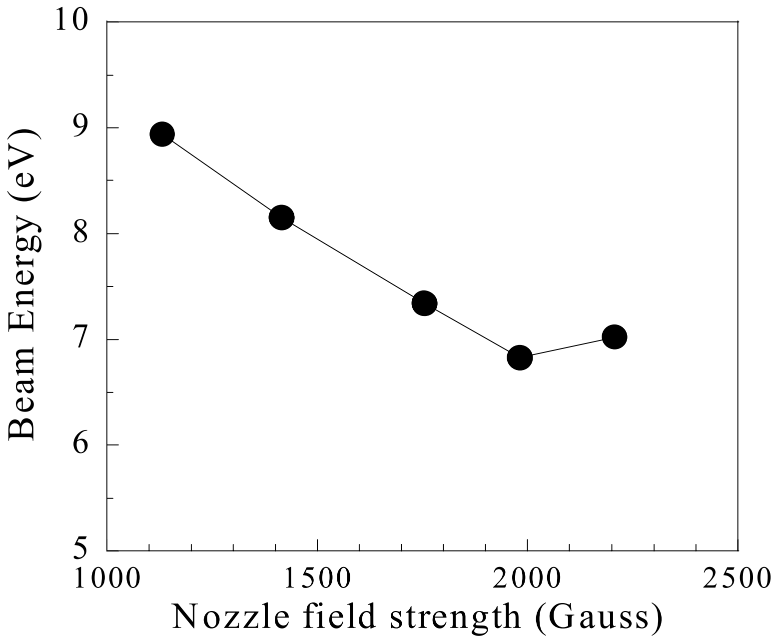

Figure 4-4. The beam energy versus the nozzle field strength at z = 3.0 cm for RF power of 800 W, B_H = 580 G, P_M = 0.7 mTorr, P_{ER} = 0.2 mTorr, and no aperture plate (M2). The uncertainties in measured beam energy, or the error bars, are smaller than the point size.

Earlier published data at higher B_H fields of 1200 G and with a mechanical aperture located in front of the magnetic nozzle coil (Ref. 1), showed qualitatively similar behavior, i.e., a 5% decrease in ion energy, E_i, with increasing B_n, for $0 < B_n < 2000$ G, but E_i rising 3% for 2000 G $< B_n <$ 3000 G. Those earlier results showed considerably higher flow energies (E_i ~ 18 eV) and speeds, M ~ 1.7 at z = -2 cm. At these lower B_H values, $R < 4$ at B_n = 2000 G, the effect of the nozzle magnetic field is qualitatively similar to that of a purely magnetic aperture [10].

B. Mechanical aperture plate

By placing the aperture plate (AP) at four different positions relative to the midplane of the magnetic-nozzle coil, we investigated the effect of aperture-plate location on the parallel ion flow speed. A 0.1 eV argon ion would have a gyroradius of 0.1-1 cm (5000-500 G), comparable to the radii of the various apertures used, 0.25-0.4 cm. The transit time for ions, accelerated by the presheath to 5 eV, to pass through the thin aperture plate is 2-20 times shorter than the ion gyroperiod. Independent of aperture plate installation, the ion flow speed (energy) in the center of the main chamber is very small, less than 0.03 eV. The perpendicular ion temperature is slightly higher, ~ 0.05-0.5 eV. Thus, ions pass through the aperture on nearly straight lines, within 30° of the plate normal.

B.1 Aperture plate immediately upstream of nozzle coil

With the AP positioned as shown in Fig. 4-3b, just upstream of the AP, at $z = -2.3$ cm, the ion flow energy increases to 1.1 eV (Fig. 4-5). After the AP and nozzle region, the ion flow energy increases further to 13.0 eV at $z = 2.4$ cm. By $z = 7.4$ cm, the ion beam energy is up to 17.7 eV. Coexistent with the ion beam is a low-energy population in the ER. Throughout this paper we use terminology: high energy particles are called HEP; low energy particles are called LEP. The LEP, represented by the diamond symbols in Fig. 4-5, has zero net flow throughout the expansion region. The lack of LEP net flow persists even in the DL where the HEP ions accelerate from 7800 m/s (12.7 eV) to 9200 m/s (17.6 eV) in 4.6 cm. These observations are consistent with conventional picture of DL [11,12,13,14], numerical simulations [15,16] and LIF measured IVDFs in HELIX-LEIA that were described in Chapter 3 of this work.

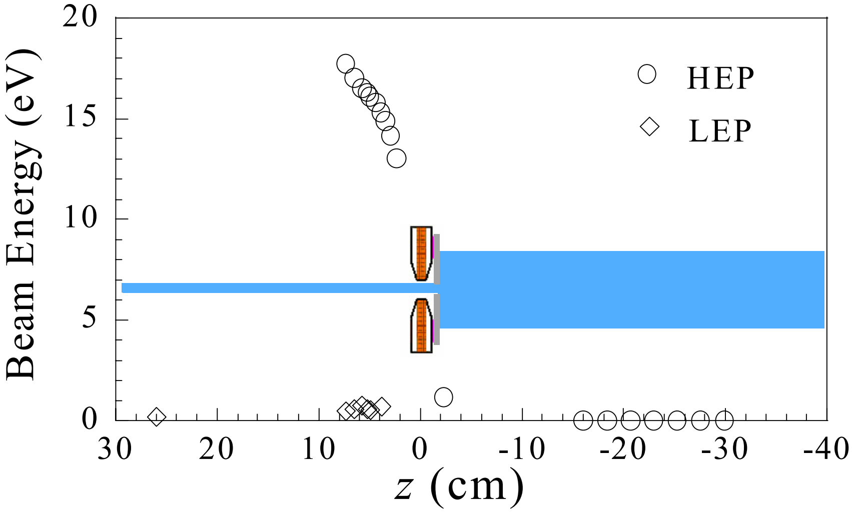

Figure 4-5. The beam energy versus *z* for AP at z = -1.8 cm and plasma conditions of rf power *P* = 600-900 W; B_H = 580 G; B_N = 2250 G; P_M = 0.6mTorr; P_{ER} = 0.3-0.7 mTorr. The open diamonds, open circles, and solid circles denote the parallel kinetic energy of LEP, and HEP ions

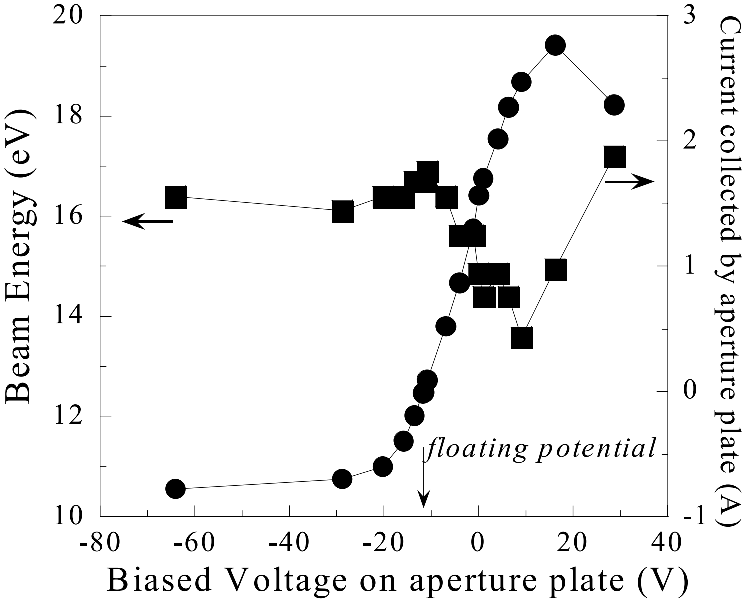

Figure 4-6. The ion beam energy versus the bias voltage on the aperture plate at *z* = -3.2 cm for rf power of 700-800 W, B_H = 580 G, B_N = 1700 G, P_M = 0.7 mTorr, and P_{ER} = 0.3 mTorr. The aperture plate was at *z* = –1.8 cm

Fig. 4-6 shows the ion-beam energy measured at z = 3.2 cm and the current collected by the aperture plate *versus* a bias voltage applied to the AP. The minimum ion beam energy occurs at a bias voltage of 9.1 V (close to the measured plasma potential of 9.8 ± 1.0 V). When the AP is biased more negative than the plasma potential, the ion beam energy increases until the bias voltage equals the floating potential. Further decreases in applied bias potential lower the ion beam energy slightly. At the negative potentials, -30 to -70 V, the AP collects ion saturation current. A bias voltage above the plasma potential, from 10 to 30 V, also increases the ion-beam energy. Electron saturation current to the AP is not achievable with the current and voltage capabilities of the AP biasing power supply.

For an expanding, two-electron-temperature plasma terminated with a metal plate at one end, *Hairapetian* and *Stenzel* reported that the DL amplitude decreased as an increasing positive bias voltage was applied to the end plate [17, 18]. They reported that the DL disappeared at large positive bias voltage and that negative bias voltages had no effect on their DL. Consistent with their results, a large negative bias voltage had little effect on the ion beam energy in these experiments. However, the detailed LIF measurements indicate that the ion beam energy does decrease slightly with negative bias until the bias AP enters ion saturation – suggesting a slight weakening of the DL until the maximum ion current is pulled through the sheath onto the AP. Similarly, and consistent with the Hairapetian and Stenzel observations, the ion beam energy also decreases with increasing positive AP bias voltage until the bias voltage equal to 9.1 V or close to the plasma potential (9.8 V). We hypothesize that increasing the electron current into the DL (through the positive bias voltage), increases the ratio of thermal to energetic electron densities – thereby decreasing the strength of the DL [17,18]. In contrast to the *Hairapetian* and *Stenzel* results, at large positive bias voltages (when the AP enters into electron saturation, or for bias voltages larger than the plasma potential) the ion beam energy returns to the same level as when the AP was biased at the negative potential.

B.2 Aperture plate near center of the source chamber

With the AP inserted into the plasma, the parallel ion kinetic energy at $z = 3.0$ cm increased from 9 eV (Fig. 4-4) to 14 eV (Fig. 4-5). To better understand the effect of the AP, we separated the AP (mechanical aperture) and nozzle (magnetic aperture) by positioning the AP near the center of the source (main) chamber, between –29.1 and -29.4 cm, see Fig. 4-3c). The viewing geometry in this configuration allowed spatially resolved measurement of parallel ion flow speeds around both the mechanical and magnetic apertures. As shown in Fig. 4-7, ions begin to accelerate at $z = -31.4$ cm and enter the aperture hole with an energy of 7.2 eV at $z = -29.4$ cm (Fig. 4-7). The ions keep accelerating as they transit the aperture and reach 20.4 eV at $z = -28.9$ cm (Fig. 4-7). Further downstream of the AP, at $z = -28.1$ cm, the ions accelerated to 39.5 eV ~ 7 T_e. Thus, the ions accelerated from 7.2 eV to 39.5eV in 1.2 cm, ~ 2000 ${}_s\lambda_D$ or ~ 200 ${}_{ER}\lambda_D$.

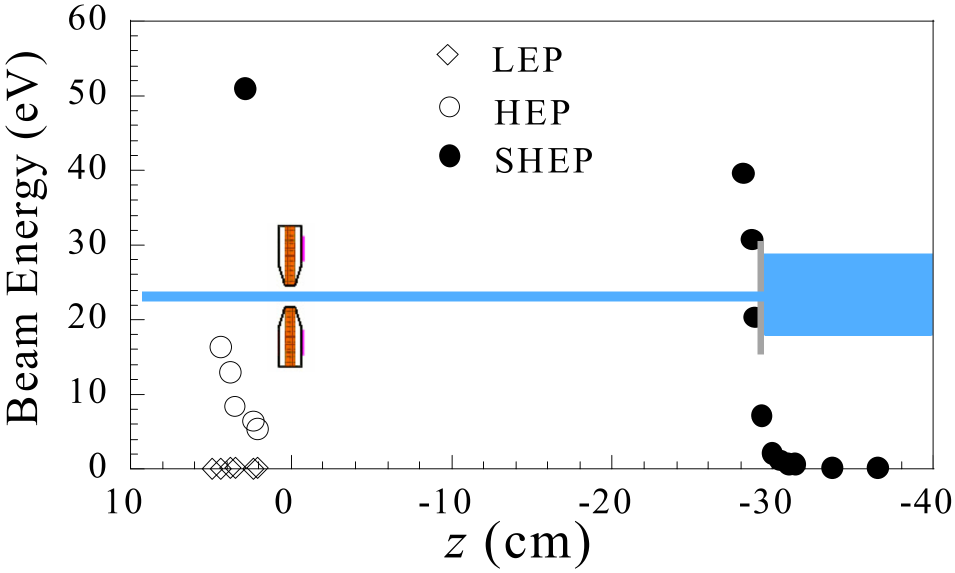

Figure 4-7. AP at z = -29.4 cm and plasma conditions of $P = 800$ W; $B_M = 580$ G; $B_N = 1100$ Gauss; $P_M = 0.51$ mTorr; $P_{ERB} = 0.11$mTorr. For measurements in main chamber, the nozzle magnetic field strength was decreased to 200 Gauss. The open diamonds, open circles, and solid circles denote the parallel kinetic energy of LEP, HEP, and SHEP (Super High Energy, relative to the HEP and LEP, Population).

In the expansion region beyond the nozzle coil ($z > 1$ cm), three ion populations are observed, see Fig. 4-7. The LEP ions with parallel kinetic energy ~ 0.1 eV are produced locally in the expansion region. We suggest that the ions with kinetic energy ~16.3 eV at $z = 4.4$ cm (~7 eV at $z = 3$ cm, as shown in Fig. 4-7) were created in the region between the AP and the nozzle coil and then accelerated through a DL at the nozzle, gaining ~ 16 eV in transit. A third, super-high-energy, population (SHEP) is observed downstream of the nozzle ($z = 2.9$ cm) having a flow energy of 51 eV. The 51 eV energy is consistent with the observation of a roughly 40 eV energy increase at the AP followed by a 7-10 eV increase at the magnetic nozzle at $z = 2.9$ cm. In other words, this configuration of a mechanical AP followed by magnetic nozzle leads to the formation of two distinct double layers.

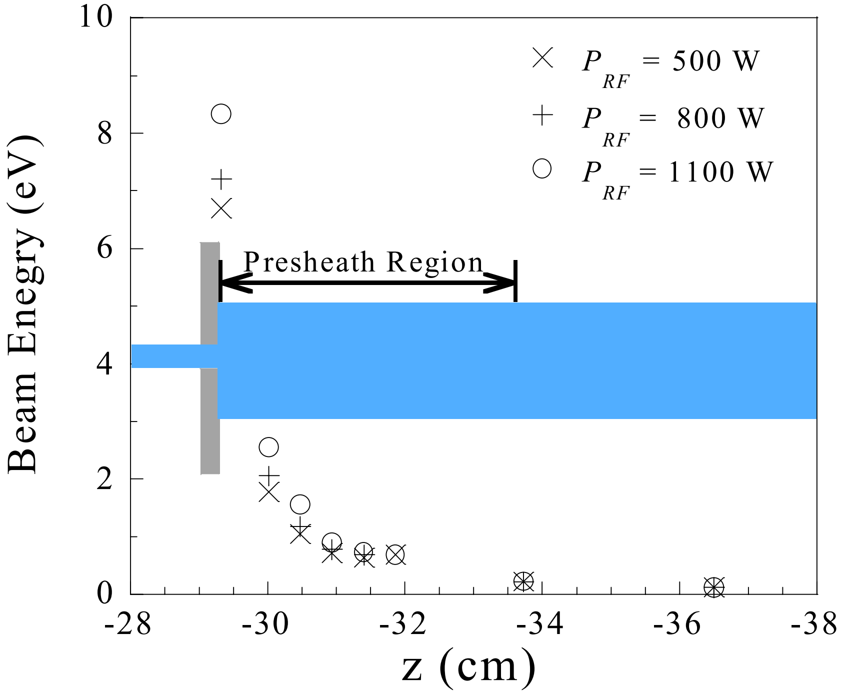

Figure 4-8. The ion beam energy in the presheath for rf powers of 500 (solid circles), 800 (solid squares) and 1100 (solid diamonds) Watts. B_H = 580 G and P_M = 0.5 mTorr**.** Aperture plate at $z = -29.4$ cm (right surface).

Since a DL is essentially a plasma sheath that forms in the interior of a plasma, a presheath must arise to match the plasma potential to that of the DL [19]. To satisfy the Bohm Criterion for ions falling into the sheath at the edge of the DL, the ions must reach a minimum parallel energy of ½ kT_e by passing through the presheath. The measured ion acceleration before the DL is shown in Fig. 4-8 for the AP placed at $z = -29.4$ cm. The ions begin to accelerate ~3 cm before the plate, approximately equal to the expected length of the presheath, the ion-neutral collision length [4,5]. The beam energies at the aperture are 6.7 eV, 7.2 eV, and 8.3 eV for 500, 800, and 1100 Watts of RF power. Langmuir probe measurements at $z \approx -32 \pm 0.15$ cm indicate that the electron temperatures are 8.0 ± 1.0 eV, 8.4 ± 1.0 eV, and 8.4 ± 1.0 eV. Thus, the ion beam energies at the aperture are consistent with the ions falling through at least a $kT_e/2e$ potential drop in transiting the presheath. The presheath region, as indicated in Fig. 4-8, is 4-5 cm, which, as noted before is approximately equal to the ion-neutral mean-free-path of 3-5 cm. Thus, the thickness of the presheath is consistent with Riemann's sheath model. However, similar to *Oksuz and Hershkowitz*'s experiment [5], the potential drop over the presheath is ~ T_e/e, instead of $kT_e/2e$ in Riemann's model. The exiting ion flow energies at z = -27.6 cm, about 1.5 cm from the exit of aperture, are 36.5, 39.6, and 47.8 eV for these three rf power values, *i.e.* the strength of sheath DL increases with increasing rf power.

Note that although the plasma parameters upstream of nozzle are dramatically different in Fig. 4-5 and Fig. 4-7, the strength of DLs formed by the nozzle magnetic field are nearly identical, about 20 V or ~$3kT_e/e$. Although no spatial scan was performed for the configuration without an aperture plate, the increase in ion kinetic energy close to the magnetic aperture is approximately the same, 7.0 eV at $z = 3.0$ cm with $B_N = 2250$ G, for configurations 4-2a and 4-2c. Thus, these measurements suggest that the nozzle magnetic field creates an overall 20 V potential drop along the axis even though the detailed DL structure does depend on the upstream plasma parameters (as indicated by the data presented in Fig. 4-5 and Fig. 4-7).

B.3 Aperture plate in the expansion chamber

The floating potential achieved by an electrically floating AP placed in the expansion region of the experiment is indicative of the energy, i.e., the temperature, of the electron population in the plasma. Shown in Fig. 4-9 are measurements of the z-directed ion energy at z = 5.3 cm for the AP at z = 4.5 cm (the AP position as indicated in Fig. 2d) and the aperture-plate floating potential *versus* nozzle magnetic field strength. Both the ion flow energy and the floating potential of the AP increase with decreasing nozzle magnetic field strength. The large negative floating potential, up to –75 V, of the electrically isolated aperture plate in the expansion chamber suggests the existence of energetic electrons in the plasma. The existence of energetic electrons in helicon sources, possibly resulting from Landau damping of the helicon wave, has long been debated amongst the helicon source community [20]. Reports of energetic electrons in long, low axial-power density, higher neutral pressure helicon plasmas indicated that the energetic population was less than $\sim 10^{-4}$ of the bulk, thus the Landau damping explanation for the high ionization efficiency of helicon sources has fallen into some disfavor [21,22]. However, the LIF measurements presented here, for a relatively short, higher power-density device, indicate a strong correlation between the mechanism responsible for determining the strength of the DL and the floating potential of the AP – possibly a result of DL formation being controlled by a population of energetic electrons in the helicon source.

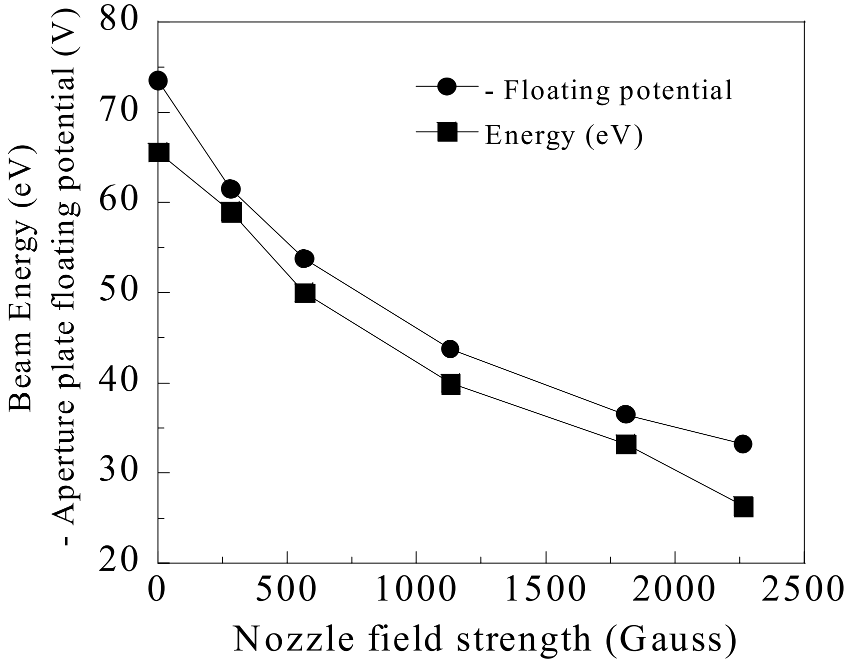

Figure 4-9. The ion beam energy (solid circles) at z = 14.8 cm and absolute value of aperture plate floating potential (solid squares) versus the nozzle field strength for rf power of 720-850 W, B_H = 580 G, P_M = 0.5 mTorr, and P_{ER} = 0.12-0.24 mTorr. The aperture plate was at z = 14.0 cm (left surface) in the ER.

If the high floating potential of the AP results from an energetic electron population, the same population of energetic electrons should determine the strength of the ion-accelerating DL and both the AP floating potential and the ion beam energy will have similar dependencies on the source parameters [17]. Note also that if the higher nozzle field strength results in more energetic electrons reflected back into source [23], i.e. fewer energetic electrons can reach the AP downstream of nozzle, the decrease in the strength of the DL and the decrease in the AP floating potential with increasing nozzle magnetic field strength are easily explained. Typically it is expected that an increasing magnetic nozzle field strength leads to higher energy ion beams. These results indicate that if the ion beam is created in a DL at a magnetic nozzle, a weaker nozzle magnetic field that does a poorer job of confining the energetic source electrons is more effective at ion beam creation and acceleration.

In summary, near and in the DL the trapped ion velocity distribution is well represented by a single, nearly stationary Maxwellian velocity distribution. The measured free ion speeds reveal the DL formed by nozzle is about $3kT_e/e$, independent of the upstream ivdf and EEDF. Acceleration of ions up to -- and exceeding -- the ion sound speed (determined by the bulk electron temperature) is observed in the presheath upstream of the DL. The potential drop over the presheath is $\sim kT_e/e$. Multiple double-layer structures were produced by first creating a DL at an electrically floating plate placed in the plasma source chamber. Then, the plasma downstream of the first DL flowed through a second DL created by a rapid plasma expansion in the divergent magnetic field of a magnetic nozzle coil. That a mechanical aperture can create a DL with strength $\sim 6kT_e/e$ and thereby increase the exit velocity of ions flowing through an additional DL further downstream suggests that a sequence of appropriately sized apertures could be used to increase the specific impulse of plasma thrusters or other systems used to create ion beams.

Perhaps the most significant result from this work is that for expanding helicon source plasmas the ion beams created by the DL in a magnetic aperture appear to depend on the energetic electron population that can escape the source region.

Further studies are still needed to explore the relationship between DL strength and aperture size, the dependence of the threshold pressure for DL formation on gas species and neutral gas temperature, and the effects of multiple gas species on the strength of the DL.

Chapter 4 References

[1] S. A. Cohen, N. S. Siefert, S. Stange, R. F. Boivin, E. E. Scime, and F. M. Levinton, Phys. Plasmas **10**, 2593 (2003)

[2]R. F. Boivin and E. E. Scime, Rev. Sci. Instrum. **74**, 4352 (2003)

[3] P. C. Stangeby, Plasma Sheath in Physics of Plasma-Wall Interactions in Controlled Fusion Devices (Plenum Press, 1984)

[4] K.U. Riemann, Phys. Plasmas **4**, 4158 (1997)

[5] L. Oksuz, and N. Hershkowitz, Phys. Rev. Lett. **89**, 145001 (2002)

[6] N. Hershkowitz, Phys. Plasmas **12**, 055502-1 (2005)

[7] S. A. Andersen, V.O. Jensen, P. Nielsen, and N.D' Angelo, Phys. Fluids **12**, 557 (1969)

[8] A. V. Arefiev, and B. N. Breizman, Phys. Plasmas **11**, 2942 (2004)

[9] F. Chang-Diaz, Sci. Am. **283**, 90 (2002).

[10] X. Sun, C. Biloiu, R. Hardin, and E. Scime, Plasma Sources Sci. Technol. **13**, 359 (2004)

[11] M. A. Raadu, Physics Reports **178**, 25 (1989)

[12] L. P. Block, Astrophys. Space Sci. **55**, 59 (1978)

[13] N. Hershkowitz, Space Sci. Rev. **41**, 351 (1985)

[14] B. H. Quon, and A. Y. Wong, Phys. Rev. Lett. **37**,1393 (1976)

[15] A. Meige, R.W. Boswell, C. Charles, and M. Turner, IEEE Trans. Plasma Sci. **33**, 334 (2005).

[16] A. Meige, R.W. Boswell, C. Charles, and M. Turner, Phys. Plasmas **12**, 052317 (2005).

[17] G. Hairapetian, and R. Stenzel, Phys. Fluids B **3**, 899 (1991)

[18] G. Hairapetian, and R. Stenzel, Phys. Rev. Lett. **65**, 175 (1990)

[19] N. Hershkowitz, IEEE Trans. on Plasma Sci. **22**, 11 (1994)

[20] F. F. Chen, Plasma Phys. Controlled Fusion **33**, 339 (1991)

[21] A. W. Molvik, T. D. Rognlien, J. A. Byers, R. H. Cohen, A. R. Ellingboe, E. B. Hooper, H. S. McLean, B. W. Stallard, and P. A. Vitello, J. Vac. Sci. Technol. A **14**, 984 (1996)

[22] F. F. Chen, and D. D. Blackwell, Phys. Rev. Lett. **82**, 2677 (1999)

[23] F. F. Chen, Introduction to Plasma Physics and Controlled Fusion, 2nd edition (Plenum, New York, 1974)

Chapter 5: Asymmetric Optical Pumping

5.1: Asymmetric LIF signal

As described in Chapter 2, in a laser-induced-fluorescence (LIF) measurement of the ion velocity-space distribution function (ivdf) in a plasma, the frequency of a narrow-linewidth, tunable laser is scanned across an absorption line of an ion in the plasma and fluorescent emission from the excited state measured as a function of laser frequency [1,2]. The Zeeman effect due to a magnetic field creates several absorption lines between the initial lower and upper states. Each Doppler-broadened line is pumped at slightly different frequencies by a particular polarization of the incident photons, i.e., linearly polarized π lines and circularly polarized +/-σ lines. Because their energies are nearly the same, the different initial Zeeman sublevels should be equally populated in plasma with electron temperature of several eV. In this chapter, we describe observations of up to a factor of 2.5 difference in the amplitude of the LIF signal from Zeeman sublevels pumped with right- and left-circularly polarized photons for argon ions accelerating along a weakening magnetic field. This effect should be considered in many situations, such as interpretation of resonant scattering observed in the solar corona [3,4]. In stellar coronas or in laboratory plasmas, the magnetic field and plasma velocity may change rapidly, perhaps by turbulence, strongly affecting the Stokes V spectrum (the wavelength dependent amplitude difference between Zeeman split σ lines [3]) and its interpretation. Field and velocity gradients effects have had significant impact in other resonance spectroscopies, such as NMR [5].

Until now, the only way to determine plasma density with LIF (for plasmas in which Stark broadening is negligible) has been to relate the plasma density to the intensity of the emitted fluorescent light with an absolutely calibrated light-collection apparatus and a known incident laser power. In this chapter, we demonstrate that the asymmetry in the +/- σ LIF signals from Zeeman sublevels is a strong function of the ion collisionality and therefore an uncalibrated LIF system can provide remote measurements of the local plasma density for highly ionized plasmas.

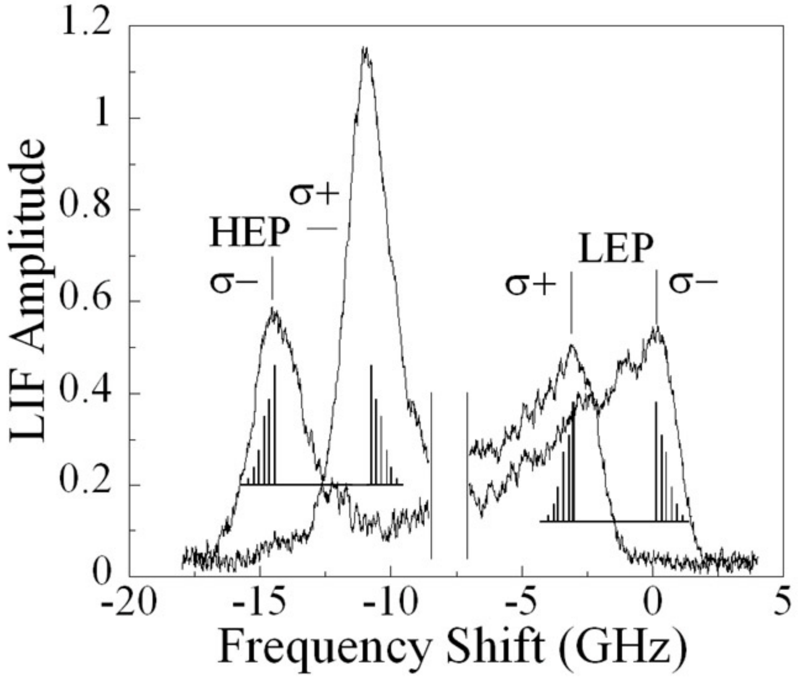

Figure 5-1. LIF signal for right (σ-) and left (σ+) circularly polarized laser light versus difference between laser frequency and natural frequency of the absorption line. Data were obtained 2.9 cm in front of the plasma limiting aperture for B_H = 465 G, B_N = 1995 G, source rf power P = 550 W, and neutral pressures of 0.6 mTorr and 0.23 mTorr in the source and ER, respectively. The vertical lines indicate the transition frequencies of Zeeman sublevels relative to the natural absorption frequency.

The experiments were performed in the Magnetic-Nozzle-eXperiment (MNX) facility (see Fig. 4-1). The linearly polarized laser beam is passed through a quarter-wave plate to create either right- or left-circularly polarized light and then propagates along the plasma axis from the ER towards the plasma source. Presented in Fig. 5-1 are LIF measurements obtained using both left- and right-circularly polarized light. In each measurement, a low-energy (LEP) ion population and a high-energy (HEP) ion population (kinetic energy ~ 20 eV) are evident. The LEP is the result of local ionization of neutral argon; the HEP is produced by argon ions that accelerated through the aperture [*6*]. The amplitude of the σ+ component in the HEP is ~2 times higher than the σ-component, yet the σ+ and σ- signal amplitudes for the locally produced LEP population are equal. The six Doppler-broadened components of each of the σ clusters are shown as vertical lines in Fig. 5-1, scaled according to their statistical weights.

5.2 Analysis of Asymmetric Optical Pumping

As a function of the magnetic-nozzle field strength, B_N, the $\sigma+$ and σ- LIF signal amplitudes (A^+ and A^-, respectively) 2.9 cm downstream of the nozzle midplane (z = 2.9 cm) are shown in Fig. 5-2. The asymmetry ratio $R, R \equiv A^+/A^-$, increases with B_N to R ~ 2.2 at B_N = 1700 and then decreases slightly for larger values of $B_{N.}$ (In the center of the helicon source, the magnetic field strength was B_H = 465 Gauss and the neutral pressure was 0.6 mTorr.) $R > 1$ can arise from either enhanced absorption/fluorescence from the $\sigma+$ ion LIF sequence or suppressed absorption/fluorescence from the σ- sequence. In Chapter 2 we demonstrated that, in helicon plasmas, the LIF intensity for Ar II is proportional to the square of the electron density times the square root of the electron temperature ($n_e^2 T_e^{0.5}$). The solid line in Fig. 5-2 is a linear fit to $n_e^2 T_e^{0.5}$ measurements *versus* the nozzle field strength at z = 7.0 cm in the expansion region. That the scaling of the $\sigma+$ LIF intensity *versus* the nozzle field strength is nearly identical to that of the $n_e^2 T_e^{0.5}$ measurements indicates that $R > 1$ arises because of a depletion of ions in the initial state of the σ- sequence compared to the $\sigma+$ sequence. In other words, at the observation point there are fewer ions in the initial state of the σ- sequence absorbing the laser light than in the $\sigma+$ state. Measurements at large values of B_N (B_H = 597 G, B_N = 2223 G, and P_M = 0.6 mTorr) also indicate that the parallel ion kinetic energy increases from 13 eV at z = 2 cm to roughly 18 eV at z = 7 cm. Thus, as the ions move from a strong magnetic field in the nozzle coil to the weaker magnetic field in the ER, the σ-Zeeman-split states for the accelerating ions somehow become less populated than the $\sigma+$.

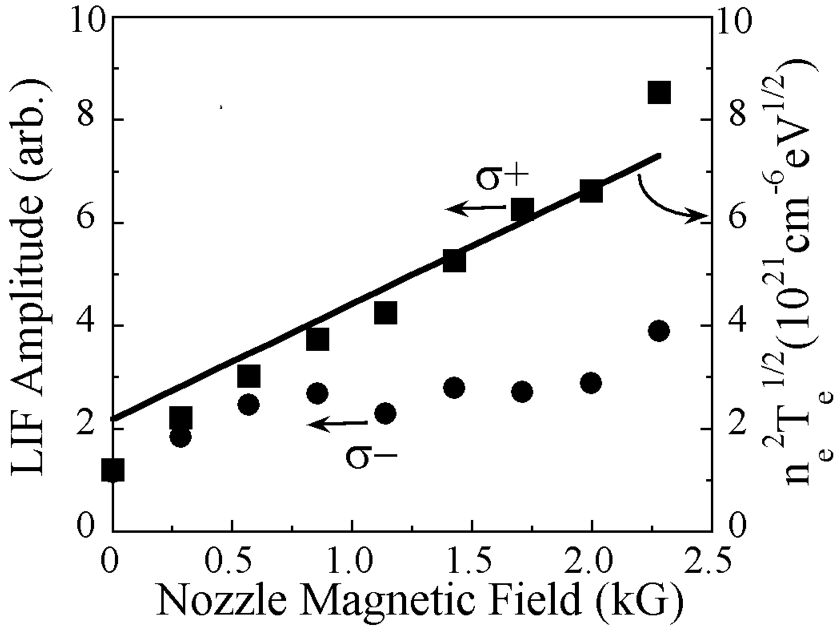

Figure 5-2. The individual *σ*+ and *σ*- peak LIF signal amplitudes at z = 2.9 cm versus nozzle magnetic field strength for P = 580 W, B_H = 465 G, P_M = 0.6 mTorr. The solid line is a linear fit to measurements of $n_e^2T_e^{1/2}$ at z = 7.0 cm.

A number of possible explanations for the asymmetry in LIF intensities can be excluded. Creation of a spin-polarized beam by the longitudinal Stern-Gerlach effect [*7*,*8*] is implausible given the very small (~ 1.0×10^{-5} eV) energy splitting of these two σ clusters compared to the thermal and kinetic energies of the HEP, typically 0.5 eV and 20 eV. The absence of any asymmetry in the LIF intensities from the σ clusters of the LEP ions rules out creation of a spin polarized beam by the transverse Stern-Gerlach effect arising from the field gradients at the end of the solenoidal field. The magnetic-field-strength-dependent Hanle effect can enhance the absorption of particular ion or atomic transitions. (In the Hanle effect, the energy of a Zeeman sublevel that increases with increasing magnetic field strength can equal the energy of a Zeeman sublevel that decreases with magnetic field – thereby creating a degeneracy between the two states for a particular magnetic field strength) [*9*]. However, for these Ar II transitions, magnetic fields above 10 T would be required to obtain a level crossing between the initial $3d^4F_{7/2}$ state and the closest other ion states. Differences in the optical depth for the wavelengths corresponding to the peak of each of the σ clusters could also lead to an asymmetry in the LIF signal intensity. However, the measured absorption for each circular polarization over the entire 2–m length of the plasma was less than 1%. We also considered the Babcock procedure, typically used to measure sub-Doppler Zeeman splittings in stellar atmospheres. In the Babcock method, the circularly polarized emission intensities from two thermally broadened, closely spaced, Zeeman-split σ lines are measured simultaneously at a wavelength slightly offset from the unshifted line [10]. The difference in emission intensity is then directly proportional to the strength of the magnetic field at the point of measurement. In contrast, in our experiments the entire line shape of each Zeeman sublevel is measured and the peak intensities compared. Thus, although this effect gives a result similar to a Babcock-type measurement and could therefore be misinterpreted as evidence of a stronger than actual magnetic field in an astrophysical measurement, the physics responsible for the difference in signal intensities is not the same. To rule out effects due to changes in the laser power during each frequency scan, the LIF intensity measurements presented here have been normalized to the instantaneous laser power. Finally, to rule out any bias in the polarizing optics, the magnetic field direction was reversed and the measurements repeated. For both directions of the magnetic field, the LIF signal of the higher frequency $\sigma+$ HEP cluster was consistently larger than that of the $\sigma-$ HEP cluster while those of the $\sigma+$ and $\sigma-$ LEP stayed equal .

Other groups have demonstrated that saturation of an absorption line used for LIF can begin at laser intensities comparable to those used in these experiments ($I \sim 1$ W/cm^2) [11]. We hypothesized that if the interaction time between the laser and the ions was different for ions in the initial $\sigma+$ state compared to those in the initial state for the $\sigma-$ transition sequence, the LIF signal from the two transition sequences could differ. For example, if upstream of the observation volume, ions in the initial $\sigma-$ state were in resonance with the laser for more time than ions in the initial $\sigma+$, the population of $\sigma-$ state ions in the observation volume could be depleted – yielding a smaller LIF signal for that transition compared to the $\sigma+$. Fig. 5-3 presents a schematic view of how the resonant interaction times would differ for ions in different Zeeman split states that accelerate through a magnetic-field gradient. The solid curve represents the decreasing magnetic field, the arrows indicate the direction of the ion velocity (and acceleration) and the laser-beam propagation. Close to the magnetic nozzle (at location *a*), the magnitude of the Zeeman shift of the σ lines relative to laser frequency at which the transition would appear in the absence of a static magnetic field (shown as a thick vertical line) is larger than further from the magnetic nozzle (at location *b*). Because the ions are accelerating towards the laser, the entire transition sequence shifts to a lower laboratory-frame frequency. Note that for measurements made at location *b*, when the laser is tuned to peak of the $\sigma-$ line (dashed vertical line in Fig. 5-3), the σ- state ions at the upstream location *a* are also pumped by the laser. Therefore, as the σ- state ions travel along the laser beam towards the measurement location their Zeeman and Doppler shifts can cancel – for appropriate velocity and field gradients – and the σ- state ions are can be pumped by the laser for a much longer time than the σ+ state ions.

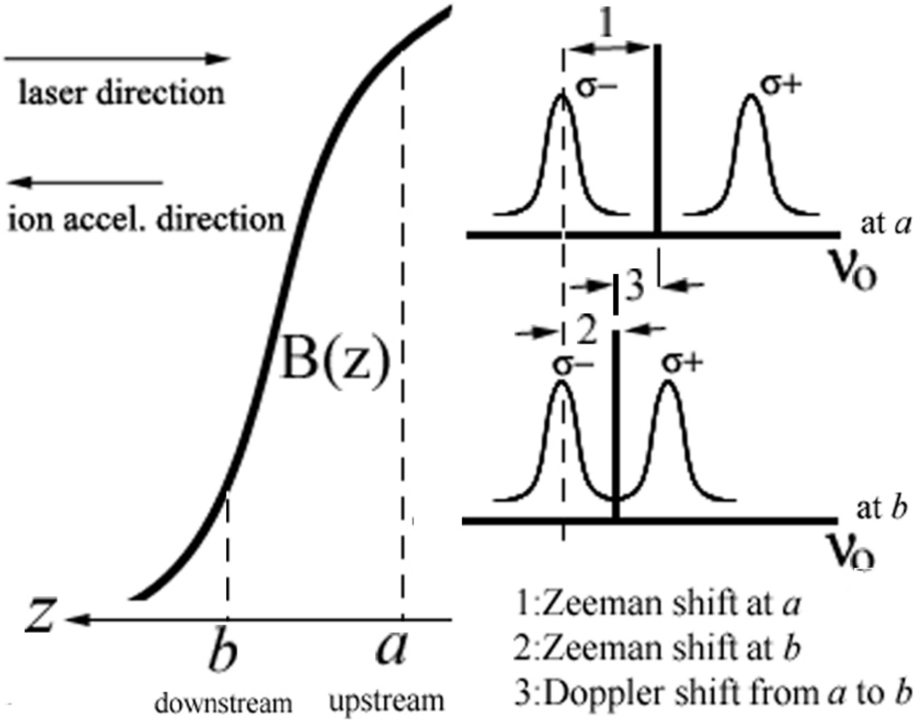

Figure 5-3. Changes in absolute frequency of absorption lines due to Zeeman and Doppler shifts as ions accelerate through a magnetic field gradient (solid curve).

Absorption out of the i^{th} state of HEP ions is described by [11]

$$-\frac{d}{dt}N_i(z) = N_i(z)\frac{B_{ij}}{4\pi}\int_0^{+\infty} d\nu\, L_i(\nu) I(z,\nu,t)\,, \tag{5-1}$$

where we have assumed that the HEP metastable ions are created in the nozzle region by electron impact excitation of ground state ions and travel into the ER where they are pumped by the laser. (Cascades from other metastable states or stimulated emission from the upper state are unimportant to the metastable density in this experiment, consistent with the σ+ data shown Fig. 5-2.) N_i(z) is the density of the i^{th} Zeeman sublevel of state $3d^4F_{7/2}$ at location z in the experiment. B_{ij} is the Einstein coefficient for absorption to the j^{th} sublevel of the state $4p^4D_{5/2}$, where j = i ± 1 for σ+ and σ– transitions. For B_{ij} we use the zero magnetic-field value, $B_{ij} \equiv E = 8.037\times10^{12}\,\mathrm{m}^2(\mathrm{Js})^{-1}$. $I(z,\ \nu,\ t) = I_0\delta(\nu-\nu_0)$ is the monochromatic laser intensity at frequency ν_o and $L_i(\nu) = \left(W_i\big/\sqrt{\pi\alpha_D T}\right)\exp\left(-\left(\nu-\nu^*\right)^2\big/\alpha_D T\right)$ is the thermally broadened line shape of the i^{th} Zeeman sublevel, where W_i is the statistical weight of the i^{th} line, T the ion temperature, m_i the ion mass, and $\alpha_D = 2k_B\nu_o^2\big/m_i c^2$. In the laboratory frame, $\nu-\nu^* = \nu-[\nu_I+\alpha_i B(z)][1-V(z)/c]$, where ν_I is the natural frequency of the $3d^4F_{7/2}$ to $4p^4D_{5/2}$ transition, α_i is the Zeeman frequency shift for the i^{th} sublevel, $B(z)$ is the magnetic field in kGauss and $V(z)$ is the ion velocity. The factor of $1-V(z)/c$ accounts for the Doppler shift of the absorption line.

The length of time, t_r, before reaching the measurement location that ions may remain in resonance with the laser [12] is governed by the time between collisions for ions with background neutrals, electrons, and other ions: $t_r \equiv 1/\nu_i$, where ν_i is the total ion collision frequency. Rewriting Eq. (5-1) in terms of the travel distance of the resonant ions, $\Delta z = V(z)/\nu_i$, yields the fraction of ions pumped out of the initial LIF state:

$$\frac{\Delta N_i(z)}{N_i}=\frac{E}{4\pi}\frac{W_i}{\sqrt{\pi\alpha_D T}}\int_{z-\Delta z}^{z}\frac{1}{V(z)}e^{-\frac{[\nu_o-(\nu_I+\alpha_i B(z))(1-V(z)/c)]^2}{\alpha_D T}}dz\,. \qquad (5\text{-}2)$$

The LIF signal at z_o for a laser tuned to ν_o is proportional to the fluorescent emission due to laser pumping of the remaining fraction of initial state ions summed over the six sublevel transitions:

$$A^{\pm}(z_o)=\sum_{i=1}^{6}A_i^{\pm}(z_o)\propto\sum_{i=1}^{6}\left[(1-\frac{\Delta N_i(z_o)}{N_i})M_i\int_0^{\infty}e^{-\frac{[\nu-(\nu_I\pm\alpha_i B(z_o))(1-V(z_o)/c)]^2}{\alpha_D T}}I_o\delta(\nu-\nu_o)d\nu\right]$$

(5-3)

Eq. (5-3) describes the LIF intensity from σ+ or σ– ion states including any depletion of those states due to changing Zeeman and Doppler shifts for ions accelerating along the laser beam in a magnetic field gradient before they reach the measurement location. Note that the ratio of $R = A^+/A^-$ predicted by Eq. (5-3) has no free parameters. To numerically integrate Eq. (5-3), we approximated the parallel ion flow and magnetic-field-strength gradients with simple fits to the measured ion flow and magnetic field values: $V(z)=267.2z+7490$ m/s and $B(z)=B_N(1+(z/3.0)^2)^{-3/2}$ kG , with z in cm. The measured plasma density (n_e = 7.5×10^{10} cm^{-3}), electron temperature (T_e = 6 eV), ion temperature (T_i = 0.2 eV), and neutral pressure (0.7 mTorr) in the expansion region were used to calculate the limits of integration. For these parameters, the total ion collision frequency is dominated by the fast ion on background neutrals collision rate [13] and is therefore independent of the electron temperature.

Measured and calculated values of R as a function of B_N are shown in Fig. 5-4 for the opposite magnetic field orientation used to obtain the data of Fig. 5-2. Experimental conditions were: B_H = 582 Gauss and neutral argon pressure = 0.7 mTorr. The total ion collision frequency, based on the measured plasma parameters and calculated using the collision cross-sections given in Ref. [13], is $\nu_i = 2.2 \times 10^5\ s^{-1}$. R curves are shown for ν_i, $10\nu_i$ and $\nu_i/10$.

Also shown in Fig. 5-4 are the measured and predicted parallel inferred ion temperature ratios ($T_{\sigma+}/T_{\sigma-}$) based on the measured HEP spectral profiles. That is, the enhanced interaction of σ- state ions with the laser distorts the measured parallel ivdf and affects the parallel ion temperature values obtained from Maxwellian fits to the LIF measurements. By varying the value of the laser frequency used in Eq. (5-3), a predicted ivdf measurement, and therefore a predicted value of $T_{\sigma+}/T_{\sigma-}$ is obtained. The predicted R values for the ion collision frequency based on the measured plasma parameters are in excellent agreement with the measurements. The dependence of $T_{\sigma+}/T_{\sigma-}$ on magnetic nozzle field strength is generally consistent with the model predictions. The divergence between the measured and predicted values of $T_{\sigma+}/T_{\sigma-}$ above 1 kG is due to difficulties in fitting Maxwellians to the highly asymmetric distributions predicted by the model for large magnetic nozzle field strengths. The peak in R at a specific value of B_N is accurately reproduced by the numerical calculations (at large B_N the Doppler and Zeeman shifts are no longer commensurate). Factor of ten variations in the collision frequency yield predicted R values that are clearly at odds with the measurements. The measured dependence of R on z (not shown) also agrees with the model, e.g., $R > 1$ and R increases with distance from the aperture as the effects of the field and velocity gradients increase. When the ion acceleration region did not overlap with the magnetic field gradient (accomplished by moving the aperture deep into either the source or ER), $R = 1$ was observed in all cases.

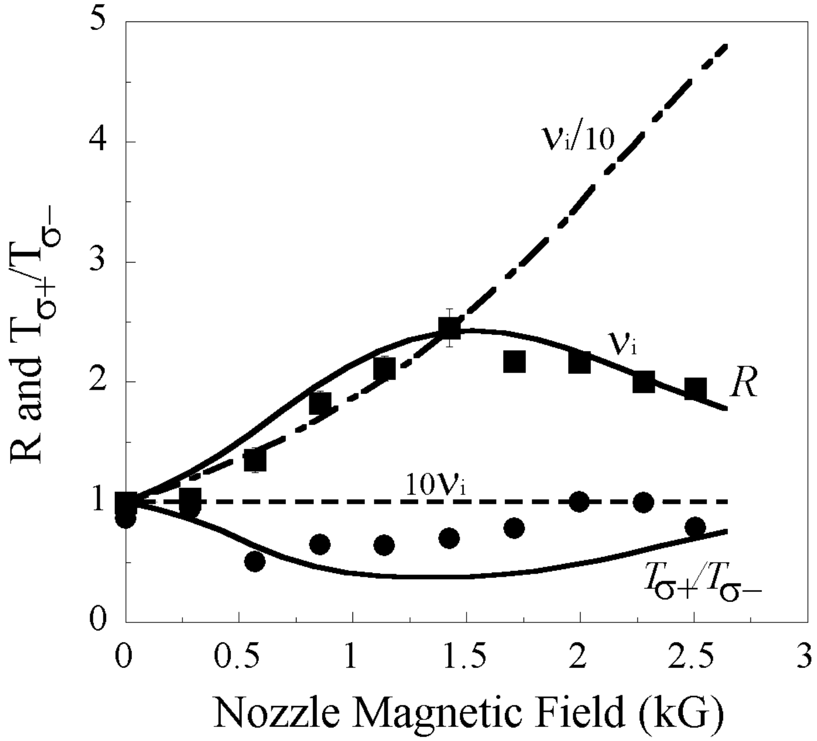

Figure 5-4. Measured (solid squares and error bars) and predicted (solid (ν_i), dashed ($10\nu_i$), and dashed-dot line ($\nu_i/10$)) values of R versus B_N at $z = 2.9$ cm for P = 750 W, $B_H = 582$ G, and $P_M = 0.7$ mTorr. Also shown are the measured (solid circles) and predicted values (solid line) for $T_{\sigma+}/T_{\sigma-}$

In summary, asymmetry in LIF emission from + and - σ states of metastable argon ions was observed and attributed to the combined effects of magnetic-field and ion-velocity gradients. This phenomenon should be considered in both laboratory and stellar plasmas where, for example, turbulence or flows can generate the requisite gradients. In stellar plasmas, the intensities of Zeeman-split absorption lines in ions accelerating away from the surface of stars, illuminated by continuum radiation from the photosphere below, frequently exhibits similar asymmetries [3,4]. With the model described here, such measurements of AOP could provide additional information about the plasma conditions in the atmospheres of those stars. Additionally, AOP with an uncalibrated LIF system can provide a non-invasive measurement of the total ion collision frequency, and therefore the plasma density, in highly ionized plasmas.

Chapter 5 References

[1] R. A. Stern and J. A. Johnson III, Phys. Rev. Lett. **34**, 1548 (1975).

[2] G. D. Severn, D. A. Edrich and R. McWilliams, Rev. Sci. Instrum. **69**, 10 (1998).

[3] M. Sigwarth, Astrophys. J. **563**, 1031 (2001).

[4] H. Lin, M. Penn, and S. Tomczyk, Astrophys. J. **541**, 83 (2000).

[5] H. Y. Carr, E. M. Purcell, Phys Rev. **94**, 630 (1954).

[6] S. A. Cohen, N. S. Siefert, S. Stange, R. F. Boivin, E. E. Scime, and F. M. Levinton, Phys. Plasmas, **10**, 2593 (2003)

[7] H. Batelaan, T.J. Gay, and J.J. Schwendiman, Phys. Rev. Lett. **79**, 4517 (1997).

[8] G. A. Gallup, H. Batelaan, and T.J. Gay, Phys. Rev. Lett. **86**, 4508 (2001).

[9] V. F. Weisskopf, Ann. d. Physik **9**, 23 (1931).

[10] H. W. Babcock, Astrophys. J. **118**, 387 (1953).

[11] M. J. Geockner and J. Goree, J. Vac. Sci. Technol. A **7**, 977 (1989).

[12] F. Skiff and J. J. Curry, Rev. Sci. Instrum. **66**, 629 (1995).

[13] A. V. Phelps, J. Phys. Chem. Ref. Data, **20**, 557 (1991).

Chapter 6: Resistive Drift Alfvén Wave

Although higher plasma densities correlated with operation of helicon plasma sources near the lower hybrid frequency have been reported by a number of groups [1, 2, 3, 4, 5, 6], there is still considerable debate about the role played by plasma instabilities in limiting plasma density in strongly magnetized helicon sources [7, 8, 9, 10]. *Light et al.* [7] suggested that low frequency electrostatic instabilities increase the loss rate of plasma at high magnetic field strengths and thus reduce plasma density. In their low β ($\beta = 8\pi nkT/B^2$) plasma experiments, the electrostatic resistive drift and Kelvin-Helmholtz instabilities were suggested as the source of the observed low frequency turbulence. Recently, in a relatively high β ($1 >> \beta > m_e/M_i$) helicon plasma, *Schröder et al.*[11] identified the drift wave by using an azimuthal Langmuir probe array in another helicon plasma. The magnetic field strength was found to be the primary trigger for destabilization of the wave. Since their β was less than ν_e/Ω_e (where ν_e is electron collision frequency and Ω_e is the electron cyclotron frequency), only electrostatic waves was considered in their analysis. In plasmas with $\beta > \nu_e/\Omega_e$, the resistive drift instability becomes an electromagnetic instability, i.e. the resistive drift Alfvén instability [12].

In this chapter, we present three dimensional electromagnetic wave frequency and amplitude measurements of low frequency instabilities observed in the expansion region of a strongly magnetized, current-free, helicon plasma. Radial plasma density profiles are measured by rf-compensated Langmuir probes in the expansion region and in the helicon plasma source. The effects of helicon plasma source magnetic field strength, expansion region magnetic field strength, and neutral pressure are investigated. A theoretical model of the resistive drift Alfvén instability, developed by *Mikhailovskii* [12], is shown to accurately predict the measured wave frequency dependence on magnetic field strength.

The experiment was conducted in HELIX-LEIA system. A three-axis magnetic sense coil array, placed in LEIA at z = 272 cm, is used to measure the spectrum and amplitude of electromagnetic fluctuations over the frequency range 1 to 100 kHz. Each of the three magnetic sense coils is made from 300 turns of 40 HML gauge, coated copper wire wound on a 7 mm long, 3 mm diameter boron nitride reel. All three components of electromagnetic fluctuations in LEIA were measured as a function of both HELIX and LEIA magnetic field strength and neutral pressure. The spatial distribution of wave amplitude was investigated by scanning the probe along the radial direction. Complete details of the probe geometry and design can be found in Ref. [13] or Chapter 2 of this dissertation.

For plasmas with $1 >> \beta > \nu_e/\Omega_e$, coupling between typically electrostatic drift waves and hydrodynamic Alfvén waves can result in the growth of the unstable coupled drift-Alfvén mode. Early experiments identified the lower-frequency drift branch in current-free collisional plasmas [14] and later experiments observed the higher-frequency Alfvén branch in high-density, collisional plasmas with an externally imposed DC current [15]. This electromagnetic instability is a transverse wave and the dispersion relation can be obtained from a two-fluid plasma model.

Following the method of *Mikhailovskii*, we ignore the temperature gradient and temperature perturbations and start from the electron momentum equation:

$$m_e n \frac{d\mathbf{V}}{dt} = -\nabla p + e_e n(\mathbf{E} + \frac{1}{c}\mathbf{V}\times\mathbf{B}) + \mathbf{R}\,, \tag{6-1}$$

where m_e is the electron mass, n is the electron density, p is the electron thermal pressure, E is the electric field, V is the electron speed, B is the magnetic field, and R is the frictional, i.e., resistive force. The first order perturbation of E is given by $\tilde{E} = -\nabla\tilde{\phi} - (1/c)\,\partial\tilde{A}/\partial t$ in the Coulomb gauge; where ϕ and A are the scalar (electrostatic) and vector potentials. The first order perturbation of R in the z direction (the equilibrium magnetic field direction) is $\tilde{R}_{ze} = -\nu_e n_0 m_e \tilde{V}_{ze}$, where ν_e is the electron collision frequency with ions. When $A_z \neq 0$ and $A_\perp = 0$, the first order perturbation equation of Eq. (6-1) along z is:

$$e_e(-ik_z\tilde{\phi} + {i\omega A_z}/{c}) + {e_e V_{ne}\tilde{B}_x}/{c} - ik_z\,{\tilde{p}_e}/{n_0} - \nu_e m_e \tilde{V}_{ze} = 0 \tag{6-2}$$

where $V_{ne} = \dfrac{ck_B T_e}{e_e B}\dfrac{\partial n}{n\partial x}$.

Combining the first order Maxwell's equation,

$$k_\perp^2 \tilde{A}_z = (4\pi / c) e_e n_0 \tilde{V}_{ze} \tag{6-3}$$

the electron continuity equation,

$$-i\omega\tilde{n}_e + c(\tilde{E}_y / B_0)\partial n_0 / \partial x + i n_0 k_z \tilde{V}_{ze} = 0 \tag{6-4}$$

the ion continuity equation,

$$-i\omega n_i + \frac{cE_y}{B_0}\frac{\partial n_0}{\partial x} + ik_y V_{iy} n_0 = 0 \tag{6-5}$$

and noting that the V_{iy} component, which arises as a result of ion inertia and leads to the phase difference between density and potential fluctuations, is

$$V_{iy} = \frac{M_i c}{eB}\dot{V}_{ix} = \frac{M_i c^2}{eB^2}\frac{\partial E_y}{\partial t} = -i\frac{\omega}{\Omega_i}\frac{cE_y}{B}\ , \tag{6-6}$$

the dispersion relationship for electromagnetic drift waves is obtained

$$(\omega - \omega_{ne})(\omega^2 + \omega\omega_{ne} - k_z^2 C_A^2) - z_i C_A^2 k_z^2 \omega(1 - i\omega\nu_e M_e / k_z^2 T_e) = 0\ ; \tag{6-7}$$

where $z_i = k_y^2 k_B T_i \big/ M_i \Omega_i^2$, $\omega_{ne} = \left(ck_y k_B T_e \big/ e_e B\right)\left(\partial n \big/ n\partial x\right)$, and C_A is the Alfvén speed. In the $z_i \to 0$ approximation, Eq. (6-7) has three solutions: $\omega_{1,2} = -\,|\,\omega_{ne}\,| \pm [(\omega_{ne}/2)^2 + (k_z c_A)^2]^{1/2}$ and $\omega_3 = \omega_{ne}$. In the limit of $z_i \to 0$, i.e., ignoring finite Larmor radius effects, Nishida and Ishii's derivation [14] yields the same roots as Eq. (6-7). According to their analysis, the ω_1 root corresponds to the higher frequency branch (as well as the negative ω_2 root), which is the Alfvén wave modified by ion drift motion. A moderate axial current is needed to drive this branch [15,16]. Thus, in our current-less plasma, only the lower frequency branch with $\omega_3 = \omega_{ne}$ is expected. This root frequency is the same as that which is obtained from the electrostatic drift wave dispersion relationship: $(\omega - \omega_{ne}) - z_i\omega(1 - i\omega\nu_e M_e / k_z^2 T_e) = 0$. The electromagnetic nature of this solution can be best understood by considering the amplitude of the magnetic fluctuations. Using Eqs. (6-2), (6-3), and (6-4) to eliminate $\tilde{\phi}$, we obtain

$$\left(\frac{\omega}{V_{ne}}+k_z\right)\frac{\tilde{n}}{n}=\frac{\nu_e}{\Omega_e}\frac{1}{\beta}k_y\frac{\tilde{B}_x}{B_o}-i\left(\frac{\partial n}{n\partial x}+\frac{\Omega_i\omega}{k_xV_{Ti}^2}+2\frac{k_z}{\beta}\frac{\partial n}{n\partial x}\right)k_y\frac{\tilde{B}_x}{B_o} \tag{6-8}$$

The real part of Eq. (6-8) yields

$$\frac{\tilde{B}_x}{B_o}=\beta\frac{\Omega_e}{\nu_e}\left(\frac{\operatorname{Re}\omega}{\omega_{ne}}+\frac{k_z}{k_y}\right)\frac{\tilde{n}}{n}. \tag{6-9}$$

Thus, when $\omega=\omega_{ne}$ and $k_z/k_y\to 0$, which is typical of drift waves, we obtain $\tilde{B}_x/B_o=\beta\,\Omega_e\tilde{n}/\nu_e n$. Therefore, if $\beta<\nu_e/\Omega_e$, magnetic fluctuations can be ignored and the wave is essentially electrostatic. If $\beta>\nu_e/\Omega_e$, the electromagnetic nature of the fluctuations must be considered. Specifically, the first order correction to the wave frequency is different in the electromagnetic case. For the essentially electrostatic case, the wave frequency is $\omega=\omega_{ne}+z_i\omega_{ne}$ and for the electromagnetic case the wave frequency is

$$\omega=\omega_{ne}+z_i\omega_{ne}\left(\frac{k_z^2C_A^2}{2\omega_{ne}^2-k_z^2C_A^2}\right). \tag{6-10}$$

The growth rates of the two cases also differ, for the electrostatic case the wave growth rate is

$$\gamma=z_i\nu_e\frac{\omega_{ne}^2}{k_z^2V_{te}^2} \tag{6-11}$$

(note the lack of dependence on plasma β; V_{te} is the electron thermal speed). For the electromagnetic case, the wave growth rate is

$$\gamma = z_i \nu_e \frac{1}{\beta} \frac{M_e}{M_i} \left(\frac{\omega_{ne}^2}{2\omega_{ne}^2 - k_z^2 C_A^2} \right) \propto z_i \nu_e \frac{1}{\beta} \frac{M_e}{M_i} . \qquad (6\text{-}12)$$

Since ω_{ne} is equal to the electron diamagnetic frequency, the wave frequency should decrease with increasing magnetic field strength. From the dispersion relationship, the destabilizing parameters (those that lead to wave growth) for this wave can be identified as the electron-ion collision frequency and magnetic field strength (for those plasmas in which β decreases with increasing magnetic field strength).

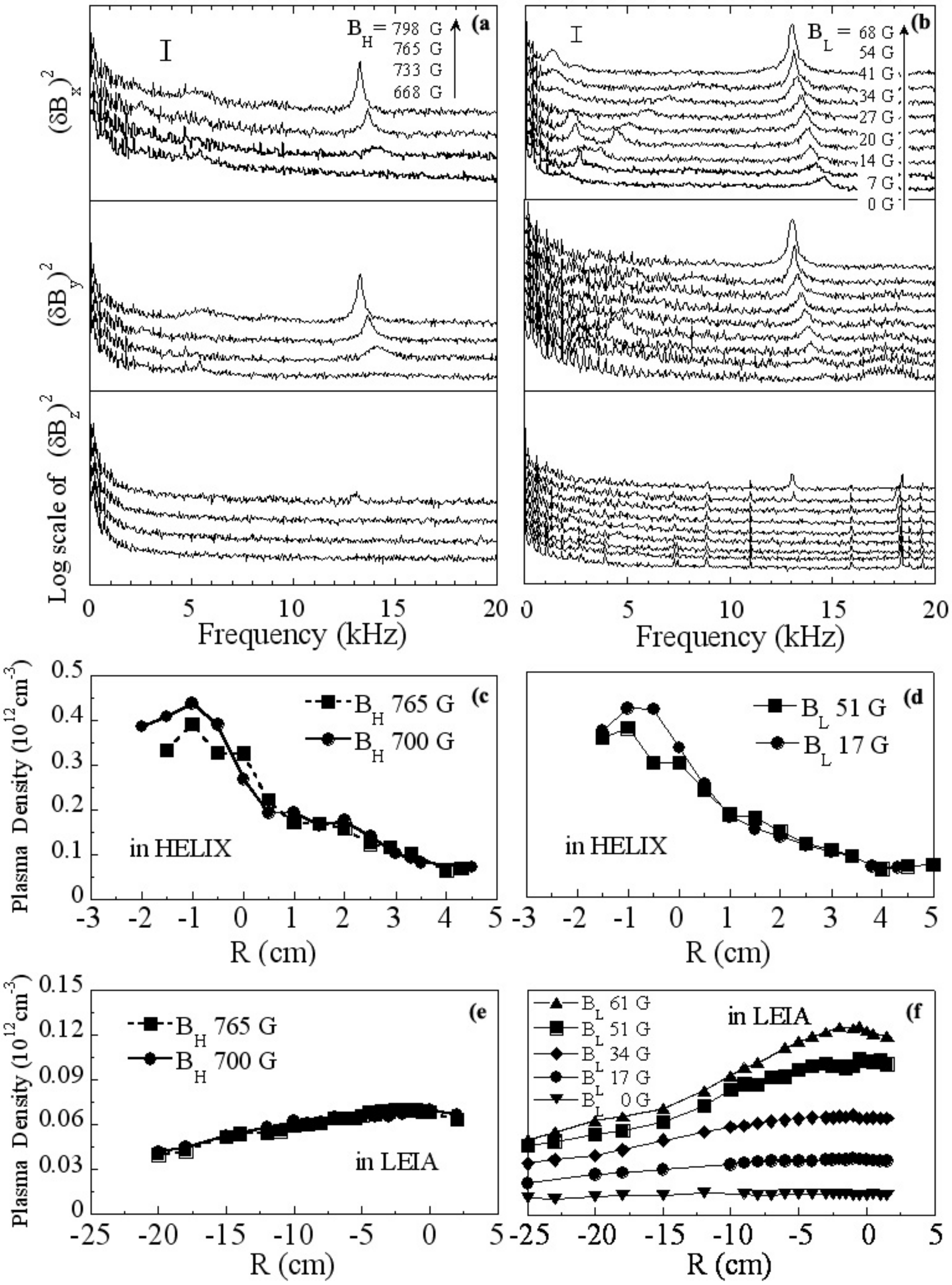

Figure 6-1. For neutral pressure of 1.6 mTorr and rf power of 700 Watts, power spectrum of three components of magnetic fluctuations at z = 272 cm and r = 0 cm (a) vs. the B_H with B_L = 34 G and (b) vs. the LEIA magnetic field strength (B_L) with B_H = 733 G. For neutral pressure of 1.7 mTorr and rf power of 720 Watts, the radial plasma density profile measurements in HELIX (c) vs. B_H (z = 126 cm) with B_L = 34 G , and (d) versus B_L (z = 126 cm) with B_H = 733 G, and in LEIA (e) vs. B_H (z = 272 cm) with B_L = 34 G, and (f) vs. B_L (z = 272 cm) with B_H = 733 G. The length of the 'I' in (a) and (b) corresponds to a factor of 10 increase in the magnitude of $(\delta B/B)^2$

Shown in Fig. 6-1a and 6-1b are power spectra for electromagnetic fluctuations measured in LEIA in all three directions as a function HELIX (source) and LEIA (expansion region) magnetic field strength. Shown in Figs. 6-1c, 6-1d, 6-1e, and 6-1f are the density profiles in HELIX (at z = 126 cm) and LEIA (at z = 272 cm) for scans of HELIX and LEIA magnetic field strength.

The focus of this chapter is the peaks in Figs. 6-1a and 1b that appear around 13 kHz. The waves are clearly transverse with $B_y \approx B_x >> B_z$, the wave frequency decreases with increasing magnetic field strength, and the wave amplitude increases with increasing magnetic field strength. Note that although the plasma density increases with increasing magnetic field strength, the overall plasma β of HELIX decreases with increasing magnetic field strength. The wave frequency is less than the ion cyclotron frequency in HELIX (30 kHz) and larger than the ion cyclotron frequency in LEIA (1.3 kHz).

Before the characteristics of the 13 kHz peaks can be compared to the predictions of any dispersion relation, the location of wave excitation must first be determined. If the waves are produced entirely in plasma source, then the wave frequency should be completely independent of the LEIA magnetic field strength since neither the plasma density profile or magnetic field strength in HELIX depend on the LEIA magnetic field strength in any significant manner (even at z = 126 cm, very close the junction between the source and LEIA, see for example Fig. 6-1d). If the waves are produced in LEIA and the waves are resistive drift-Alfvén waves, then the strong dependence on LEIA magnetic field strength of the LEIA density gradient (see Fig. 6-1f) should make the wave frequency and amplitude dependence of the 13 kHz peaks on the LEIA magnetic field strength much larger than the HELIX magnetic field strength dependence (which has little effect on the LEIA density gradient or LEIA magnetic field strength, see for example Fig. 6-1e). Since neither of these expectations is realized in the measurements, we hypothesize that the 13 kHz wave is excited in the region between LEIA and HELIX, where the magnetic field is decreasing along z and plasma is expanding into the 2m-diameter LEIA chamber from the 15 cm-diameter HELIX chamber. Note, that because $k_z\lambda_B > 1$ (λ_B is the scale length of the magnetic field gradient) in our experiments, we ignored the parallel mirror force $-\mu\, \partial B_z/\partial z$ in the formulation of Eq. (6-1). If we had retained the mirror force term, Eq. (6-2) would still be the same as the electron μ is constant [17] and no fluctuation of B_z are observed in the experiments, *i.e.*, based on the measurements the first order term $-\mu\,\partial B_z/\partial z$ is zero.

Since the 13 kHz peak shifts down in frequency approximately 1 kHz for both the HELIX and LEIA increasing magnetic field strength scans, the wave has a drift-wave-like and not a cyclotron-like dependence on the magnetic field strength. Since an 84 Gauss magnetic field increase in HELIX and a 49 Gauss magnetic field increase in LEIA both yield the same 1 kHz downshift in the instability frequency (Fig. 6-1), it is likely that the actual magnetic field strength change at the point of wave excitation is similar for both scans. According to numerical calculations of the axial magnetic field profile in the combined HELIX-LEIA system, at z =156 cm (just past the end of the helicon source), the change in the total magnetic field is 35 Gauss for both the LEIA and the HELIX magnetic field scans. Because the resistive drift wave occurs when the phase speed of the Alfvén wave equals the phase speed of the density-gradient driven drift wave [18], we hypothesis the z = 156 cm is where these two wave phase speeds are similar in magnitude.

Based on the LEIA electron temperature of 6.5 eV and HELIX electron temperature of 10.0 eV (measured at z = 126 cm and z = 272 cm), we estimate the electron temperatures to be 7.0 ± 0.5 eV, at z = 156 cm. At the same location, the HELIX plasma cross sectional area has expanded roughly a factor of two as the plasma follows the expanding magnetic field. Estimating that the plasma density at z = 156 cm decreases by a factor of two from in the source (based on the measured expansion of the magnetic field flux tubes), the plasma conditions at z = 156 cm yield $\beta \approx 5\times10^{-4}$, which is 50 times larger than (m_e/M_i) and 10 times larger than (ν_e/Ω_e). Density measurements in HELIX and particle flux conservation yield an estimated plasma density of $2\times10^{11}\text{cm}^{-3}$ and a normalized density gradient of 1/(10 ± 1) cm^{-1} (the average of the density gradients measured in HELIX and LEIA) at the same location. k_z measured downstream in LEIA with another magnetic field fluctuation probe at $z = 400$ cm is roughly 0.05 ± 0.01 cm^{-1}, yielding a phase speed of $1.5 \sim 2.5\times10^4$ m/s which about two times larger than the ion flow speed (10^4 m/s) and fifty times smaller than the electron thermal speed (10^6 m/s). In other words, wave-particle interactions should not play a significant role in the dynamics of the observed wave and the conditions for excitation of the resistive drift Alfvén wave are satisfied.

Shown in Fig. 6-2 are the measured wave frequencies (solid circles) and fluctuation amplitudes ($\tilde{B}$) (open squares) extracted from the measurements shown in Fig 3b. versus the magnetic field strength at $z = 156$ cm. As predicted by Eq. (6-7) for the lower branch of resistive drift Alfvén wave, the wave frequency should proportional to $1/B$. The solid line in Fig. 6-2 is linear fit to α / B and α is a fitting parameter. Since the waves occurred in steady state and the initiation of the wave was difficult to control, we could not measure the real growth rate of the wave. Assuming the growth time (τ) is same for all the measurements in Fig. 3b, the wave amplitude should be proportional to $\exp(\gamma\tau) \sim \exp(z_i \nu_e m_e \tau / \beta M_i)$. In these experiments, the plasma densities in HELIX, and hence the plasma densities at $z = 156$ cm, barely changed during the LEIA magnetic field scan. Thus, β is proportional to the $1/B^2$. The dotted line in Fig. 6-2 is a fit to wave amplitude data by the equation $\alpha_1 \exp(\alpha_2 B^2)$. The scaling of the wave amplitude and wave frequency with magnetic field strength are both in excellent agreement with the model.

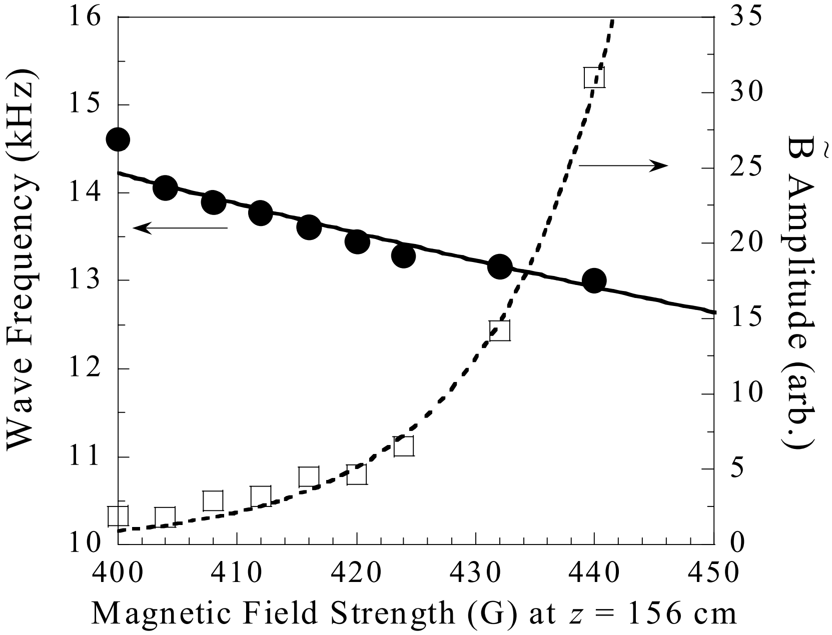

Figure 6-2. Measured wave frequency (solid circles), wave amplitude (open squares), predicted function of wave frequency (solid line), and wave amplitude (dotted line) versus magnetic field strength at $z = 156$ cm.

Since the resistive-drift Alfvén wave is driven by the presence of a density gradient, wave excitation should be localized to those plasma regions with significant density gradients. Once the waves are created, they can propagate out of the region of excitation while retaining many of their original characteristics, e.g., wave frequency. *Nishida et al.* [14] reported that the amplitude of magnetic fluctuations of the coupled mode of the collisional drift and Alfvén wave, increased towards the plasma center in his experiments. Consistent with localization to the region of maximum density gradient, the wave amplitude in LEIA (at z = 272 cm) decreases with increasing radius and then disappears at r = -15 cm as shown in Fig. 6-3.

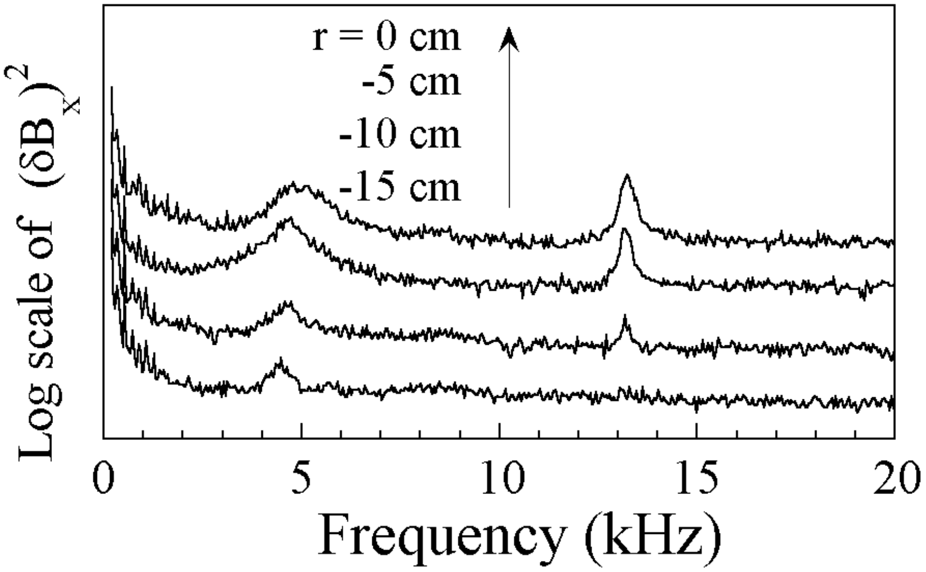

Figure 6-3. B_x fluctuation power spectrum measurements along r direction at z = 272 cm for a rf power of 700 W, B_H = 798 G, B_L = 34 G, and neutral pressure of 1.8 mTorr.

Fundamentally, the drift instability is caused by a phase difference between potential fluctuations and density fluctuations. This phase shift is due to perpendicular charge separation. If the parallel electron speed in a plasma is large enough, perpendicular charge separation can be neutralized and the drift instability suppressed [19]. Previously, we reported that a strong parallel electric field develops in the expansion region of a helicon plasma source if the neutral pressure drops below a critical value [20]. Thus, it could be included in Eq. (6-2) as an effective enhancement of the resistive term, ν_e. The somewhat counter-intuitive increased effective resistivity at lower neutral pressure should yield a larger growth rate, and hence a larger wave amplitude, because the wave growth rate is proportional to the plasma resistivity. This hypothesis is confirmed by the measurement of magnetic fluctuation power spectra versus neutral pressure shown in Fig. 6-4. In addition to the increase in effective parallel resistivity, lower neutral pressures also reduce the ion-neutral collision rate in the plasma (important as neutral damping should not be ignored in a partially ionized plasma). Since the charge separation is due to V_{iy}, a ion-neutral collision term should be added in Eq. (6-6) so that $V_{iy} = \left(M_i c/eB\right)(\dot{V}_{ix} + \nu_{in} V_{ix})$. To estimate the damping due to neutral collisions, we set $\nu_e = 0$ in Eq. (6-2), then combine Eq. (6-2) through Eq. (6-6) to obtain $\omega - \omega_{ne} = -z_i(\omega + i\nu_{in})$ and a growth rate of $\gamma = -z_i \nu_{ni}/\left(1+z_i\right) \sim -z_i \nu_{ni}$. Thus, as expected and as seen in the measurements, lower neutral pressures should lead to larger wave amplitudes. Note that although the data shown in Fig. 6-4 were obtained in LEIA and the neutral pressure in LEIA is typically 10 times smaller than the neutral pressure in HELIX, each spectrum is labeled with the neutral pressure in HELIX for consistency with the pressure values reported earlier this manuscript.

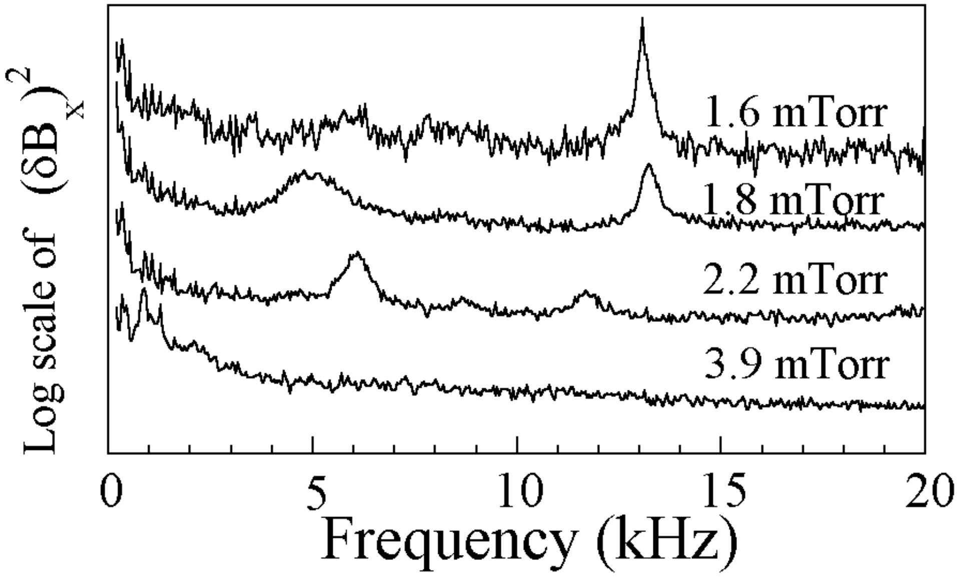

Figure 6-4. B_x fluctuation power spectrum measurements as a function of neutral pressure at z = 272 cm and r = 0 cm for a rf power of 700 W, B_H = 798 G, B_L = 34 G.

In summary, we have presented strong low frequency electromagnetic waves in a current free helicon plasma that appear in low neutral pressure and are localized to the region of the plasma with the largest density gradient. The wave amplitude grows rapidly with increasing magnetic field strength (and the wave frequency downshifts with increasing magnetic field strength), consistent with previous helicon source experiments. Because the waves arise in a plasma that satisfies the $1 >> \beta > \nu_e / \Omega_e > m_e / M_i$ requirements for growth of resistive-drift Alfvén waves, we have compared the measured wave frequencies to expectations for resistive-drift Alfvén waves. The observed wave is a transverse electromagnetic wave and the wave frequency is consistent with expectations for a resistive-drift Alfvén wave. With increasing magnetic field strength, the wave amplitude increases and eventually the plasma becomes unstable. As suggested by other research groups, it is possible that this low frequency wave could be responsible for reduced plasma confinement in helicon sources at large magnetic field strengths.

Chapter 6 References

[1] R. Boswell, Plasma Phys. Controlled Fusion **26**, 1147 (1984)

[2] Y. Sakawa, T. Takino, and T. Shoji, Phys. Plasmas **6**, 4759 (1999)

[3] S. Cho, Phys. Plasmas **7**, 417 (2000)

[4] J. L. Kline, E. E. Scime, R. F. Boivin, A. M. Keesee, X. Sun, and V. S. Mikhailenko, Phys. Rev. Lett. **88**, 1950021 (2002)

[5] M. Balkey, R. Boivin, P. Keiter, J. Kline, and E. E. Scime, Plasma Source Sci. Technol. **10**, 284 (2001)

[6] J. G. Kwak et al., Phys. Plasmas **4**, 1463 (1997)

[7] M. Light, F. F. Chen and P. L. Colestock, Phys. Plasmas **8**, 4675 (2001); M. Light, C. Chen, P.L. Colestock, Plasma Source Sci. Technol. **11**, 273 (2002).

[8] G. R. Tynan, M.J. Burin, C. Holland, G. Antar, N. Crocker, P. H. Diamond, Phys. Plasmas, **11**, 5195 (2004)

[9] B. P. Cluggish, F. A. Anderegg, R. L. Freeman, J. Gilleland, T. J. Hilsabeck, R. C. Isler, W. D. Lee, A. A. Litvak, R. L. Miller, T. Ohkawa, S. Putvinski, K. R. Umstadter, and D. L. Winslow, Phys. Plasmas, **12**, 057101 (2005).

[10] M. D. Carter, F. W. Baity, Jr., G. C. Barber, R. H. Goulding, Y. Mori, D. O. Sparks, K. F. White, E. F. Jaeger, F. R. Chang-Diaz, J. P. Squire, Phys. Plasmas **9**, 5097 (2002).

[11] C. Schröder, O. Grulke, and T. Klinger, Phys. Plasmas, **12**, 042103 (2005)

[12] A.B. Mikhailvskii, Electromagnetic Instabilities in an Inhomogeneous Plasma (IOP Publishing Ltd. 1992)

[13] C. Biloiu, E. E. Scime, and X. Sun, Rev. Sci. Instrum. **75**, 4296 (2004)

[14] Y. Nishida and K. Ishii, Phys. Rev. Lett. **33**, 352 (1974).

[15] J. T. Tang, N. C. Luhmann, Y. Nishida and K. Ishi, Phys. Rev. Lett. **34**, 70 (1975)

[16] R. Hatakeyama, M. Inutake, and T. Akitsu, Phys. Rev. Lett. **47**, 183 (1981)

[17] F. F. Chen, Introduction to plasma physics and controlled fusion (Plenum Press, New York 1984)

[18] J. T. Tang and N. C. Luhmann, Jr., Phys. Fluids, **19**, 1935 (1976)

[19] F. F. Chen, Phys. Fluids, **8**, 912 (1965)

[20] X. Sun, C. Biloiu, R. Hardin, and E. E. Scime, Plasma Sources Sci. and Tech. **13**, 359 (2004).

Chapter 7: Summary and Discussion

The parallel ion flow speed measurements in two different helicon plasma sources with different magnetic field geometries presented in this work demonstrate the existence of spontaneously forming double layers in the magnetic field gradient region of freely expanding helicon plasmas. The free and trapped ion populations seen in the ivdf measurements by non-perturbing LIF in MNX and HELIX-LEIA are consistent with numerical predictions of double layer development in expanding helicon plasmas. The experimental and numerical results support the hypothesis that a spatially localized electron loss process plays a critical role in double layer formation, i.e., the DL forms if the scale length of the density gradient (which can result from the presence of a strong magnetic field gradient) is smaller than the ion-neutral collision length.

Evidence for DL formation by other processes was presented in discussion of the aperture experiments in MNX. Strong DLs ($\sim 6kT_e$) initiated by an aperture placed in a plasma source immersed in a uniform magnetic field were observed in the MNX experiments. A possible explanation for such strong, $\sim 6kT_e$, potential drops is the presence of energetic electrons that in the plasma. Some indirect evidence for the existence of isotropic energetic electrons is given by the observed changes in floating potential and DL strength downstream resulting from changes in the mirror ratio, equivalent to changing the energetic electron flux into expansion region.

There were also some interesting observations not reported in the more formal portion of this dissertation because of a lack of definitive evidence. For example, a negative potential dip on the low potential side of DL in the HELIX-LEIA experiments appeared routinely in both LIF and plasma potential measurements. Such observations would be consistent with expectations for potential structures arising from ion-acoustic shocks [1,2]. Reversed flow of trapped ions (towards the DL), which could be due to such a negative potential dip, were observed in MNX experiments. Some questions raised by these observations include: Are the observations indicative of DLs continuing to evolve? Do the observations suggest that ion holes appear in the ivdf and that the holes initiate the formation of the DL? Some of the questions will be answered through future time resolved LIF measurements of DL evolution. Although recently completed time resolved

LIF measurements reveal that the DL forms within the first 3 ms of the discharge, the details of the DL evolution in those 3 ms have yet to be determined [3].

Another fundamental question is how the plasmas in expansion region are produced. LIF measurements indicate that the downstream plasmas are not entirely the remains of plasma expanding out of the plasma source. The measured LIF amplitudes of trapped and free ions in MNX as a function of neutral pressure and axial position suggest that the downstream plasma might be produced locally by electron-neutral collisions. The MNX experiment, with its metal aperture plate that separates the source from expansion region, is very different that the open-ended HELIX-LEIA experiment. In HELIX-LEIA, fast or slow waves could propagate along the field lines into the expansion chamber and ionize the neutrals through wave-wave or/and wave-particles processes. Additionally, charge-exchange or other momentum transfer processes could play a role in ion production downstream of the DL. Caution in using LIF data to investigate momentum charge exchange processes is warranted because if the expanding ions slow down through charge exchange collisions and then form slow ions, each collision could depopulate the metastable ion state and make the decelerating ions 'invisible' in LIF measurements. Thus, the absence of LIF measurements of decelerating ions in the expansion region does not rule out the possible importance of such processes. However, it is worth noting that the retarding field energy analyzer measurements in Chi-Kung did not show any evidence for a population of decelerating ions. Considering the ratio of ion mean-free-path to the length of expansion chamber, charge exchange processes might be important in MNX and HELIX-LEIA plasmas, but perhaps not in Chi-Kung.

An important consequence of charge-exchange processes is the creation of fast neutral beams, which are of particular importance for plasma thruster applications. Through time resolved LIF measurements, it might be possible to determine if charge exchange processes are responsible for creating the trapped ions. In principle, the amplitude of free ions would grow with time and then decrease due to collisions (assuming the collision time is larger than the thermalization time and ion transit time through the expansion region). In this scenario, the LIF amplitude of the trapped ions should increase as the free ion population decreases. In recent time-resolved measurements (~ 5ms resolution), we observed the amplitudes of free and trapped ions increasing simultaneously. Thus, the charge-exchange processes do not appear to dominate the plasma production process in the expansion region. However, a definitive conclusion awaits improvement in the time resolution of the pulsed source LIF measurements and corroboration from other diagnostics. Another focus of future plasma thruster relevant work should be to explore methods of increasing the outflow ion speed to super-Alfvénic velocities and measuring the neutral flow speed by LIF. At super-Alfvénic velocities plasma detachment should occur [4]. Momentum coupling to neutrals would also provide a means of plasma detachment. In either case, controlled plasma detachment is critical to successful operation of helicon sources as plasma thrusters.

A serendipitous result reported in this dissertation was the observation of explanation of asymmetric optical pumping (described and modeled in Chapter V). The AOP effect occurs if the changing Doppler frequency shift can compensate for the changing Zeeman frequency shift when ions accelerate in a region with magnetic field gradient. Because the frequency shift of $\sigma+$ and $\sigma-$ transitions are in opposite directions, the frequency shifts of only one transition ($\sigma-$ in our experiments) cancel. Thus, ions in the $\sigma-$ transition initial state remain resonant with the laser beam while accelerating. The continual pumping of the $\sigma-$ transition upstream of the observation point results in a smaller $\sigma-$ LIF signal at the measurement location. Thus, the LIF amplitudes are different for the $\sigma-$ and $\sigma+$ transitions. To the best of our knowledge, this phenomenon has never been previously reported. The AOP may also provide an explanation for abnormal asymmetric stokes V profile observations, one of the mysteries in stellar magnetic field measurements. Observation of AOP effects in other helicon source plasmas awaits future work.

Creating of strong DLs requires operational of helicon sources at the lowest limit of gas pressure, ~1.5mTorr. Below this pressure, and at high magnetic field strengths, the plasma becomes unstable. Electromagnetic fluctuation measurements at high magnetic field and low pressure suggest that resistive drift Alfvén waves are excited in the expansion region of the helicon plasma. However, the electrostatic drift instability, which could also exist in the source, has not been seriously investigated. Future wave studies should measure the density and potential fluctuations, azimuthal mode number of the waves, and the phase shift between the density and potential fluctuations.

In summary, plasma expansion in a magnetic field gradient involves a wide range of interesting, and not fully understood, plasma phenomena. Despite the experimental challenges, three-dimensional flow speed measurements in a plasma cross-section at different axial locations throughout a DL structure would be a challenging and scientifically productive undertaking, however, that is work for future researchers.

Chapter 7 References

[1] M. K. Hudson, W. Lotko, I. Roth, E. Witt, J. Geophys. Res. **88**, 9161 (1983)

[2] N. Hershkowitz, Space Sci. Rev. **41**, 351 (1985)

[3]C. Biloiu**,** X. Sun, E. Choueri, E. E. Scime, *et al.*, *Plasma Sources Sci. Technol.* **14**, 766 (2005)

[4] A. V. Arefiev, and B. N. Breizman, Phys. Plasmas **11**, 2942 (2004)

Appendix: Matlab code for the calculation of Asymmetric Optical Pumping

```
%  This code calculates the ratio of LIF intensity of the different sigma
%  state groups for diode laser illumination of argon ions assuming that
%  the metastable density of the initial state is much greater than then
%  density of the upper state and stimulated emission down to the initial
%  state can be ignored. In other words, this code only calculates the
%  ratio of pumping rates out of the initial state by the laser.
%  Earl Scime                                        1-7-2004
%  Modifications:    Xuan Sun                        1-15-2004
%   the frequency of sigma+ transition shift higher,
%   set the direction of z axis is laser direction, so velocity is negative
%   set the zero point of z axis at Z=2.3 cm , so Z=3.3 cm is -1 cm
%   velocity profile linear approximation V(x)=Ax+D 14.7eVat z=3.3 13 eV at z=2.3
%   so A>0, D<0
clear;

% Spacing of the sigma lines from the center of the rest frame line in
% GHz/kG
%warning:weights should be normalized
alpha=[1.26 1.44 1.63 1.82 2.01 2.19];   %from Boivin PLP 50
weights=[21/58.0   15/58.0   12/58.0   6/58.0     3/58.0     1/58.0];  %from Boivin PLP 50



lightspeed=2.9979E8;
line_freq=lightspeed/(668.43E-9)/1.0E9;

%create arrays
Nozzle_field=zeros(1,10);
Pumping_ratio=zeros(1,10);
```

```
flow_speed=zeros(1,10);
pre_coll_dis=zeros(1,10);
Signal_ratio = zeros (1,10);
Pumping_ratio(1)=1;
Nozzle_field(1)=0;

flow_speed(1)=0;

alpha_D=1.0/.092495;  %in units of GHz^2/eV
T=0.2;  %estimate of MNX Ti
B01=8.037E12; %Einstein coeffient for Argon 668
I=15000/pi/1.6;   %laser intensity W/m^2, 15mw/pi1mm^2
xo = 0.029;
r = 0.03;
%scan through some parameter
for j=1:20

%velocity profile linear approximation V(x)=Ax+D 17.7eVat Z=6.3(z=-1)
%the velocity function is from the experimetn data fitting, V=11.7 + 0.85*x
   D=sqrt(2.*11.7/938E6/40)*lightspeed;
   A=(-D+sqrt(2.*12.55./938E6/40)*lightspeed)/0.01;  %velocity slope in (m/s)/m
   %D=D*(j)*.1;
   %A=A*(j)*.1;
%magnetic field profile linear approximation (positive direction is back
%towards source)  B(x)=Bx+C

   Bscaling=(j-1)/7.2;
   C = Bscaling;
%B=Bscaling*(500/0.006/1000);   %field change in kG/m the scale 0.37/cm  is  based on
                  %LIF measurements
```

```
%define "pre-illumination" time for integration as average ion speed at
%point of measurement times ion-electron collision time (assuming such
%collisions "reset" the ion quantum state distribution.
   n = 7.5E10; p = 0.7; Te = 6; %p is the neutral pressure
%ion-ion collisions
   coll_freq1=(4.8E-8)*10*n/sqrt(40)/sqrt(T^3);
%ion-neutral collsion 3.2e13 is the density per mTorr, 8.5e-15 is the collision cross
                %section
%*100 to convert it to cm/s
  coll_freq2 = p*(3.2E13*8.5E-15)*abs(D+A*xo)*100;
   coll_freq = coll_freq1 + coll_freq2;
   t_coll=1.0/coll_freq; %estimated using the ion-ion collision freq for a 1E12 density
                %plasma
  delta_t = t_coll/200;
  z(1) = xo;
  for m=1:200
     z(m+1) = z(m) - (A*z(m)+D)*delta_t;
  end
  %delta_x=abs(D*t_ie);   %D is the ion speed at the measurement location
  delta_x = z(1) - z(m+1);
  x = linspace(xo-delta_x,xo,200);

  %Bfield = B.*x + C;
  Bfield =  C./(1+(x./r).^2).^1.5; % Using formular of B produced by loop current
                %instead of linear equation
  Velocity = A.*x +D;

  %assume laser tuned to peak of largest signma lines for measurement in GHz
  laser_plus = (line_freq+alpha(1)*C)*(1.0-D/lightspeed);
  laser_minus = (line_freq-alpha(1)*C)*(1.0-D/lightspeed);
  initialfreq = (line_freq-alpha(6)*C)*(1.0-D/lightspeed);
```

```
Rplus_sum=0.0;
Rminus_sum=0.0;

for m=1:200
   % determine laser scan range
   laser_freq(m) = initialfreq -10.0 + 30.0/200.0*m;%(finalfreq-
               %initialfreq+7.0)/200.0*m;
   laser_plus = laser_freq(m);
   laser_minus = laser_freq(m);




   %integrate for each of the sigma lines
   for i=1:6
       % integrate function from 0 to delta_x
         Rplus(i)=0;Rminus(i)=0;
          plus = (laser_plus - (line_freq+alpha(i).*Bfield).*(1-
               Velocity./lightspeed))./sqrt(alpha_D*T);
         Rplus(i) = weights(i)*sum(exp(-(plus.^2))./Velocity)*delta_x/200.0;
          minus = (laser_minus - (line_freq-alpha(i).*Bfield).*(1-
               Velocity./lightspeed))./sqrt(alpha_D*T);
         Rminus(i) = weights(i)*sum(exp(-(minus.^2))./Velocity)*delta_x/200.0;

      %end integration, if computer fast enough, could use integration func. directly

      %Rplus_sum=Rplus_sum+weights(i)*Rplus;
      %Rminus_sum=Rminus_sum+weights(i)*Rminus;

         Rplus(i) = B01/(4*pi*sqrt(pi*alpha_D*T))*I*Rplus(i)/1.0E9;
         Rminus(i) = B01/(4*pi*sqrt(pi*alpha_D*T))*I*Rminus(i)/1.0E9;
    end
```

```
    %note: Rplus's unit is 1/GHZ

    Rplus_sum(m) =  sum(Rplus);
    Rminus_sum(m) =  sum(Rminus);
    %Pumping_Ratio(j)=Rminus_sum/Rplus_sum;

    %assume the observation point is at z=0 (Z=3.3cm)
    % Ions obey maxwell distribution and laser is single mode
    % Plamsa relaxation is slow and Plasma has arrived at new equilibrium
    y = xo;
    %Bfield1 = B*y + C;
    Bfield1 = C./(1+(y./r).^2).^1.5;
    Velocity1 = A*y + D;
    Aminus(m) = 0; Aplus(m) = 0; Splus(m)=0;Sminus(m)=0;
    for i=1:6
      freq_plus = (laser_freq(m)-(line_freq+alpha(i)*Bfield1)*(1-
              Velocity1/lightspeed))/sqrt(alpha_D*T);
      freq_minus= (laser_freq(m)-(line_freq-alpha(i)*Bfield1)*(1-
              Velocity1/lightspeed))/sqrt(alpha_D*T);
      Aplus(m) = Aplus(m) + (1-Rplus(i))*weights(i)*exp(-(freq_plus.^2));
      Aminus(m) = Aminus(m) + (1-Rminus(i))*weights(i)*exp(-(freq_minus.^2));
      Splus(m) = Splus(m) + weights(i)*exp(-(freq_plus.^2));
      Sminus(m) = Sminus(m) + weights(i)*exp(-(freq_minus.^2));
    end
  end
```

```
%curve fitting the simulation result to have T and A

laser_plus = (line_freq+alpha(1)*Bfield1)*(1.0-Velocity1/lightspeed);
laser_minus = (line_freq-alpha(1)*C)*(1.0-D/lightspeed);
center = laser_plus/2+laser_minus/2;
laser_freq = laser_freq - center;

fplus = inline ('coefplus(1)*exp(-((laser_freq-coefplus(2))/sqrt(10.8114*coefplus(3))).^2)+coefplus(4)','coefplus','laser_freq');
coef = [0.8,alpha(1)*Bfield1*(1.0-Velocity1/lightspeed),0.2,0.01];
coefplus = lsqcurvefit(fplus,coef,laser_freq,Aplus);

fminus = inline ('coefminus(1)*exp(-((laser_freq-coefminus(2))/sqrt(10.8114*coefminus(3))).^2)+coefminus(4)','coefminus','laser_freq');
coef = [0.8,-alpha(1)*Bfield1*(1.0-Velocity1/lightspeed),0.2,0.01];
coefminus = lsqcurvefit(fminus,coef,laser_freq,Aminus);

% end curve fitting

fittingplus = coefplus(1)*exp(-((laser_freq-coefplus(2))/sqrt(10.8114*coefplus(3))).^2)+coefplus(4);
fittingminus = coefminus(1)*exp(-((laser_freq-coefminus(2))/sqrt(10.8114*coefminus(3))).^2)+coefminus(4);

figure(j);
subplot(2,1,1);
plot(laser_freq, Rminus_sum,'r',laser_freq,Rplus_sum);
ylabel('pumping out rate,red is minus');
maxplus = max(Aplus);
```

```
maxminus = max(Aminus);
subplot(2,1,2);
plot(laser_freq, Aminus, 'r',laser_freq,
                    Aplus,'b',laser_freq,fittingplus,'b:',laser_freq,fittingminus,'r:');
hold;

Zeemanfreq = alpha.*Bfield1*(1.0-Velocity1/lightspeed);
plot(laser_freq, Sminus, 'c:',laser_freq, Splus,'c:',Zeemanfreq, weights, '*');

ylabel('Amplitude');

Nozzle_field(j) = C;
Signal_ratio(j) = coefplus(1)/coefminus(1);
Asplus(j) = coefplus(1); Asminus(j) = coefminus(1);
Signal_ratio(j) = Asplus(j)/Asminus(j);%maxplus/maxminus;
Adplus(j) = maxplus; Adminus(j) = maxminus;
T_ratio(j) = coefplus(3)/coefminus(3);
Tplus(j) = coefplus(3); Tminus(j) = coefminus(3);
end

figure(j+1);
plot (Nozzle_field, Signal_ratio,'k*-',Nozzle_field,T_ratio,'b*-');



OUT=fopen('kpoutput.txt','wt');
y = [Nozzle_field; Signal_ratio; T_ratio]
fprintf(OUT,'Nozzle_field  Amp_ratio T_ratio \n');
fprintf(OUT,'%f  %f  %f \n',y);
fclose(OUT);
```

```
OUT1=fopen('kpoutput1.txt','wt');
y = [Nozzle_field; Asplus; Asminus; Adplus; Adminus;Tplus; Tminus; ]
fprintf(OUT1,'Nozzle_field  As+ As- Ad+    Ad-  T+   T- \n');
fprintf(OUT1,'%f  %f  %f %f  %f  %f   %f\n',y);
fclose(OUT1);
```

VITAE

Xuan Sun

Education:

Doctor of Philosophy in Physics
2005 West Virginia University Morgantown, WV

Master of Science in Physics
2000 Univ. of Science & Technology of China Hefei, China

Bachelor of Engineering in Automation
1997 Southeast University Nanjing, China

Publications:

S. A. Cohen, **X. Sun**, N. M. Ferraro, E. E. Scime, M. Miah, S. Stange, N. Siefert, and R. Boivin, "On Collisionless Ion and Electron Populations in the Magnetic Nozzle Experiment (MNX)" accepted for publication in *IEEE Trans. Plasma Sci.* (2006)

C. Biloiu, **X. Sun,** E. Choueri, E. E. Scime, *et al.*, "Evolution of the Parallel and Perpendicular Ion Velocity Distribution Function in Pulsed Helicon Plasma Sources Obtained by Time Resolved Laser Induced Fluorescence" *Plasma Sources Sci. Technol.* **14**, 766 (2005).

X. Sun, E. Scime, and S. Cohen, "On-axis Parallel Ion Speeds near Mechanical and Magnetic Aperture in a Helicon plasma Device" **12**, 103509 (2005).

X. Sun, C. Biloiu, and E. Scime, "Observation of Resistive Drift Alfvén Waves in a Helicon Plasma" *Phys. Plasmas* **12**, 102105 (2005).

X. Sun, A. M. Keesee, C. Biloiu, E. E. Scime, A. Meige, C. Charles, and R. W. Boswell, "Observations of Ion-beam Formation in a Current-free Double-layer" *Phys. Rev. Lett.* **95**, 025004 (2005).

X. Sun, E. Scime, M. Miah, S. Cohen, and F. Skiff, "Measurement of Asymmetric Optical Pumping of Ions Accelerating in a Magnetic Field Gradient" *Phys. Rev. Lett.* **93**, 235002 (2004).

R. Hardin, **X. Sun**, and E. Scime, "3D Laser-induced Fluorescence Measurements in a Helicon Plasma" *Rev. Sci. Instrum.* **75**, 4103 (2004).

C. Biloiu, E. Scime, and **X. Sun**, “Scanning Internal Probe for Plasma Particle, Fluctuation, and LIF Tomographic Measurements” *Rev. Sci. Instrum.* **75**, 4296 (2004).

X. Sun, C. Biloiu, R. Hardin, and E. Scime “Parallel Velocity and Temperature of Argon Ions in an Expanding, Helicon Source Driven, Plasma” *Plasma Sources Sci. Technol.* **13**, 359 (2004).

J. L. Kline, M. Balkey, R. Boivin, A. M. Keesee, P. Keiter, E. Scime, and **X. Sun**, “Ion Dynamics in Helicon Plasmas” *Phys. Plasmas* **10**, 2127 (2003).

J. L. Kline, E. Scime, R. Boivin, A. M. Keesee, and **X. Sun** “Slow Wave Ion Heating in the HELIX Helicon Source” *Plasma Sources Sci. Technol.* **11**, 413 (2002).

J. Kline, E. Scime, R. Boivin, A. M. Keesee, **X. Sun**, and V. Mikhailenko, “RF Absorption and Ion Heating in Helicon Sources” *Phys. Rev. Lett.* **88**, 195002 (2002).

X. Sun, Z.J. Wang, R. H. Lu, and Y. Z. Wen, *et. al.*, “Excitation and Propagation of Modified Fluctuation in a Toroidal Plasma in KT-5C Device*”* *Plasma Sci. Technol.* **4**, 1361 (2002